

The Vera C. Rubin Observatory Data Preview 1

VERA C. RUBIN OBSERVATORY¹

¹*Placeholder used for collective author that will not be shown*

(Dated: July 3, 2025)

ABSTRACT

We present [Data Preview 1 \(DP1\)](#), the first data from the [National Science Foundation \(\)-Department of Energy \(\)](#) Vera C. Rubin Observatory, comprising raw and calibrated single-epoch images, coadds, difference images, detection catalogs, and derived data products. [DP1](#) is based on 1792 science-grade optical/near-infrared exposures acquired over 48 distinct nights by the [Rubin Commissioning Camera](#), LSSTComCam, on the [Simonyi Survey Telescope](#) at the [Summit Facility](#) on Cerro Pachón, Chile during the first on-sky commissioning campaign in late 2024. [DP1](#) covers ~ 15 sq. deg. over seven roughly equally-sized non-contiguous fields, each independently observed in six broad photometric bands, *ugrizy*, spanning a range of stellar densities and latitudes and overlapping with external reference datasets. The median image quality across all bands, measured by the [Full Width at Half-Maximum \(FWHM\)](#) of the point-spread function, is approximately 1.13 arcseconds, with the sharpest images reaching about 0.65 arcseconds. [DP1](#) contains approximately 2.3 million distinct astrophysical objects, of which 1.6 million are extended in at least one band, and 431 solar system objects, of which 93 are new discoveries. [DP1](#) is approximately 3.5 TB in size and available to Rubin data rights holders via the [Rubin Science Platform](#), a cloud-based environment for the analysis of petascale astronomical data. While small compared to future [Legacy Survey of Space and Time \(formerly Large Synoptic Survey Telescope\) \(LSST\)](#) releases, its high quality and diversity of data support a broad range of early science investigations across all four [LSST](#) themes ahead of full operations in late 2025.

Keywords: Rubin Observatory – LSST

1. INTRODUCTION

The [NSF–DOE](#) Vera C. Rubin Observatory is a ground-based, wide-field optical/near-infrared facility located on Cerro Pachón in northern Chile. Named in honor of Vera C. Rubin, a pioneering astronomer whose groundbreaking work in the 20th century provided the first convincing evidence for the existence of dark matter ([V. C. Rubin & W. K. Ford 1970](#); [V. C. Rubin et al. 1980](#)), the observatory’s prime mission is to carry out the [LSST](#) ([Ž. Ivezić et al. 2019a](#)). This 10-year survey is designed to obtain rapid-cadence, multi-band imaging of the entire visible southern sky approximately every 3–4 nights, mapping it to a depth of ~ 27.5 magnitude in the r-band with ~ 0.7 arcsecond seeing, with a total of ~ 800 visits per pointing.

The Rubin Observatory system consists of four main components: the [Simonyi Survey Telescope](#), featuring an 8.4 m diameter (6.5 m effective aperture) primary mirror that delivers a wide field of view; a 3.2-gigapixel

Camera, capable of imaging 9.6 square degrees per exposure with seeing-limited quality in six broadband filters, *ugrizy* (320–1050 nm); an automated [Data Management System](#) that processes and archives tens of terabytes of data per night, generating science-ready data products within minutes for a global community of scientists; and an [Education and Public Outreach \(\)](#) program that provides real-time data access, interactive tools, and educational content to engage the public. The integrated system’s étendue² of $319 \text{ m}^2 \text{ deg}^2$, is over an order of magnitude larger than that of any existing facility, enabling a fast, large-scale survey with exceptional depth in a fraction of the time compared to other observatories.

The observatory’s design is driven by four key science themes: probing dark energy and dark matter; taking

² The product of the primary mirror area and the angular area of its field of view for a given set of observing conditions.

an inventory of the solar system; exploring the [transient](#) optical sky; and mapping the Milky Way ([Ž. Ivezić et al. 2019a](#)). These themes inform the optimization of a range of system parameters, including image quality, photometric and astrometric accuracy, the depth of a single visit and the co-added survey depth, the filter complement, the total number of visits per pointing as well as the distribution of visits on the sky, and total sky coverage. Additionally, they inform the design of the data processing and access systems. By optimizing the system parameters to support a wide range of scientific goals, we maximize the observatory’s scientific output across all areas, transforming Rubin into a powerful discovery machine capable of addressing a broad range of astrophysical questions.

Over the lifetime of the [LSST](#), Rubin Observatory will issue several Data Releases, each representing a full reprocessing of all [LSST](#) data collected to date. Prior to the start of the [LSST](#) survey, commissioning activities will generate a significant volume of science-grade data. To make this early data available to the community, the Rubin Early Science Program, ([L. P. Guy et al. 2025](#)), was established. One key component of this program is a series of Data Previews; early versions of the [LSST](#) Data Releases. These previews include preliminary data products derived from both simulated and commissioning data, which, together with early versions of the data access services, are intended to support high-impact early science, facilitate community readiness, and inform the development of Rubin’s operational capabilities ahead of the start of full survey operations. All data and services provided through the Rubin Early Science Program are offered on a shared-risk basis³.

This paper describes Rubin’s second of three planned Data Previews: [DP1](#) ([NSF-DOE Vera C. Rubin Observatory 2025](#)). The first, [Data Preview 0 \(DP0\)](#)⁴, contained data products produced from the processing of simulated [LSST](#)-like data sets, together with a very early version of the Rubin [Science Platform](#) ([M. Jurić et al. 2019](#)). [DP1](#) contains data products derived from the reprocessing of science-grade exposures acquired by the [Rubin Commissioning Camera](#) (), in late 2024. The third and final Data Preview, [Data Preview 2 \(DP2\)](#), is planned to be based on a reprocessing of all science-grade data taken with the Rubin’s [LSST Science Camera](#)

(), during commissioning, and is expected to be released around mid-2026.

All Rubin Data Releases and Previews are subject to a two-year proprietary period, with immediate access granted exclusively to data rights holders ([R. Blum & the Rubin Operations Team 2020](#)). Data rights holders are individuals or institutions with formal authorization to access proprietary data collected by the Vera C. Rubin Observatory. This includes all scientists in the United States, Chile, and designated individuals or groups from other countries⁵. After the two-year proprietary period, [DP1](#) will be made public.

In this paper, we present the contents and validation of, and the data access and community support services for, Rubin [DP1](#), the first Data Preview to deliver data derived from observations conducted by the Vera C. Rubin Observatory. [DP1](#) is based on the reprocessing of a subset of 1792 science-grade exposures acquired over 48 nights during the first on-sky commissioning campaign using the Rubin Commissioning [Camera](#), [LSSTComCam](#), between 2024-11-09 and 2024-12-11. It covers a total area of approximately ~ 15 sq. deg. distributed across seven distinct non-contiguous fields. The data products include raw and calibrated single-epoch images, coadded images, difference images, detection catalogs, and other derived data products. [DP1](#) is about 3.5 TB in size and contains around 2.3 million distinct astronomical objects, detected in 2644 coadded images. Full [DP1](#) release documentation is available at <https://dp1.lsst.io>. Despite Rubin Observatory still being in commissioning and not yet complete, Rubin [DP1](#) provides an important first look at the data, showcasing its characteristics and capabilities.

The structure of this paper is as follows. In [§2](#) we describe the observatory system and overall construction completion status at the time of data acquisition, the seven fields included in [DP1](#) and the observing strategy used. [§3](#) summarizes the contents of [DP1](#) and the different types of data products contained in the release. The data processing pipelines are described in [§4](#), followed by a description of the data validation and performance assessment in [§5](#). [§6](#) describes the Rubin [Science Platform](#) (RSP), a cloud-based data science infrastructure that provides tools and services to Rubin data rights holders to access, visualize and analyze petascale data generated by the [LSST](#). [§7](#) presents Rubin’s model for community support, which emphasizes self-help via documentation and tutorials, and employs an open platform for asynchronous issue reporting that en-

³ Shared risk means early access with caveats: the community benefits from getting a head start on science, preparing analyses, and providing feedback, while also accepting that the experience may not be as polished or reliable as it will be during full operations.

⁴ See <https://dp0.lsst.io>

⁵ See <https://www.lsst.org/scientists/international-drh-list>

ables crowd-sourced solutions. Finally, a summary of the DP1 release and information on expected future releases of data is given in §8. The appendix contains a useful glossary of terms and the bibliography.

All magnitudes quoted are in the AB system (J. B. Oke & J. E. Gunn 1983), unless otherwise specified.

2. ON-SKY COMMISSIONING CAMPAIGN

The first Rubin on-sky commissioning campaign was conducted using the LSSTComCam between 2024-10-24 and 2024-12-11, spanning a total of 48 nights. The primary objective was to optically align the Simonyi Survey Telescope and verify its ability to deliver acceptable image quality using LSSTComCam. In addition, the campaign provided valuable operations experience to facilitate commissioning the full LSSTCam, (A. Roodman et al. 2024; T. Lange et al. 2024). It is important to note that commissioning LSSTComCam was not an objective of the campaign. Instead, LSSTComCam was used as a tool to support broader observatory commissioning, including early testing of the Active Optics System (AOS) and the LSST Science Pipelines. As a result, many artifacts present in the data are specific to LSSTComCam and will only be addressed if they persist with LSSTCam. Accordingly, the image quality achieved during this campaign, and in the DP1 data, may not reflect the performance ultimately expected from LSSTCam.

Approximately 16,000 exposures⁶ were collected during this campaign, the majority in support of AOS commissioning, system-level verification, and end-to-end testing of the telescope’s hardware and software. This included over 10000 exposures for AOS commissioning, more than 2000 bias and dark calibration frames, and over 2000 exposures dedicated to commissioning the LSST Science Pipelines. For DP1, we have selected a subset of 1792 science-grade exposures from this campaign that are most useful for the community to begin preparing for early science.

At the time of the campaign, the observatory was still under construction, with several key components, such as dome thermal control, full mirror control, and the final AOS configuration either incomplete or still undergoing commissioning. As a result, image quality varied widely throughout the campaign and exhibited a broader distribution than is expected with LSSTCam. Despite these limitations, the campaign success-

fully demonstrated system integration and established a functional observatory.

2.1. Simonyi Survey Telescope

The Simonyi Survey Telescope (B. Stalder et al. 2024) features a unique three-mirror design, including an 8.4-meter Primary Mirror Tertiary Mirror (M1M3) fabricated from a single substrate and a 3.5-meter Secondary Mirror (M2). This compact configuration supports a wide 3.5-degree field of view while enabling exceptional stability, allowing the telescope to slew and settle in under five seconds. To achieve the scientific goals of the 10-year LSST, the Observatory must maintain high image quality across its wide field of view (Ž. Ivezić et al. 2019b). This is accomplished through the AOS (B. Xin et al. 2015; G. Megias Homar et al. 2024), which corrects, between successive exposures, wavefront distortions caused by optical misalignments and surface deformation primarily under the effect of gravitational and thermal loads.

The AOS, which comprises open- and closed-loop components, optimizes image quality by aligning the camera and M2 relative to M1M3, as well as adjusting the shapes of all three mirrors. The AOS open-loop component corrects for distortions and misalignments resulting from gravitational and thermal effects, while the closed-loop component addresses unpredictable or slowly varying aberrations using feedback from the corner wavefront sensors. The closed-loop wavefront sensing technique is curvature sensing, analyzing extra-focal and intra-focal images to infer the wavefront errors in the system (S. Thomas et al. 2023). Since LSSTComCam lacks wavefront sensors, wavefront errors were estimated by defocusing the telescope ± 1.5 mm on either side of focus and applying the curvature wavefront pipeline to measure and correct for wavefront errors.

Each night began with an initial alignment correction using a laser tracker to position the system within the capture range of the closed-loop algorithm (G. M. Homar et al. 2024). Alignment was achieved using the AOS system. Once the optics were aligned, the image quality was optimized across the LSSTComCam field of view by applying additional corrections to the shape of the mirrors. During Science Pipelines commissioning (§2.4), observations were undertaken using the open-loop component with no correction for thermal effects. The image quality for these data was monitored by measuring the Point Spread Function (PSF) FWHM and periodically rerunning the closed-loop component when the image quality degraded. Under favorable seeing conditions, the delivered image quality was typically around $0.7''$, with a best recorded value of $0.58''$.

⁶ We define an “exposure” as the process of exposing all LSSTComCam detectors. It is synonymous with “visit” in DP1. By contrast, an “image” is the output of a single LSSTComCam detector following an exposure.

2.2. The Rubin Camera

248

249 The LSSTComCam (SLAC National Accelerator
 250 Laboratory & NSF-DOE Vera C. Rubin Observatory
 251 2024; B. Stalder et al. 2022, 2020; J. Howard et al.
 252 2018), is a 144-megapixel, scaled-down version of the
 253 3.2-gigapixel LSSTCam. It covers approximately 5% of
 254 the LSSTCam focal plane area and is designed to val-
 255 idate camera interfaces with other observatory compo-
 256 nents and evaluate overall system performance prior to
 257 the start of LSSTCam commissioning.

258 The LSSTCam focal plane consists of 21 modular sci-
 259 ence rafts for imaging, arranged in a 5×5 grid, along
 260 with 4 additional corner rafts dedicated to guiding and
 261 wavefront sensing. Each raft is a self-contained unit
 262 comprising nine $4K \times 4K$ Charge-Coupled Device () sen-
 263 sors arranged in a 3×3 mosaic, along with integrated
 264 readout electronics and cooling systems. Each sensor is
 265 subdivided into 16 segments arranged in a 2×8 layout,
 266 with each segment containing $512 \times 2k$ pixels. All 16 seg-
 267 ments are read out in parallel using dedicated amplifiers,
 268 one per segment. LSSTCam uses CCD sensors from
 269 two vendors: Imaging Technology Laboratory (Univer-
 270 sity of Arizona (UA)) (UA) and Teledyne (E2V). To
 271 ensure uniform performance and calibration within each
 272 module, individual rafts are populated with sensors from
 273 only one vendor.

274 LSSTComCam consists of a single raft equipped ex-
 275 clusively with ITL sensors. The sensors selected for
 276 LSSTComCam represent the lowest-performing units
 277 from the LSSTCam production batch and exhibit known
 278 issues, including high readout noise (e.g., Detector 8)
 279 and elevated Charge Transfer Inefficiency (CTI) (e.g.,
 280 Detector 5). As a result, some image artifacts observed
 281 in the DP1 dataset may be specific to ITL sensors.

282 Figure 1 shows the single-raft LSSTComCam posi-
 283 tioned at the center of the full LSSTCam focal plane.
 284 LSSTComCam is designated as Raft 22 (R22) and is
 285 installed at the center of the LSSTCam focal plane, cor-
 286 responding to the central science raft position.

288 Figure 2 shows the LSSTComCam focal plane layout,
 289 illustrating the enumeration of sensors and amplifiers,
 290 along with their physical arrangement within the raft.
 291 The LSSTCam and LSSTComCam focal planes are de-
 292 scribed in detail in Plazas Malagón, A. et al. (2025).

294 LSSTComCam is housed in a support structure that
 295 precisely replicates the total mass, center of gravity,
 296 and physical dimensions of LSSTCam, with all mechani-
 297 cal and utility interfaces to the telescope implemented
 298 identically. This configuration supports full end-to-end
 299 testing of the observatory systems, including readout
 300 electronics, image acquisition, and data pipelines. The
 301 LSSTComCam plate scale is 0.2 arcsec. per pixel.

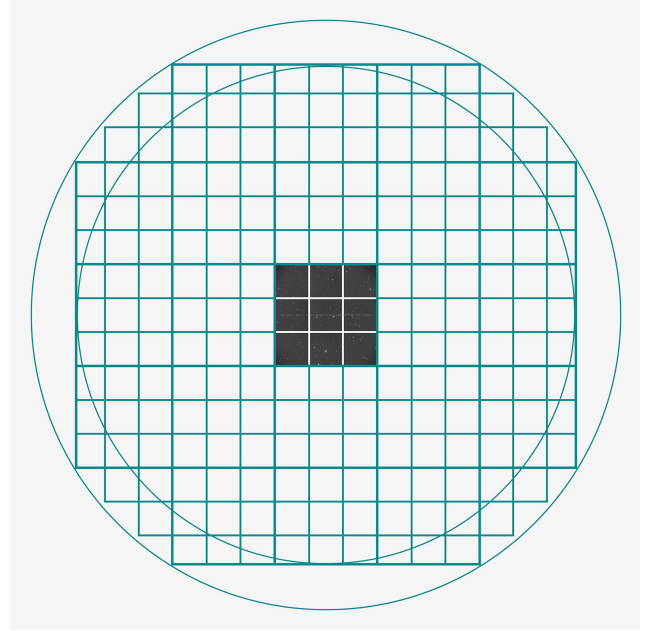
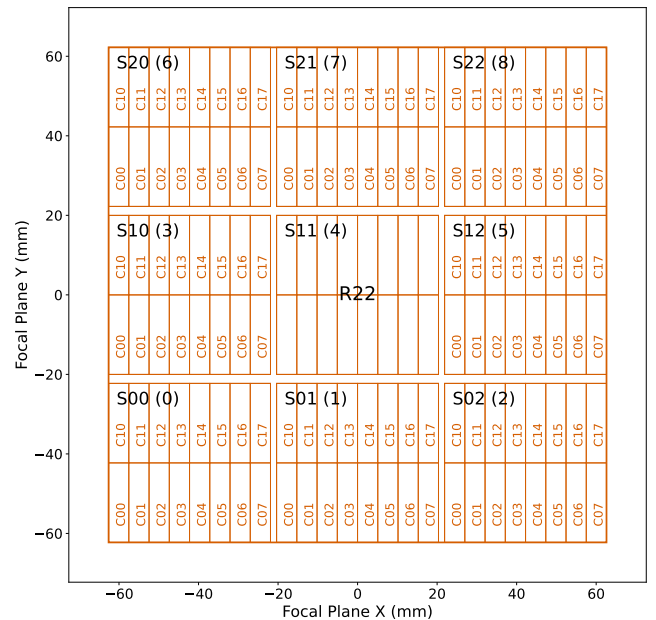


Figure 1. Schematic showing the single-raft LSSTComCam positioned at the center of the full LSSTCam focal plane. The perspective is from above, looking down through the LSSTComCam lenses onto the focal plane. Credit: RubinObs/NOIRLab/SLAC/NSF/DOE/AURA.



2.2.1. Filter Complement

LSSTComCam supports imaging with six broadband filters *ugrizy* spanning 320–1050 nm, identical in design to LSSTCam. However, its filter exchanger can hold only three filters at a time, compared to five in LSSTCam. The full-system throughput of the six LSSTComCam filters, which encompasses contributions from a standard atmosphere at airmass 1.2, telescope optics, camera surfaces, and the mean ITL detector quantum efficiency is shown in Figure 3.

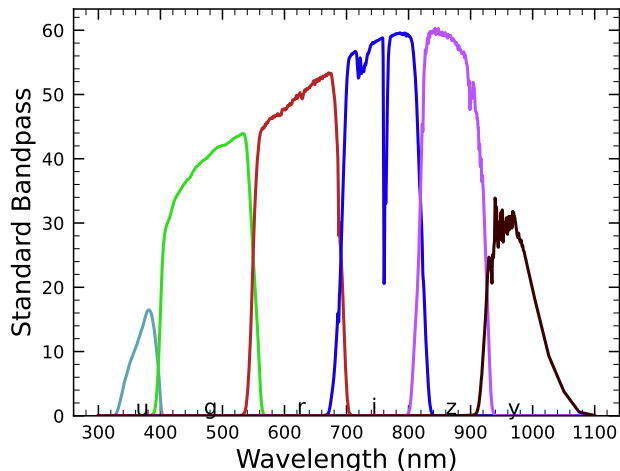


Figure 3. LSSTComCam standard bandpasses, illustrating full system throughput. The bandpasses include a standard atmosphere at airmass 1.2, telescope optics, camera surfaces, and mean ITL detector quantum efficiency.

2.3. Flat Field System

During the on-sky campaign, key components of the Rubin calibration system (P. Ingraham et al. 2022), including the flat field screen, Collimated Beam Projector (), and the Ekspla tunable laser had not yet been installed. As a result, flat fielding for DP1 relied entirely on twilight flats. While twilight flats pose challenges such as non-uniform illumination and star print-through, they were the only available option during LSSTComCam commissioning and for DP1 processing. To mitigate these limitations, dithered, tracked exposures were taken over a broad range of azimuth and rotator angles to construct combined flat calibration frames. Exposure times were dynamically adjusted to reach target signal levels of between 10,000 and 20,000 electrons. Future campaigns will benefit from more stable and uniform flat fielding using the Rubin flat field system, described in P. Fagrelius & E. Rykoff (2025).

2.4. LSST Science Pipelines Commissioning

Commissioning of the LSST Science Pipelines (Rubin Observatory Science Pipelines Developers 2025) began once the telescope was able to routinely deliver sub-arcsecond image quality. The goals included testing the internal astrometric and photometric calibration across a range of observing conditions, validating the difference image analysis and Prompt Processing (K.-T. Lim 2022) framework, and accumulating over 200 visits per band to evaluate deep coadded images with integrated exposure times roughly equivalent to those of the planned LSST Wide Fast Deep (WFD) 10-year depth. To support these goals, seven target fields were selected that span a range of stellar densities, overlap with external reference datasets, and collectively span the full breadth of the four primary LSST science themes. These seven fields form the basis of the DP1 dataset. Figure 4 shows the locations of these seven fields on the sky, overlaid on the LSST baseline survey footprint (R. L. Jones 2021; P. Yoachim 2022; Z. Ivezić 2022; The Rubin Observatory Survey Cadence Optimization Committee 2023, 2025), along with sky coverage of both the LSSTCam and LSSTComCam focal planes. Each of the seven target fields was observed repeatedly in multiple bands over many nights. A typical observing epoch on a given target field consisted of 5–20 visits in each of the three loaded filters. Only images taken as 1x30 second exposures have been included in DP1. All images were acquired using the Rubin Feature-Based Scheduler (FBS), version 3.0 (E. Naghib et al. 2019; P. Yoachim et al. 2024). Table 1 lists the seven DP1 fields and their pointing centers, and provides a summary of the band coverage in each.

The temporal sampling distribution of observations per band and per night is shown in Figure 5. Gaps in coverage across some bands arise from the fact that LSSTComCam can only accommodate three filters at a time §2.2. As the campaign progressed, the temporal sampling became denser across all fields, reflecting improved efficiency and increased time allocated for science observations. The Extended Chandra Deep Field-South Survey (ECDFS) field received the most consistent and densest temporal sampling. It is important to note that the time sampling in the DP1 dataset differs significantly from what will be seen in the final LSST data.

All fields except for the low ecliptic latitude field, Rubin_SV_38_7, used random translational and rotational dithers within a 0.2 degree radius around the pointing center (Table 1). The rotational dithers were typically applied at the time of filter changes for operational efficiency, with translational dithers of approximately 1 degree applied between individual visits. The Rubin_SV_38_7 field used a different dither pattern to optimize coverage of Solar System Objects and test Solar System Object linking across multiple nights. These observations used a 2 x 2 grid of LSSTComCam pointings to cover an area of about 1.3 degree x 1.3 degrees. The visits cycled between the grid’s four pointing centers, using small random dithers to fill chip gaps with the goal of acquir-

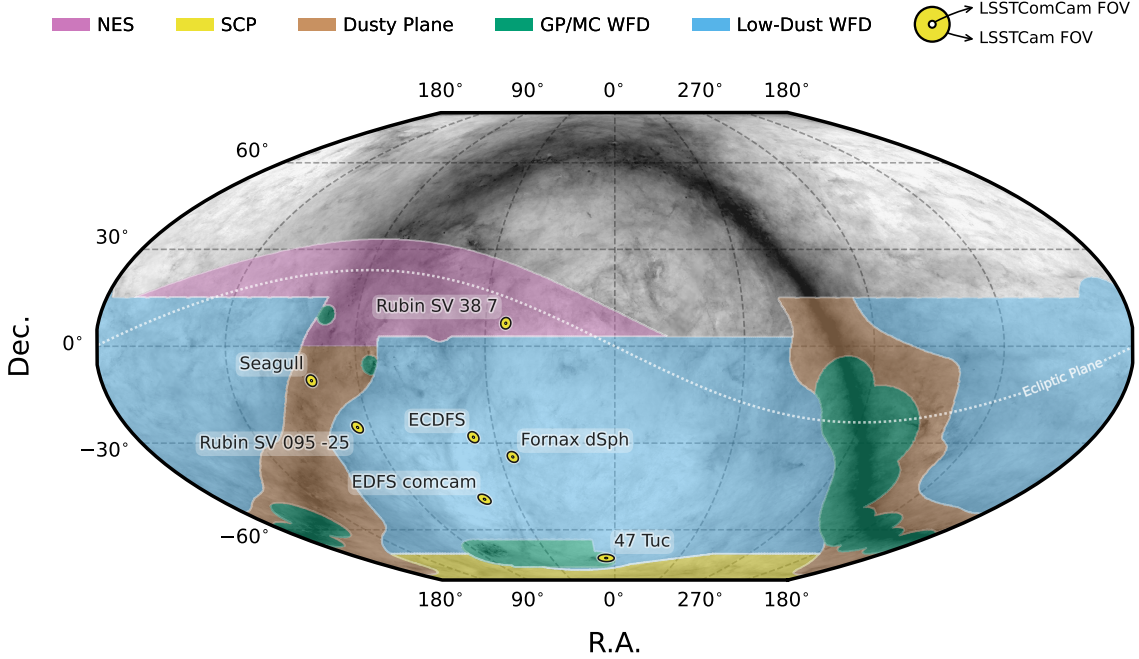


Figure 4. Location of the seven DP1 fields overlaid on the LSST baseline survey footprint. NES: North Ecliptic Spur, SCP: South Celestial Pole, Low-Dust WFD: regions away from the GP observed with a WFD cadence, GP/MC WFD: Galactic Plane and Magellanic Clouds regions observed with a WFD cadence. The field of view (FOV) covered by the LSSTCam and LSSTComCam focal planes is shown as concentric yellow circles about the pointing center of each field.

Table 1. DP1 fields and pointing centers with the number of exposures in each band per field. ICRS coordinates are in units of decimal degrees.

Field Code	Field Name	RA	DEC	Band						Total
				u	g	r	i	z	y	
47_Tuc	47 Tucanae Globular Cluster	6.128	-72.090	6	10	32	19	0	5	72
ECDFS	Extended Chandra Deep Field South	53.160	-28.100	43	230	237	162	153	30	855
EDFS_comcam	Rubin SV Euclid Deep Field South	59.150	-48.730	20	61	87	42	42	20	272
Fornax_dSph	Fornax Dwarf Spheroidal Galaxy	40.080	-34.450	0	5	25	12	0	0	42
Rubin_SV_095_-25	Rubin SV Low Galactic Latitude Field	95.040	-25.000	33	82	84	23	60	10	292
Rubin_SV_38_7	Rubin SV Low Ecliptic Latitude Field	37.980	7.015	0	44	40	55	20	0	159
Seagull	Seagull Nebula	106.300	-10.510	10	37	43	0	10	0	100

ing 3-4 visits per pointing center per band in each observing epoch.

2.5. Delivered Image Quality

The delivered image quality is influenced by contributions from both the observing system (i.e., dome, telescope and camera) and the atmosphere. During the campaign, the Rubin Differential Image Motion Monitor (DIMM) was not operational, so atmospheric seeing was estimated using live data from the Southern Astrophysical Research Telescope (SOAR) Ring-Image Next Generation Scintillation Sensor (RINGS) seeing monitor. Although accelerometers mounted on the

mirror cell and top-end assembly were available to track dynamic optics effects, such as mirror oscillations that can degrade optical alignment, this data was not used during the campaign. Mount encoder data was used to measure the mount jitter in every image, with a median contribution of 0.004 arcseconds to image degradation measured. As the pointing model was not fine tuned, tracking errors could range from 0.2 to 0.4 arcseconds per image, depending on RA and Dec. Dome and mirror-induced seeing were not measured during the campaign. The median delivered image quality for commanded in-focus images (all bands) was 1.14", as measured by the PSF FWHM. The best images achieved a

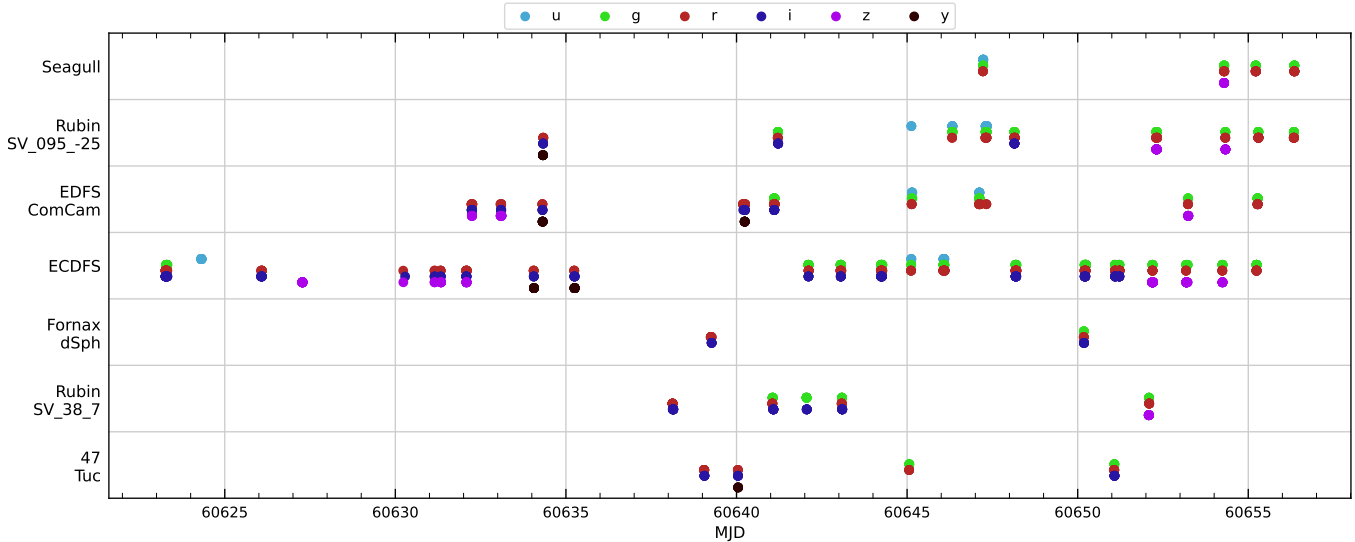


Figure 5. Distribution of DP1 observations by date grouped by field and color coded by band.

418 PSF FWHM of approximately $0.58''$. Ongoing efforts aim to
 419 quantify all sources of image degradation, including contribu-
 420 tions from the camera system, static and dynamic optical
 421 components, telescope mount motion, observatory-induced
 422 seeing from the dome and mirror, and atmospheric condi-
 423 tions.

3. OVERVIEW OF THE CONTENTS OF RUBIN DP1

424 Here we describe Rubin DP1 data products and provide
 425 summary statistics for each. The DP1 science data products
 426 are derived from the 15972 individual CCD images taken
 427 across 1792 exposures in the seven LSSTComCam commis-
 428 sioning fields (§2.4).

429 The data products that comprise DP1 provide an early
 430 preview of future LSST data releases and are strongly de-
 431 pendent on the type and quality of the data that was col-
 432 lected during LSSTComCam on-sky campaign (§2.4). Con-
 433 sequently not all anticipated LSST data products, as de-
 434 scribed in the Data Product Definition Document () (M.
 435 Jurić et al. 2023) were produced for the DP1 dataset.

436 At the highest level, the DP1 data products fall into one
 437 of five types:

- 440 • **Images**, including single-epoch images, deep and tem-
 441 plate coadded images, and difference images;
- 442 • **Catalogs** of astrophysical sources and objects de-
 443 tected and measured in the aforementioned images. We
 444 also provide the astrometric and photometric refer-
 445 ence catalog generated from external sources that was
 446 used during processing to generate the DP1 data
 447 products;
- 448 • **Maps**, which provide non-science-level visualizations
 449 of the data within the release. They include, for exam-
 450 ple, zoomable multi-band images and coverage maps;
- 451 • **Ancillary data products**, including, for example,
 452 the parameters used to configure the data process-
 453 ing pipelines, log and processing performance files,

plots and metrics produced during the data processing
 steps, and calibration data products (e.g. CTI models,
 brighter-fatter kernels, etc.);

- 457 • **Metadata** in the form of tables containing informa-
 458 tion about each visit and processed image, such as
 459 pointing, exposure time, and a range of image qual-
 460 ity summary statistics.

461 While images and catalogs are expected to be the primary
 462 data products for scientific research, we also recognize the
 463 value of providing access to other data types to support in-
 464 vestigations and ensure transparency.

465 To facilitate processing, Rubin DP1 uses a single skymap⁷
 466 that covers the entire sky area encompassing the seven DP1
 467 fields. The DP1 skymap divides the entire celestial sphere
 468 into 18938 tracts, each covering approximately 2.8 sq. deg..
 469 Each tract is further subdivided into 10×10 equally-sized
 470 patches, with each patch covering roughly 0.028 sq. deg..
 471 Both tracts and patches overlap with their neighboring re-
 472 gions. Since the LSSTComCam only observed ~ 15 sq. deg.
 473 of the sky during its campaign, only 29 out of the 18938
 474 tracts have coverage in DP1. The tract identification num-
 475 bers and corresponding target names for these tracts are listed in
 476 Table 2.

477 The skymap is integral to the production of co-added im-
 478 ages. To create a coadded image, the processing pipeline
 479 selects all calibrated science images that meet specific qual-
 480 ity thresholds (§3.1 and §4.5.1) for a given patch, warps them
 481 onto a single consistent pixel grid for that patch, as defined
 482 by the skymap, then coadds them. Each individual coadd im-
 483 age therefore covers a single patch. Coadded images and the
 484 catalogs of detections from them are termed tract-level data
 485 products. By contrast, visit-level data products are those

⁷ A skymap is a tiling of the celestial sphere, organizing large-
 scale sky coverage into manageable sections for processing and
 analysis.

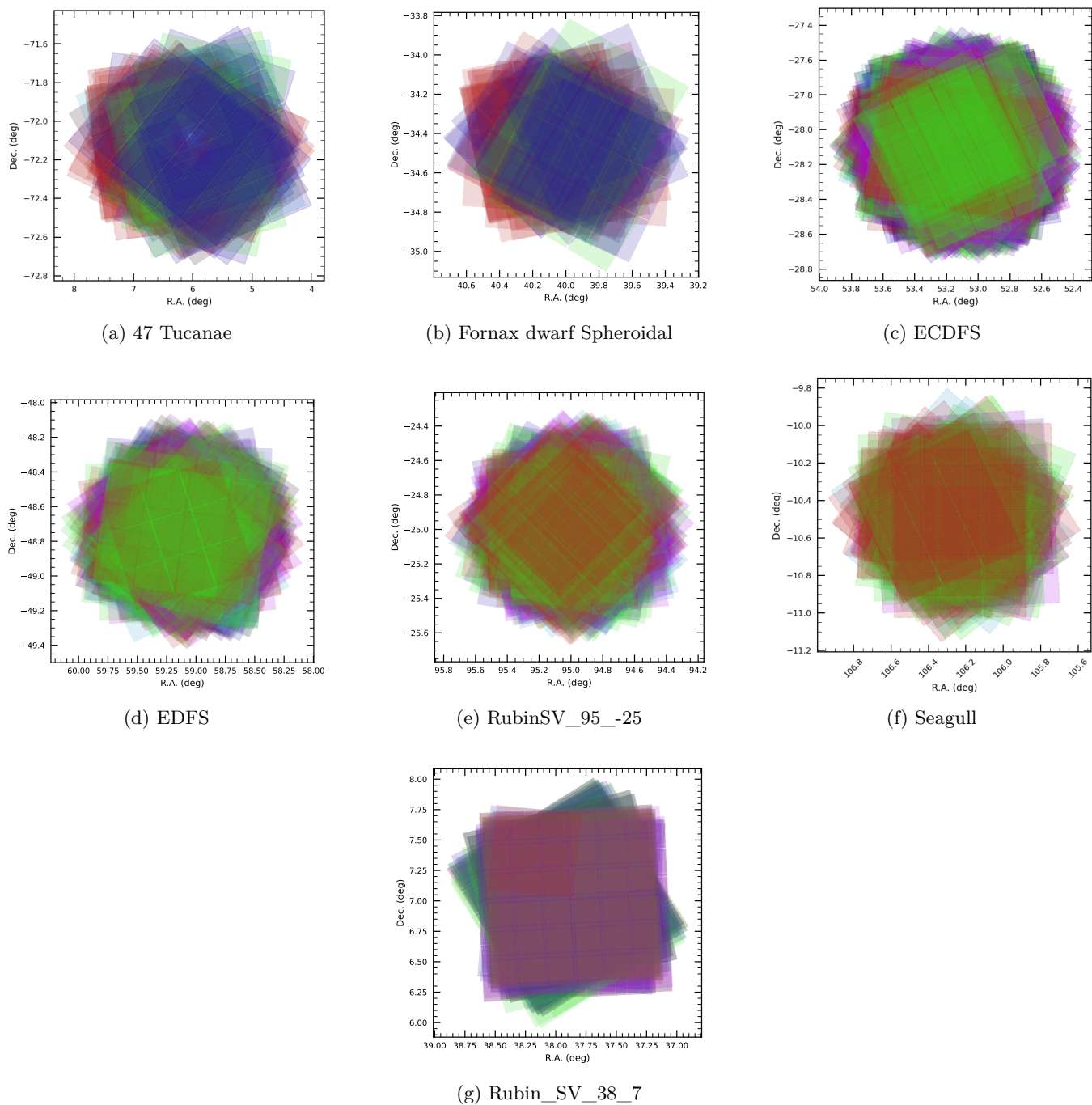


Figure 6. Sky coverage for seven DP1 fields.

487 derived from individual LSSTComCam exposures, such as 497
 488 a raw image or a catalog of detections from a single cali- 498
 489 brated image. Most science data products (i.e., images and 499
 490 catalogs) in DP1 are either `tract` or `visit`-level, the main 500
 491 exception being the `Calibration` reference catalog. 501

492 Throughout this section, the data product names are in- 502
 493 dicated using `monospace` font. Data products are accessed 503
 494 via either the International Virtual-Observatory Alliance 504
 495 (IVOA) Services (§6.2.1) or the Data Butler (§6.2.2), or 505
 496 both. 506

3.1. Science Images

Science images are exposures of the night sky, as distinct 507
 from `calibration` images (§3.5.3). Although the release in- 508
 cludes `calibration` images, allowing users to reprocess the raw 509
 images if needed, this is expected to be necessary only in rare 510
 cases. Users are strongly encouraged to start from the `visit`- 511
 level images provided. The data product names shown here 512
 are those used by the Data Butler, but the names used in the 513

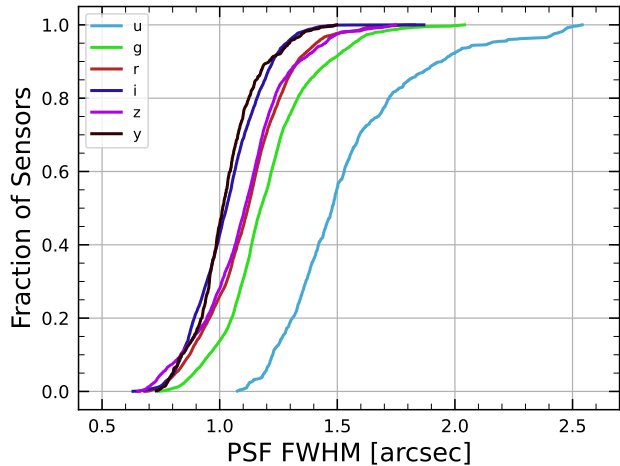


Figure 7. Cumulative distribution of PSF FWHM of the DP1 dataset.

Table 2. Tract coverage of each DP1 field.

Field Code	Tract ID
ECDFS	5062, 5063, 5064, 4848, 4849
Seagull	7850, 7849, 7610, 7611
Rubin_SV_38_7	10464, 10221, 10222, 10704, 10705, 10463
EDFS_comcam	2393, 2234, 2235, 2394
Rubin_SV_095_-25	5305, 5306, 5525, 5526
47_Tuc	531, 532, 453, 454
Fornax_dSph	4016, 4217, 4218, 4017

505 IVOA Services differ only slightly in that they are prepended
506 by “lsst.”.

507 • **raw** images (NSF-DOE Vera C. Rubin Observatory
508 2025a) are unprocessed data received directly from the
509 camera. Each **raw** corresponds to a single CCD from a
510 single LSSTComCam exposure of 30 s duration. Each
511 LSSTComCam exposure typically produces up to nine
512 **raws**, one per sensor in the focal plane. However, a
513 small number of exposures resulted in fewer than nine
514 **raw** images due to temporary hardware issues or read-
515 out faults.

516 In total, DP1 includes 16125 **raw** images. Table 3 pro-
517 vides a summary by target and band. A **raw** contains
518 4608×4096 pixels, including prescan and overscan,
519 and occupies around 18 MB of disk space.⁸ The field
520 of view of a single **raw**, excluding prescan and over-

⁸ Each amplifier image contains 3 and 64 columns of serial pre-
scan and overscan pixels, respectively, and 48 rows of parallel
overscan pixels, meaning a **raw** contains 4072×4000 exposed
pixels.

521 scan regions, is roughly $0.23^\circ \times 0.22^\circ \approx 0.051$ sq. deg.,
522 corresponding to a plate scale of 0.2 arcsec. per pixel.

523 • **visit_images** (NSF-DOE Vera C. Rubin Observatory
524 2025b) are fully-calibrated processed images. They
525 have undergone instrument signature removal (§4.2.1)
526 and all the single frame processing steps described in
527 §4.2 which are, in summary: PSF modeling, back-
528 ground subtraction, and astrometric and photomet-
529 ric calibration. As with **raws**, a **visit_image** contains
530 processed data from a single CCD resulting from a single
531 30 s LSSTComCam exposure. As a consequence,
532 a single LSSTComCam exposure typically results in
533 nine **visit_images**. The handful of exposures with
534 fewer than nine **raw** images also have fewer than nine
535 **visit_images**, but there are an additional 153 **raw**
536 that failed processing and for which there is thus no
537 corresponding **visit_image**. Almost all failures were
538 due to challenges with astrometric fits or PSF models.
539 In total, there are 15972 **visit_images** in DP1. Each
540 **visit_image** comprises three images: the calibrated
541 science image, a variance image, and a pixel mask,
542 indicating, for example, bad or saturated pixels, pix-
543 els affected by cosmic rays, pixels associated with de-
544 tected sources, etc.). Each **visit_image** also contains
545 a position-dependent PSF model, World Coordinate
546 System () information, and various metadata provid-
547 ing information about the observation and processing.
548 The science and variance images and the pixel mask
549 each contain 4072×4000 pixels. In total, a single
550 **visit_image**, including all extensions and metadata,
551 occupies around 110 MB of disk space.

552 • **deep_coadds** (NSF-DOE Vera C. Rubin Observatory
553 2025c) are the product of warping and co-adding mul-
554 tiple **visit_images** covering a given patch, as defined
555 by the skymap. **deep_coadds** are created on a per-
556 band basis, meaning only data from exposures taken
557 with a common filter are coadded. As such, there
558 are up to six **deep_coadds** covering each patch – one
559 for each of the six LSSTComCam bands. The pro-
560 cess of producing **deep_coadds** is described in detail
561 in §4.5 but, to summarize, it involves the selection of
562 suitable **visit_images** (both in terms of patch cov-
563 erage, band, and image quality), the warping of those
564 **visit_images** onto a common pixel grid, and the co-
565 adding of the warped **visit_images**. To be included
566 in a DP1 **deep_coadd**, a **visit_image** needed to have a
567 PSF FWHM smaller than $1.7''$. Of the 15972 **visit_-**
568 **images**, N satisfied this criterion and were therefore
569 used to create **deep_coadds**.

570 There are a total of 2644 **deep_coadds** in DP1. As
571 mentioned above, a single **deep_coadd** covers one
572 patch, and includes a small amount of overlap with
573 its neighboring patch. The skymap used for DP1 de-
574 fines a patch as having an on-sky area of 0.028 sq. deg.
575 excluding overlap, and 0.036 sq. deg. including over-
576 lap. A single **deep_coadd** – including overlap – con-
577 tains 3400×3400 equal-sized pixels, corresponding to
578 a platescale of 0.2 arcsec. per pixel. Each **deep_coadd**
579 contains the science image (i.e., the coadd), a variance

Table 3. Number of raw per field and band.

Field Code	Band						Total
	u	g	r	i	z	y	
47_Tuc	54	90	288	171	0	45	648
ECDFS	387	2070	2133	1455	1377	270	7692
EDFS_comcam	180	549	783	378	378	180	2448
Fornax_dSph	0	45	225	108	0	0	378
Rubin_SV_095_-25	297	738	756	207	540	90	2628
Rubin_SV_38_7	0	396	360	495	180	0	1431
Seagull	90	333	387	0	90	0	900
Total	1008	4221	4932	2814	2565	585	16125

image, and a pixel mask; all three contain the same number of pixels. Each `deep_coadd` also contains a position-dependent PSF model (which is the weighted sum of the PSF models of the input `visit_images`), WCS information, plus various `metadata`.

Since coadds always cover an entire `patch`, it is fairly common for a `deep_coadd` to contain regions that were not covered by any of the selected `visit_images`, particularly if the `patch` is on the outskirts of a field and was thus not fully observed. By the nature of how coadds are produced, such regions may contain seemingly valid `flux` values (i.e., not necessarily zeros or NaNs), but will instead be flagged with the `NO_DATA` flag in the pixel mask. It is therefore crucial that the pixel mask is referred to when analyzing `deep_coadds`.

- `template_coadds` (NSF-DOE Vera C. Rubin Observatory 2025d) are those created to use as templates for difference imaging, i.e., the process of subtracting a template image from a `visit_image` to identify either variable or `transient` objects.⁹ As with `deep_coadds`, `template_coadds` are produced by warping and co-adding multiple `visit_images` covering a given skymap-defined `patch`. The process of building `template_coadds` is the same as that for `deep_coadds`, but the selection criteria differ between the two types of coadd. In the case of `template_coadds`, the third of `visit_images` covering the `patch` in question with the smallest PSF FWHM are selected. If one third corresponds to fewer than twelve `visit_images` (i.e., there are fewer than 36 `visit_images` covering the `patch`), then the twelve `visit_images` with the smallest PSF FWHM are selected. Finally, if there are fewer than twelve `visit_images` covering the `patch`, then

⁹ It should be noted that `template_coadds` are not themselves subtracted from `visit_images` but are, instead, warped to match the WCS of a `visit_image`. It is this warped template that is subtracted from the `visit_image` to create a difference image. For storage space reasons, warped templates are not retained for DP1, as they can be readily and reliably recreated from the `template_coadds`.

all `visit_images` are selected. Of the 15972 `visit_images`, N were used to create `template_coadds`. This selection strategy is designed to optimize for seeing when a `patch` is well-covered by `visit_images`, yet still enabling the production of `template_coadds` for poorly-covered patches.

There are a total of 2730 `template_coadds` in DP1.¹⁰ As with `deep_coadds`, a single `template_coadd` covers a single `patch`. Since the same `skymap` is used when creating both `deep_coadd` and `template_coadds`, the on-sky area and pixel count of `template_coadds` are the same as that of a `deep_coadd` (see above). Similarly, `template_coadds` contain the science image (i.e., the coadd), a variance image, and a pixel mask; all three contain the same number of pixels. Also included is the PSF model, WCS information, and `metadata`. As is the case for `deep_coadd`, those pixels within `template_coadds` that are not covered by any of the selected `visit_images` may still have seemingly valid values, but are indicated with the `NO_DATA` flag within the pixel mask.

- `difference_images` (NSF-DOE Vera C. Rubin Observatory 2025e) are generated by the subtraction of the warped, scaled, and PSF-matched `template_coadd` from the `visit_image` (see §4.6.1). In principle, only those sources whose `flux` has changed relative to the `template_coadd` should be apparent (at a significant level) within a `difference_image`. In practice, however, there are numerous spurious sources present in `difference_images` due to unavoidably imperfect template matching.

In total, there are 15972 `difference_images` in DP1, one for each `visit_image`.

Like `visit_images`, `difference_images` contain the science (i.e., difference) image, a variance image, and a pixel mask; all three contain the same number of

¹⁰ The difference in the number of `deep_coadds` and `template_coadds` is due to the difference in the `visit_image` selection criteria for each coadd.

pixels, which is the same as that of the input `visit_image`. Also included is the PSF model, WCS information, and `metadata`.

- Background images contain the model `background` that has been generated and removed from a science image. `visit_images`, `deep_coadds` and `template_coadds` all have associated `background` images.¹¹ Background images contain the same number of pixels as their respective science image, and there is one `background` image for each `visit_image`, `deep_coadd`, and `template_coadd`. Difference imaging analysis also measures and subtracts a `background` model, but the `difference_background` data product is not written out by default and is not part of DP1.

Background images are not available via the IVOA Service; they can only be accessed via the Butler Data Service.

3.2. Catalogs

Here we describe science-ready tables produced by the science pipelines. All but one of the catalogs described here contain data for detections in the images described in §3.1, the exception being the `Calibration` catalog that contains reference data obtained from previous surveys. Observatory-produced `metadata` tables are described in §3.4

The Rubin Observatory has adopted the convention by which single-epoch detections are referred to as sources. By contrast, the astrophysical object associated with a given detection is referred to as an object.¹² As such, a given object will likely have multiple associated sources, since it will be observed in multiple epochs. Each type of catalog contains measurements for either sources or objects detected in one of `visit_images`, `deep_coadds`, or `difference_images`.

While the `Source`, `Object`, `ForcedSource`, `DiaSource`, `DiaObject`, and `ForcedSourceOnDiaObject` catalogs described below each differ in terms of their specific columns, in general they each contain: one or more unique identification number, positional information, one or more types of `flux` measurements (e.g., aperture fluxes, PSF fluxes, Gaussian fluxes, etc.), and a series of boolean flags (indicating, for example, whether the source/object is affected by saturated pixels, cosmic rays, etc.) for each source/object. The Solar System catalogs `SSObject` and `SSSource` deviate from this general structure in that they instead contain orbital parameters for all known asteroids. Where applicable, all measured properties are reported with their associated 1σ uncertainties.

Since DP1 is a preview, it doesn't include all the catalogs expected in a full `LSST Data Release`. Additionally, the catalogs it does include may be missing some columns planned for future releases. Where this is the case, we note what data is missing in the catalog descriptions that follow.

¹¹ In future data releases, `background` images may be included as part of their respective science image data product.

¹² We caution that this nomenclature is not universal; for example, some surveys call “detections” what we call “sources”, and use the term “sources” for what we call “objects”.

Catalog data are stored in the `Qserv` database (§6.5.1) and are accessible via `Table Access Protocol (IVOA standard) (IVOA)`, and an online DP1 catalog schema is available at <https://sdm-schemas.lsst.io/dp1.html>. Catalog data are also accessible via the `Data Butler` (§6.2.2).

- The `Source` catalog (`NSF-DOE Vera C. Rubin Observatory 2025f`) contains data on all sources which are, prior to deblending, detected with a greater than 5σ significance in each individual visit. The detections reported in the `Source` catalog have undergone deblending; in the case of blended detections, only the deblended sources are included in the `Source` catalog. It is important to note that while the criterion for inclusion in a `Source` catalog is a $> 5\sigma$ detection in a `visit_image` prior to deblending, the positions and fluxes are reported post-deblending. Hence, it is possible for the `Source` catalog to contain sources whose `flux-to-error` ratios – potentially of all types (i.e., aperture `flux`, `PSF flux`, etc.) – are less than 5.

In addition to the general information mentioned above (i.e., IDs, positions, fluxes, flags), the `Source` catalog also include basic `shape` and extendedness information.

The `Source` catalog contains data for 46 million sources in DP1.

- The `Object` catalog (`NSF-DOE Vera C. Rubin Observatory 2025g`) contains data on all objects detected with a greater than 5σ significance in the `deep_coadds`. With coadd images produced on a per-band basis, a $> 5\sigma$ detection in one or more of the bands will result in an object being included in the `Object` catalog. For cases where an object is detected at $> 5\sigma$ in more than one band, a cross-matching has been performed between bands to associate an object in one band with its counterpart(s) in the other bands. As such, unlike the `Source` catalog, the `Object` catalog contains data from multiple bands. The objects reported in the `Object` catalog have also undergone deblending; in the case of blended detections, only the deblended child objects are included in the catalog. As with the `Source` catalog, the criterion for inclusion in the `Object` catalog is a $> 5\sigma$ detection in one of the `deep_coadds` prior to deblending, yet the positions and fluxes of objects are reported post-deblending. Hence, it is possible for `Object` catalog to contain objects whose `flux-to-error` ratios — potentially of all types and in all bands — are less than 5.

In addition to the general information mentioned above (i.e., IDs, positions, fluxes, flags), the `Object` catalog also includes basic `shape` and extendedness information. While they may be included in future data releases, no photometric redshifts, Petrosian magnitudes (V. Petrosian 1976), proper motions or periodicity information is included in the DP1 object catalogs. The `Object` catalog contains data for 2.3 million objects in DP1.

- The `ForcedSource` catalog (`NSF-DOE Vera C. Rubin Observatory 2025h`) contains forced PSF photom-

etry measurements performed on both `difference_images` (i.e., the `psfDiffFlux` column) and `visit_images` (i.e., the `psfFlux` column) at the positions of all the objects in the `Object` catalog. We recommend using the `psfDiffFlux` column when generating lightcurves because they are less sensitive to flux from neighboring sources. As well as `forced photometry PSF` fluxes, a range of boolean flags are also included in the `ForcedSource` catalog.

The `ForcedSource` catalog contains a total of 269 million entries across 2.3 million unique objects.

- The `DiaSource` catalogs (NSF-DOE Vera C. Rubin Observatory 2025i) contains data on all the sources detected at a $> 5\sigma$ significance — including those associated with known Solar System objects — in the `difference_images`. Unlike sources detected in `visit_image`, sources detected in difference images (hereafter, “DiaSources”) have gone through an association step during which an attempt has been made to associate them with into underlying objects called “DiaObject”s. The `DiaSource` catalog consolidates all this information across multiple visits and bands. The detections reported in the `DiaSource` catalog have not undergone deblending.

The `DiaSource` catalog contains data for 3.1 million `DiaSources` in `DP1`.

- The `DiaObject` catalog (NSF-DOE Vera C. Rubin Observatory 2025j) contains the astrophysical objects that `DiaSources` are associated with (i.e., the “DiaObjects”). The `DiaObject` catalog only contains non-Solar System Objects; Solar System Objects are, instead, recorded in the `SSObject` catalog (see below for a description of the `SSObject` catalog). When a `DiaSource` is identified, the `DiaObject` and `SSObject` catalogs are searched for objects to associate it with. If no association is found, a new `DiaObject` is created and the `DiaSource` is associated to it. Along similar lines, an attempt has been made to associate `DiaObjects` across multiple bands, meaning the `DiaObject` catalog — like the `Object` catalog — contains data from multiple bands. Since `DiaObjects` are typically `transient` or `variable` (by the nature of their means of detection), the `DiaObject` catalog contains summary statistics of their fluxes, such as the mean and standard deviation over multiple epochs; users must refer to the `ForcedSourceOnDiaObject` catalog (see below) or the `DisSource` catalog for single `epoch flux` measurements of `DiaObjects`.

The `DIAObject` catalogs contains data for 1.1 million `DiaObjects` in `DP1`.

- The `ForcedSourceOnDiaObject` catalog (NSF-DOE Vera C. Rubin Observatory 2025k) is equivalent to the `ForcedSource` catalog, but contains `forced photometry` measurements obtained at the positions of all the `DiaObjects` in the `DiaObject` catalog.

The `ForcedSourceOnDiaObject` catalog contains a total of 197 million entries across 1.1 million unique `DiaObjects`.

- The `CcdVisit` catalog (NSF-DOE Vera C. Rubin Observatory 2025l) contains data for each individual processed `visit_image`. In addition to technical information, such as the on-sky coordinates of the central pixel and measured pixel scale, the `CcdVisit` catalog contains a range of data quality measurements, such as whole-image summary statistics for the `PSF` size, zeropoint, sky `background`, sky noise, quality of `astrometry` solution. It provides an efficient method to access `visit_image` properties without needing to access the image data.

The `CcdVisit` catalog contains entries summarizing data for all 16071 `visit_images`.

- The `SSObject` catalog (NSF-DOE Vera C. Rubin Observatory 2025a)..... Two tables, named `Minor Planet Center Orbit database` () and `SSObject`, carry information about Solar System Objects. The `MPCORB` table provides the Minor Planet Center-computed orbital elements for all known asteroids, including Rubin-discovered. For `DP1`, the `SSObject` serves primarily to provide the mapping between the `International Astronomical Union (IAU)` designation of an object (listed in `MPCORB`), and the internal `ssObjectId` identifier (used as a key to find solar system object observations in the `DiaSource` and `SSSource` tables).

- The `SSSource` catalog (NSF-DOE Vera C. Rubin Observatory 2025b) contain data on all `DiaSources` that are either associated with previously-known Solar System Objects, or have been confirmed as newly-discovered Solar System Objects by confirmation of their orbital properties. As entries in the `SSSource` catalog stem from the `DiaSource` catalog, they have all been detected at $> 5\sigma$ significance.

The `SSSource` catalog contains data for 5988 Solar System Sources.

- The `Calibration` catalog is the reference catalog that was used to perform astrometric and photometric `calibration`. It is a whole-sky catalog built specifically for `LSST`, as no prior reference catalog had both the depth and coverage needed to calibrate `LSST` data. It combines data from multiple previous reference catalogs and contains only stellar sources. Full details on how the `Calibration` catalog was built are provided in P. Ferguson et al. (2025) (in which it is referred to as “The Monster”), but we provide a brief summary here.

For the *grizy* bands, the input catalogs were (in order of priority): `Dark Energy Survey (DES) Y6 Calibration Stars` (E. S. Rykoff et al. 2023); `Gaia-B or R Photometry (Gaia)` () `Synthetic Magnitudes` (Gaia Collaboration et al. 2023); the `Panoramic Survey Telescope and Rapid Response System (Pan-STARRS)1 3pi survey` (K. C. Chambers et al. 2016); `Data Release 2 of the the SkyMapper survey` (C. A. Onken et al. 2019); and `Data Release 4 of the Very Large Telescope (European Southern Observatory (ESO)) (ESO) Survey Telescope (ESO) Asteroid Terrestrial-impact Last Alert System` () survey (T. Shanks et al. 2015). For the

874 *u*-band, the input catalogs were (in order of priority):
 875 Standard Stars from [Sloan Digital Sky Survey \(\) Data](#)
 876 [Release 16](#) (R. Ahumada et al. 2020); [Gaia-XP Syn-](#)
 877 [thetic Magnitudes](#) ([Gaia Collaboration et al. 2023](#));
 878 and synthetic magnitudes generated using [Stellar Lo-](#)
 879 [cus Regression \(SLR\)](#), which estimates the *u*-band flux
 880 from the *g*-band flux and *g-r* colors. This latter input
 881 (i.e., SLR estimates) was used to boost the number of
 882 *u*-band reference sources, as otherwise the source density
 883 from the *u*-band input catalogs is too low to be
 884 useful for the large footprint of the LSST.

885 Only high quality stellar sources were selected from
 886 each input catalog. Throughout, the `Calibration` cat-
 887 alog uses the `DES` bandpasses for the *grizy*-bands and
 888 the `SDSS` bandpass for the *u*-band; color transforma-
 889 tions derived from high quality sources were used to
 890 convert fluxes from the various input catalogs (some
 891 of which did not use the `DES/SDSS` bandpasses) to
 892 the respective bandpasses. All sources from the in-
 893 put catalogs are matched to [Gaia-Data Release 3 \(\)](#)
 894 sources for robust astrometric information, selecting
 895 only isolated sources (i.e., no neighbors within 1").

896 Once the input catalogs had been collated and
 897 fluxes transformed to the standard `DES/SDSS`
 898 bandpasses, the `LSST Science Pipeline's`
 899 `ConvertReferenceCatalogTask` was used to shard
 900 the catalog, which allows it to be quickly searched for
 901 sources covering a particular `patch` of sky, and create
 902 a set of standard columns containing positional and
 903 flux information, including uncertainties.

904 3.3. Maps

905 Maps are two-dimensional visualizations of survey data.
 906 In DP1, these fall into two categories: Survey Property
 907 Maps and [Hierarchical Progressive Survey \(IVOA standard\)](#)
 908 (IVOA) Maps (P. Fernique et al. 2015).

909 3.3.1. Survey Property Maps

910 Survey Property Maps ([NSF-DOE Vera C. Rubin Obser-](#)
 911 [vatory 2025](#)) summarize how properties such as observing
 912 conditions or exposure time vary across the observed sky.
 913 Each map provides the spatial distribution of a specific quan-
 914 tity at a defined sky position for each band by aggregating
 915 information from the images used to make the `deep_coadd`.
 916 Maps are initially created per-tract and then combined to
 917 produce a final consolidated map. At each sky location, rep-
 918 resented by a spatial pixel in the [Hierarchical Equal-Area](#)
 919 [iso-Latitude Pixelisation \(HEALPix\)](#) grid, values are derived
 920 using statistical operations, such as minimum, maximum,
 921 mean, weighted mean, or sum, depending on the property.

922 There are 29 survey property maps in DP1. The
 923 available maps describe total exposure times, observa-
 924 tion epochs, PSF size and `shape`, PSF magnitude lim-
 925 its, sky `background` and noise levels, as well as astro-
 926 metric shifts and PSF distortions due to wavelength-
 927 dependent atmospheric [Differential Chromatic Refraction \(\)](#)
 928 effects. They all use the dataset type format `deep_coadd_`
 929 `<PROPERTY>_consolidated_map_<STATISTIC>` e.g. `deep_`
 930 `coadd_exposure_time_consolidated_map_sum` provides a

931 spatial map of the total exposure time accumulated per
 932 sky position in units of seconds. All maps are stored in
 933 `HealSparse`¹³(K. M. Górski et al. 2005) format. Survey
 934 property maps are only available via the `Data Butler` (§6.2.2)
 935 and have dimensions `band` and `skymap`.

936 Figure 8 presents three survey property maps for exposure
 937 time, PSF magnitude limit, and sky noise, computed for rep-
 938 resentative tracts and bands. Because full consolidated maps
 939 cover widely separated tracts, we use clipped per-tract views
 940 here to make the spatial patterns more discernible.

942 3.3.2. HiPS Maps

943 HiPS Maps (P. Fernique et al. 2015), offer an interac-
 944 tive way to explore seamless, multi-band tiles of the sky
 945 regions covered by DP1, allowing for smooth panning and
 946 zooming. DP1 provides multi-band HiPS images created by
 947 combining data from individual bands of `deep_coadd` and
 948 `template_coadd` images. These images are false-color repre-
 949 sentations generated using various filter combinations for the
 950 red, green, and blue channels. The available filter combina-
 951 tions include *gri*, *izy*, *riz*, and *ugr* for both `deep_coadd` and
 952 `template_coadd`. Additionally, for `deep_coadd` only, we pro-
 953 vide color blends such as *uug* and *grz*. Post-DP1, we plan to
 954 also provide single-band HiPS images for all *ugrizy* bands in
 955 both [Portable Network Graphics \(PNG\)](#) and [Flexible Image](#)
 956 [Transport System \(\)](#) formats.

957 HiPS maps are only accessible through the HiPS viewer in
 958 the [Rubin Science Platform \(\) Portal](#) (§6.3) and cannot be
 959 accessed via the `Data Butler` (§6.2.2). All multi-band HiPS
 960 images are provided in PNG format.

961 3.4. Metadata

962 DP1 also includes `metadata` about the observations, which
 963 is stored in the `Visit` table. The data it contains is produced
 964 by the observatory directly, rather than the science pipelines.
 965 It contains technical data for each visit, such as telescope
 966 pointing, `camera` rotation, `airmass`, exposure start and end
 967 time, and total exposure time.

968 3.5. Ancillary Data Products

969 DP1 also includes several ancillary data products. While
 970 we do not expect most users to need these, we describe them
 971 here for completeness. All the Data Products described in
 972 this section can only be accessed via the `Data Butler` (§6.2.2).

973 3.5.1. Task configuration, log, and metadata

974 DP1 includes `provenance`-related data products such as
 975 task logs, `configuration` files, and task metadata. Configura-
 976 tion files record the parameters used in each processing task,
 977 while logs and `metadata` contain information output during
 978 processing. These products help users understand the pro-
 979 cessing setup and investigate potential processing failures.

13 A sparse HEALPix representation that efficiently encodes data values on the celestial sphere. <https://healsparse.readthedocs.io>

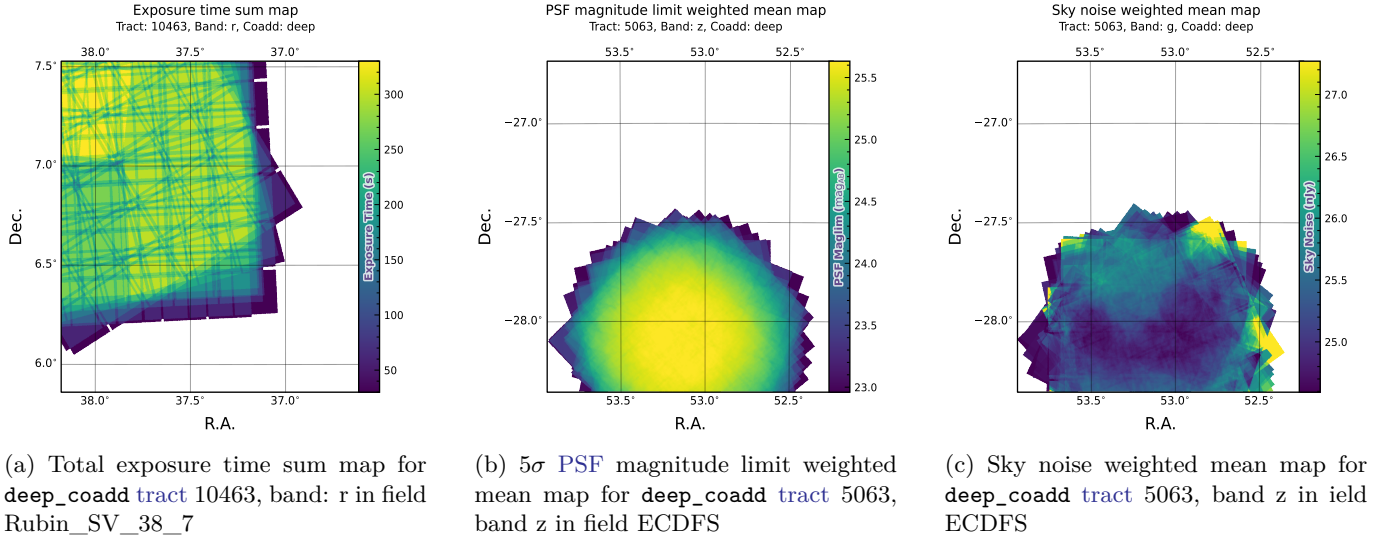


Figure 8. Examples of survey property maps from Rubin DP1 across different bands, clipped to the boundary of a single tract for visual clarity.

3.5.2. Pipeline-generated plots and metrics

DP1 includes various plots and metrics generated during data processing, such as plots comparing measured fluxes and source positions relative to references, and metrics indicating the numbers of flagged pixels in a given `visit_image`. These data products are predominantly used by the data management team to assess the quality of the processed data. We include them with DP1 for transparency.

3.5.3. Calibration Data Products

Calibration data products include a variety of images and models that are used to characterize and correct the performance of the camera and other system components. These include bias, dark, and flat-field images, Photon Transfer Curve (PTC) gains, brighter-fatter kernels, charge transfer inefficiency (CTI) models, linearizers, and illumination corrections. For flat-field corrections, DP1 processing used combined flats, which are averaged from multiple individual flat-field exposures to provide a stable calibration. These calibration products are essential inputs to Instrument Signal Removal (ISR) (§4.2.1). While these products are included in DP1 for transparency and completeness, users should not need to rerun ISR for their science and are advised to start with the processed `visit_image`.

3.5.4. Standard Bandpasses

The `standard_passband` data products contain the system throughputs described in §2.2.1.

4. DATA RELEASE PROCESSING

Data Release Processing () is the systematic reprocessing of all Rubin Observatory data collected up to a certain date to produce the calibrated images, catalogs of detections, and derived data products described in Section 3. DP1 was pro-

cessed entirely at the United States Data Facility (USDF), using 17,024 CPU hours.¹⁴

This section describes the pipeline algorithms used to produce DP1 and how they differ from those planned for full-scale LSST data releases. Data Release Production consists of four major stages: (1) single-frame processing, (2) calibration, (3) coaddition, and (4) difference imaging analysis (Difference Image Analysis ()).

4.1. LSST Science Pipelines Software

The LSST Science Pipelines software (Rubin Observatory Science Pipelines Developers 2025; J. Swinbank et al. 2020) will be used to generate all Rubin Observatory and LSST data products. It provides both the algorithms and middleware frameworks necessary to process raw data into science-ready products, enabling analysis by the Rubin scientific community. Version v29.1 of the pipelines was used to produce DP1. Documentation for this version is available at: https://pipelines.lsst.io/v/v29_1_1

4.2. Single Frame Processing

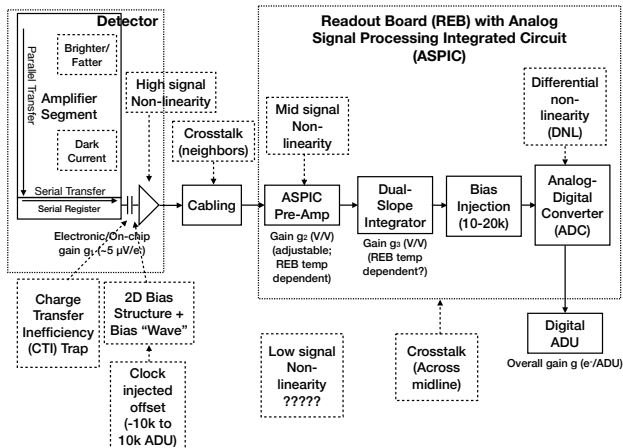
4.2.1. Instrument Signature Removal

The first step in processing LSSTComCam images is to correct for the effects introduced by the telescope and detector. Each sensor and its readout amplifiers can vary slightly in performance, causing images of even a uniformly illuminated focal plane to exhibit discontinuities and shifts due to detector effects. The ISR pipeline aims to recover the original astrophysical signal as best as possible and produce science-ready single-epoch images for source detection and measurement (see P. Fagrelus & E. Rykoff 2025; A. A.

¹⁴ For future Data Releases, data processing will be distributed across the USDF, the French Data Facility (FrDF) and the United Kingdom Data Facility (UKDF).

1040 Plazas Malagón et al. 2025 for a detailed description of the
1041 ISR procedures).

1042 Figure 9 illustrates the model of detector components and
1043 their impact on the signal, tracing the process from photons
1044 incident on the detector surface to the final quantized
1045 values recorded in the image files. The ISR pipeline essentially
1046 “works backward” through the signal chain, correcting
1047 the integer analog-to-digital units (ADU) raw camera output
1048 back to a floating-point number of photoelectrons created in
1049 the silicon. The physical detector, shown on the left in Figure
1050 9, is the source of effects that arise from the silicon itself,
1051 such as the dark current and the brighter-fatter effect (A. A.
1052 Plazas et al. 2018; A. Broughton et al. 2024). After the image
1053 has integrated, the charge is shifted to the serial register and
1054 read out, which can introduce charge transfer inefficiencies
1055 and a clock-injected offset level. The signals for all ampli-
1056 fiers are transferred via cables to the Readout Electronics
1057 Board (REB), during which crosstalk between the amplifiers
1058 may occur. The Analog Signal Processing Integrated Circuit
1059 (ASPIC) on the REB converts the analog signal from the
1060 detector into a digital signal, adding both quantization
1061 and a bias level to the image. Although the signal chain is
1062 designed to be stable and linear, the presence of numerous
1063 sources of non-linearity indicates otherwise.



1064 **Figure 9.** The model of the detector and REB components,
1065 labeled with the effects that they impart on signal.

1066 The ISR processing pipeline for DP1 performs, in the fol-
1067 lowing order: **Analog-to-Digital Unit (ADU)** dithering to
1068 reduce quantization effects, serial overscan subtraction, sat-
1069 uration masking, gain normalization, crosstalk correction,
1070 parallel overscan subtraction, linearity correction, serial CTI
1071 correction, image assembly, bias subtraction, dark subtraction,
1072 brighter-fatter correction, defect masking and interpo-
1073 lation, variance plane construction, flat fielding, and ampli-
1074 fier offset (amp-offset) correction¹⁵. Flat fielding for DP1

¹⁵ Amp-offset corrections are designed to address systematic dis-
continuities in background sky levels across amplifier bound-
aries. The implementation in the LSST Science Pipelines is

1075 was performed using combined flats produced from twilight
1076 flats acquired with sufficient rotational dithering to mitigate
1077 artifacts from print-through stars, as described in §2.3.

1078 4.2.2. Background Subtraction

1079 The background subtraction algorithms in the LSST Sci-
1080 ence Pipelines estimate and remove large-scale background
1081 signals from science imaging. Such signals may include sky
1082 brightness from airglow, moonlight, scattered light instru-
1083 mental effects and diffuse astrophysical emission. In so do-
1084 ing, true astrophysical sources are isolated to allow for accu-
1085 rate detection and measurement.

1086 To generate a **background** model, each post-ISR image is
1087 divided into superpixels of 128×128 pixels. Pixels with a
1088 mask flag set that indicates that they contain no useful sci-
1089 ence data or that they contain flux from a preliminary source
1090 detection are masked. The iterative 3σ clipped mean of the
1091 remaining pixels is calculated for each superpixel, construct-
1092 ing a **background** statistics image. A sixth-order Chebyshev
1093 polynomial is fit to these values to allow for an extrapolation
1094 back to the native pixel resolution of the post-ISR image.

1095 4.3. Calibration

1096 Stars are detected in each post-ISR image using a 5σ
1097 threshold. Detections of the same star across multiple im-
1098 ages are then associated to identify a consistent set of iso-
1099 lated stars with repeated observations suitable for use in PSF
1100 modeling, photometric **calibration**, and astrometric **calibra-**
1101 **tion**.

1102 Initial astrometric and photometric solutions are derived
1103 using only the calibration reference catalogs (see §3.2), and
1104 an initial PSF model is fit using PSFEx (E. Bertin 2011).
1105 These preliminary solutions provide approximate source posi-
1106 tions, fluxes, and PSF shapes that serve as essential inputs
1107 to the **calibration** process, enabling reliable source matching,
1108 selection of high-quality stars, and iterative refinement of
1109 the final astrometric, photometric, and PSF models. These
1110 preliminary solutions are subsequently replaced by more ac-
1111 curate fits, as described in the following sections.

1112 4.3.1. PSF Modeling

1113 PSF modeling in DP1 uses the Piff (M. Jarvis et al. 2021)
1114 algorithm. Piff models represent the PSF on a pixel-by-pixel
1115 basis and interpolate its parameters across a single CCD
1116 using two-dimensional polynomials. Piff utilizes its Pixel
1117 grid model with a fourth-order polynomial interpolation per
1118 CCD, except in the u-band, where star counts are insufficient
1119 to support a fourth-order fit. In this case, a second-order
1120 polynomial is used instead. Details on the choice of poly-
1121 nomial order, overall PSF modeling performance, and known
1122 issues are discussed in §5.2.

1123 4.3.2. Astrometric Calibration

1124 Starting from the astrometric solution calculated in sin-
1125 gle frame processing §4.2, the final astrometric solution is

based on the Pan-STARRS Pattern Continuity algorithm (C. Z.
Waters et al. 2020)

computed using the ensemble of visits in a given band that overlap a given *tract*. This allows the astrometric solution to be further refined by using all of the isolated point sources of sufficient signal-to-noise ratio in an image, rather than only those that appear in the reference catalog (as is done in single frame processing). Using multiple whole visits rather than a single detector also allows us to account for effects that impact the full focal plane and for the proper motion and parallax of the sources.

In order to perform the fit of the astrometric solution, isolated point sources are associated between overlapping visits and with the Gaia DR3 reference catalog where possible. The model used for DP1 consists of a static map from pixel-space to an intermediate frame (the per-detector model), followed by a per-visit map from the intermediate frame to the plane tangent to the telescope boresight (the per-visit model), then finally a deterministic mapping from the tangent plane to the sky. The fit is done using the *gbdes* package (G. M. Bernstein et al. 2017), and a full description is given in C. Saunders (2024).

The per-detector model is intended to capture quasi-static characteristics of the telescope and camera. During Rubin Operations, the astrometric solution will allow for separate epochs with different per-detector models, to account for changes in the camera due to warming and cooling and other discrete events. However, for DP1, LSSTComCam was assumed to be stable enough that all visits use the same per-detector model. The model itself is a separate two-dimensional polynomial for each detector. For DP1, a degree 4 polynomial was used; the degree of the polynomial mapping is tuned for each instrument and may be different for LSSTCam. Further improvements may be made by including a pixel-based astrometric offset mapping, which would be fit from the ensemble of astrometric residuals, but this is not included in the DP1 processing.

The per-visit model attempts to account for time-varying effects on the path of a photon from both atmospheric sources and those dependent on the telescope position. This model is also a polynomial mapping, in this case a degree 6 two-dimensional polynomial. Correction for DCR was not done for DP1, but will be included in LSSTCam processing during Operations. Future processing will also likely include a Gaussian Processes fit to better account for atmospheric turbulence, as was demonstrated in W. F. Fortino et al. (2021) and P. F. Léget et al. (2021).

The last component of the astrometric calibration is the position of the isolated point sources included in the fit. The positions consist of five parameters: position on the sky, proper motion, and parallax. The reference epoch for the fit positions is 2024.9.

4.3.3. Photometric Calibration

Photometric calibration of the DP1 dataset is based on the Forward Global Calibration Method (FGCM D. L. Burke et al. 2018), adapted for the LSST Science Pipelines (H. Aihara et al. 2022; P. Fagrelus & E. Rykoff 2025). We used Forward Global Calibration Model (FGCM) to calibrate the full DP1 dataset with a forward model that uses a parameterized model of the atmosphere as a function of airmass

along with a model of the instrument throughput as a function of wavelength. The FGCM process typically begins with measurements of the instrumental throughput, including the mirrors, filters, and detectors. However, because full scans of the LSSTComCam as-built filters and individual detectors were not available, we instead used the nominal reference throughputs for the Simonyi Survey Telescope and LSSTCam.¹⁶ These nominal throughputs were sufficient for the DP1 calibration, given the small and homogeneous focal plane consisting of only 9 ITL detectors. The FGCM atmosphere model, provided by MODTRAN (A. Berk et al. 1999), was used to generate a look-up table for atmospheric throughput as a function of zenith distance at Cerro Pachón. This model accounts for Rayleigh scattering by molecular oxygen (O₂) and ozone (O₃), absorption by water vapor, and Mie scattering by airborne aerosol particulates. Nightly variations in the atmosphere are modeled by minimizing the variance in repeated observations of stars with a Signal to Noise Ratio (SNR) greater than 10, measured using “compensated aperture fluxes”. These fluxes include a local background subtraction (see §4.2.2 to mitigate the impact of background offsets). The model fitting process incorporates all 6 bands (*ugrizy*) but does not include any gray (achromatic) terms, except for a linear assumption of mirror reflectance degradation, which is minimal over the short duration of the DP1 observation campaign. As an additional constraint on the fit, we use a subset of stars from the reference catalog (P. Ferguson et al. 2025), primarily to constrain the system’s overall throughput and establish the “absolute” calibration.

4.4. Visit Images and Source Catalogs

With the final PSF models, WCS solutions, and photometric calibrations in place, we reprocess each single-epoch image to produce a final set of calibrated visit images and source catalogs. Source detection is performed down to a 5 σ threshold using the updated PSF models, followed by measurement of PSF and aperture fluxes. These catalogs represent the best single-epoch source characterization, but they are not intended for constructing light curves. For time-domain analysis, we recommend using the forced photometry tables described in §4.6.2

4.5. Coaddition Processing

4.5.1. Coaddition

Only exposures with a seeing better than 1.7 arcseconds FWHM are included in the deep coadded images. For the template coadds, only the top third of visits with the best seeing are used, resulting in an even tighter image quality cutoff for the template coadds.

Exposures with poor PSF model quality, identified using internal diagnostics, are excluded to prevent contamination of the coadds with unreliable PSF estimates. The remaining exposures are combined using an inverse-variance weighted mean stacking algorithm. To mitigate transient artifacts before coaddition, we apply the artifact rejection procedure

¹⁶ Available at: <https://github.com/lstt/throughputs/tree/1.9>

described in Y. AlSaiyad (2019) that identifies and masks features such as satellite trails, optical ghosts, and cosmic rays. It operates on a time series of PSF-matched images re-sampled onto a common pixel grid (“warps”) and leverages their temporal behavior to distinguish persistent astrophysical sources from transient artifacts.

Artifact rejection uses both direct and PSF-matched warps, homogenized to a standard PSF of 1.8 arcseconds FWHM, consistent with the seeing threshold used in data screening. A sigma-clipped mean of the PSF-matched warps serves as a static sky model, against which individual warps are differenced to identify significant positive and negative residuals. Candidate artifact regions are classified as **transient** if they appear in less than a small percentage of the total exposures, with the threshold varying based on the number of visits, N , as follows:

- $N = 1$ or 2 : threshold = 0 (no clipping).
- $N = 3$ or 4 : threshold = 1.
- $N = 5$: threshold = 2.
- $N > 5$: threshold = $2 + 0.03N$.

Identified **transient** regions are masked before coaddition, improving image quality and reducing contamination in derived catalogs.

4.5.2. Coadd Processing

Coadd-processing consists of detection, **deblending**, and measurement on coadds to produce object tables (§3.2). For each coadd in all six bands, we fit a constant **background** and performed source detection at a 5σ detection threshold. Detections across bands are merged in a fixed priority order, *irzygu*, to form a union detection catalog, which serves as input to deblending.

Deblending is performed using the Scarlet Lite algorithm, which implements the same model as Scarlet (P. Melchior et al. 2018), but operates on a single pixel grid. This allows the use of analytic gradients, resulting in greater computational speed and memory efficiency.

Source measurement is then performed on the deblended footprints in each band. Measurements are conducted in three modes: independent per-band measurements, forced measurements in each band, and multiband measurements. Most measurement algorithms operate through a single-band plugin system, largely as originally described in J. Bosch et al. (2018). These plugins run on a deblended image, which is generated by using the Scarlet model as a template to re-weight the original noisy coadded pixel values. This effectively preserves the original image in regions where objects are not blended, while dampening the noise elsewhere.

Measurement **algorithm** outputs include object fluxes, centroids, and higher-order moments thereof like sizes and shapes.

A reference band is then chosen for each object based on detection significance and measurement quality using the same priority order as detection merging (*irzygu*) and a second round of measurements is performed in forced mode using the shape and position from the reference band to ensure consistent colors (J. Bosch et al. 2018). A variety of

flux measurements are included in the object tables, from aperture fluxes and forward modeling algorithms.

Composite model (CModel) magnitudes are used to calculate the extendedness parameter, which functions as a star-galaxy classifier. Gaussian-aperture-and-PSF (GAaP K. Kuijken 2008; A. Kannawadi 2022) fluxes are provided to ensure consistent galaxy colors across bands. Sersic model fits are run on all available bands simultaneously (Multi-ProFit D. S. Taranu 2025). The resulting Sersic (J. L. Sérsic 1963; J. L. Sérsic 1968) model fluxes are provided as an alternative to CModel and are intended to represent total galaxy fluxes. Like CModel, the Sersic model is a Gaussian mixture approximation to a true Sersic profile, convolved with a Gaussian mixture approximation to the PSF. CModel measurements use a double “shapelet” (A. Refregier 2003) PSF with a single shared shape, while the Sersic fits use a double Gaussian with independent shape parameters for each component. Sersic model fits also include a free centroid, with all other structural parameters shared across all bands. That is, the intrinsic model has no color gradients, but the convolved model may have color gradients if the PSF parameters vary significantly between bands.

Further details on the performance of these algorithms can be found in 5.5.

4.6. Variability Measurement

4.6.1. Difference Imaging Analysis

Difference Image Analysis (DIA) used the decorrelated Alard & Lupton image differencing algorithm (D. J. Reiss & R. H. Lupton 2016). We detected both positive and negative **DIASources** at 5σ in the difference image. Sources with footprints containing both positive and negative peaks were fit with a dipole centroid code.

We filter a subset of **DIASources** that have pixel flags characteristic of artifacts, non-astrophysical trail lengths, and unphysically negative direct fluxes. We performed a simple spatial association of **DIASources** into **DIAObjects** with a one arcsecond matching radius.

To meet the latency requirements for **Alert Production**, we initially developed a relatively simple Machine Learning reliability model: a Convolutional Neural Network with three convolutional layers, and two fully connected layers. The convolutional layers have a 5×5 kernel size, with 16, 32, and 64 filters, respectively. A max-pooling layer of size 2 is applied at the end of each convolutional layer, followed by a dropout layer of 0.4 to reduce overfitting. The last fully connected layers have sizes of 32 and 1. The ReLU activation function is used for the convolutional layers and the first fully connected layer, while a sigmoid function is used for the output layer to provide a probabilistic interpretation. The cutouts are generated by extracting postage stamps of 51×51 pixels centered on the detected source. The input data of the model consists of the template, science, and difference image stacked to have a tensor of **shape** (3, 51, 51). The model is implemented using PyTorch (J. Ansel et al. 2024). The Binary Cross Entropy loss function was used, along with the **Adaptive Moment Estimation (Adam)** optimizer with a fixed learning rate of 1×10^{-4} , weight decay of 3.6×10^{-2} , and a batch size of 128. The final model uses

the weights that achieved the best precision/purity for the test set. Training was done on the SLAC National Accelerator Laboratory () Shared Scientific Data Facility () with an NVIDIA L40S GPU model.

The model was initially trained using simulated data from the second Data Challenge (DC2; (LSST Dark Energy Science Collaboration (LSST DESC) et al. 2021)) plus randomly located injections of PSFs to increase the number of real sources, for a total of 89,066 real sources. The same number of bogus sources were selected at random from non-injected DIASources. Once the LSSTComCam data was available, the model was fine-tuned on a subset of the data containing 183,046 sources with PSF injections. On the LSSTComCam test set, the model achieved an accuracy of 98.06%, purity of 97.87%, and completeness of 98.27%.

4.6.2. Lightcurves

To produce light curves, we perform multi-epoch forced photometry on both the direct visit images and the difference images. For lightcurves we recommend the forced photometry on the difference images (psDiffFlux on the Forced-Source Table), as it isolates the variable component of the flux and avoids contamination from static sources. In contrast, forced photometry on direct images includes flux from nearby or blended static objects, and this contamination can vary with seeing. Centroids used in the multi-epoch forced photometry stage are taken either from object positions measured on the coadds or from the DIAObjects (the associated DIASources detected on difference images).

This stage takes the longest in terms of integrated Central Processing Unit (CPU)-hours.

4.6.3. Solar System Processing

Solar system processing in DP1 consists of two key components: the association of observations (sources) with known solar system objects, and the discovery of previously unknown objects by linking sets of tracklets¹⁷.

To generate expected positions, ephemerides are computed for all objects found in the Minor Planet Center orbit catalog using the Sorcha survey simulation toolkit (Merritt et al., in press)¹⁸. To enable fast lookup of objects potentially present in an observed visit, we use the mpsky package (M. Juric 2025). In each image, the closest DiaSource within 1 arcsecond of a known solar system object’s predicted position is associated to that object.

Solar system discovery uses the helioline package of asteroid identification and linking tools (A. Heinze et al. 2023). The suite consists of the following tasks:

- Tracklet creation with `make_tracklets`
- Multi-night tracklet linking with `heliolinc`
- Linkage post processing (orbit fitting, outlier rejection, and de-duplication) with `link_purify`

¹⁷ A tracklet is defined as two or more observations taken in close succession in a single night.

¹⁸ Available at <https://github.com/dirac-institute/sorcha>

The inputs to the helioline suite included all sources detected in difference images produced by an early processing of the LSSTComCam commissioning data, including some that were later rejected as part of DP1 processing and hence are not part of this DP1 release.

About 10% of all commissioning visits targeted the near-ecliptic field Rubin_SV_38_7 designed to enable asteroid discovery. Rubin_SV_38_7 produced the vast majority of asteroid discoveries, as expected, but a few were found in off-ecliptic fields as well.

Tracklet creation with `make_tracklets` used an upper limit angular velocity of 1.5 deg/day, faster than any main belt asteroid and in the range of many Near-Earth Object () discoveries. To avoid excessive false tracklets from fields that were observed many times per night, the minimum tracklet length was set to three and the minimum on-sky motion for a valid tracklet was set to five arcseconds.

The heart of the discovery pipeline is the heliolinc task, which connects (“links”) tracklets belonging to the same object over a series of nights. It employs the HelioLinC3D algorithm (S. Eggl et al. 2020; A. Heinze et al. 2022), a refinement of the original HelioLinC algorithm of M. J. Holman et al. (2018). The heliolinc run tested each tracklet with 324 different hypotheses spanning heliocentric distances from 1.5 to 9.8 AU and radial velocities spanning the full range of possible bound orbits (eccentricity 0.0 to nearly 1.0). This range of distance encompasses all main belt asteroids and Jupiter Trojans, as well as many comets and Mars-crossers and some NEOs. Smaller heliocentric distances were not attempted here because nearby objects move rapidly across the sky and hence were not likely to remain long enough in an LSSTComCam field to be discovered. A clustering radius was chosen corresponding to 1.33×10^{-3} AU at 1 deprecated acronym for astronomical unit; use astronomical unit (au) instead (au) from Earth. Linkages produced by heliolinc are then post-processed with `link_purify` into a final non-overlapping set of candidate discoveries, ranked from highest to lowest probability of being a real asteroid based on astrometric orbit-fit residuals and other considerations.

5. PERFORMANCE CHARACTERIZATION AND KNOWN ISSUES

In this section, we provide an assessment of the DP1 data quality and known issues. A summary of the Rubin DP1 key numbers and data quality metrics and is found in PERF-SUMMARYTABLE

5.1. Sensor Anomalies and ISR

In addition to the known detector features identified before LSSTComCam commissioning, most of which are handled by the ISR processing (see §4.2.1), we discovered a number of new types of anomalies in the DP1 data. Since no corrections are currently available for these anomalies, they are masked and excluded from downstream data products.

5.1.1. Vampire Pixels

Vampire pixels are visible on the images as a bright defect surrounded by a region of depressed flux, as though the defect is stealing charge from its neighboring pixels; they have

1457 been termed “vampire” defects. From studies on evenly il-
 1458 luminated images, vampires appear to conserve charge. Un-
 1459 fortunately, there’s no clean way to redistribute this stolen
 1460 flux, and so we have identified as many of them as possi-
 1461 ble and created manual defect masks to exclude them from
 1462 processing. We have found some similar features on the ITL
 1463 detectors on LSSTCam, and will use the same approach to
 1464 exclude them.

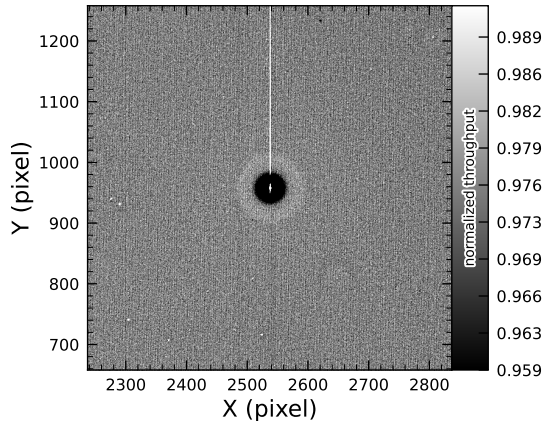


Figure 10. A large *vampire pixel* near the center of R22_
 S11, as seen on the r-band flat.

5.1.2. Phosphorescence

1465
 1466
 1467
 1468 Some regions were seen to contain large numbers of bright
 1469 defects. On closer study, it appears that on some detec-
 1470 tors a layer of photoresist wax was incompletely removed
 1471 from the detector surface during production. As this wax is
 1472 now trapped below the surface coatings, there is no way to
 1473 physically clean these surfaces. If this wax responded to all
 1474 wavelengths equally, then it would likely result in quantum
 1475 efficiency dips, which might be removable during flat cor-
 1476 rection. However, it appears that this wax is slightly phos-
 1477 phorescent, with a decay time on the order of minutes, result-
 1478 ing in the brightness of these sources being dependent on the
 1479 illumination of prior exposures. The worst of these regions
 1480 were excluded with manual masks, but we do not expect to
 1482 need to do this for LSSTCam.

5.1.3. Crosstalk

1483
 1484 We use an average crosstalk correction based on laboratory
 1485 measurements with LSSTCam. These average corrections
 1486 performed better than expected, and so have been used as-
 1487 is for DP1 processing. There are, however, some residual
 1488 crosstalk features present post-correction, with a tendency
 1490 towards over-subtraction.

5.1.4. Bleed Trails

1491
 1492 Bleed trails from saturated sources were expected on
 1493 LSSTComCam, but they appear in more dramatic forms
 1494 than was expected. As a bleed trail nears the serial reg-
 1495 ister, it fans out into a “trumpet” shaped feature. Although

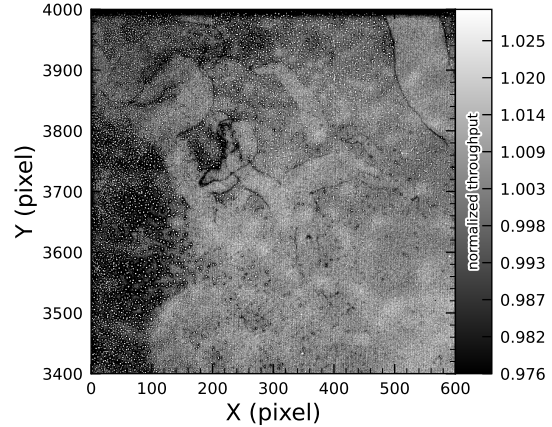


Figure 11. The top left corner of R22_S01 in the g-band
 flat, showing the many small defect features that are caused
 by the remnant photoresist wax. A single large defect box
 masks this region from further analysis to prevent these fea-
 tures from contaminating measurements.

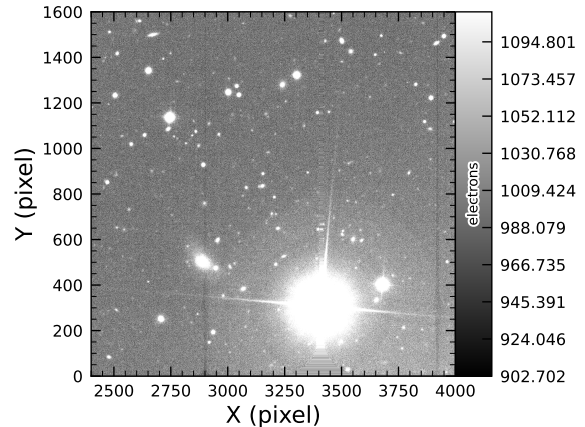


Figure 12. An example of a bright star with over-sub-
 tracted crosstalk residuals visible on neighboring amplifiers
 to both sides (exposure 2024120600239, detector R22_S02).
 The horizontal banding stretching from the center of the star
 shows the interpolation pattern covering the saturated core and
 the ITL edge bleed near the serial register.

1483

1484 We use an average crosstalk correction based on laboratory
 1485 measurements with LSSTCam. These average corrections
 1486 performed better than expected, and so have been used as-
 1487 is for DP1 processing. There are, however, some residual
 1488 crosstalk features present post-correction, with a tendency
 1490 towards over-subtraction.

1491

5.1.4. Bleed Trails

1492 Bleed trails from saturated sources were expected on
 1493 LSSTComCam, but they appear in more dramatic forms
 1494 than was expected. As a bleed trail nears the serial reg-
 1495 ister, it fans out into a “trumpet” shaped feature. Although

1496

1497

1498

1499

1500

1501

1502

1503

1504

1505

1506

1507

bright, these features do not have consistently saturated pix-
 els, and were ignored in the first on-sky processing. We have
 since developed the means to programmatically identify and
 mask these features, which we have named “edge bleeds.”

Saturated sources can create a second type of bleed, where
 the central bleed drops below the background level. The
 depressed columns along these trails extend across the entire
 height of the detector, crossing the detector mid-line. We
 developed a model for these to identify which sources are
 sufficiently saturated to result in such a trail, which is then
 masked. As these kind of trails appear only on the ITL
 detectors, we’ve named these features “ITL dips.”

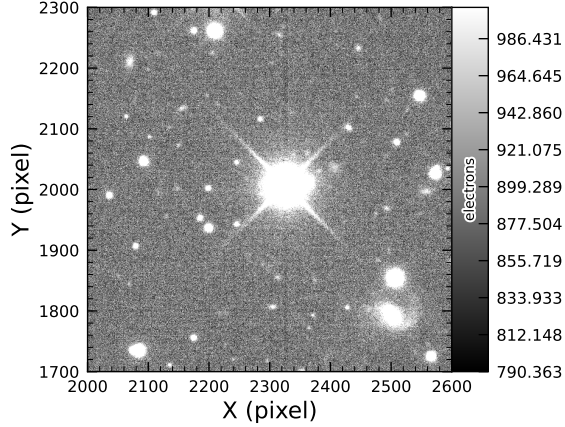


Figure 13. A bright star showing the “ITL dip” phenomenon, in which a dark trail extends out from the star to the top and bottom edges of the detector (exposure: 202412100503, detector: R22_S21).

5.2. PSF Models

To characterize PSF performance, we use the second moments measured on PSF stars and on the PSF model via the Half-Second Moment (HSM) method (C. Hirata & U. Seljak 2003 and R. Mandelbaum et al. 2005), all expressed in the camera’s pixel frame. Given the second-moment matrix elements I_{xx} , I_{yy} , and I_{xy} , we define:

$$\begin{aligned} T &= I_{xx} + I_{yy} \\ e^1 &= \frac{I_{xx} - I_{yy}}{T} \\ e^2 &= \frac{2I_{xy}}{T}. \end{aligned}$$

We denote T_{PSF} , e_{PSF}^1 , and e_{PSF}^2 for measurements on the PSF stars, and T_{model} , e_{model}^1 , and e_{model}^2 for the PSF model. Two variants are compared:

- Piff with second-order polynomial interpolation (default in science pipelines); and
- Piff with fourth-order polynomial interpolation (final DP1 PSF).

Table 4 summarizes each model’s ability to reconstruct the mean T , e^1 , and e^2 on LSSTComCam. Piff shows a negative residual bias in size. We will explore this further by plotting $\delta T/T$ versus magnitude (binned by color) in Fig. 16.

Another way to assess PSF performance is to examine the average across visits of $\delta T/T$ projected onto focal-plane coordinates (Figure 14). Piff shows strong spatial correlations, with a systematic offset that matches Table 4. It is the existence of these spatial structures that motivated raising the interpolation order to four, except in the u-band. Although not shown in Figure 14, third-order polynomial interpolation still exhibited residual structure. A fifth-order polynomial interpolation would require more stars than are available on some CCDs to adequately constrain the model while offering only marginal gains. Preliminary analysis of LSSTCam data

in the laboratory at SLAC shows that the ITL sensors exhibit the same pattern. The sensor’s $\delta T/T$ is fully correlated with the height variation across the LSSTCam ITL sensors, which explains this behavior. Future data processing will account for this height variation directly in the PSF model.

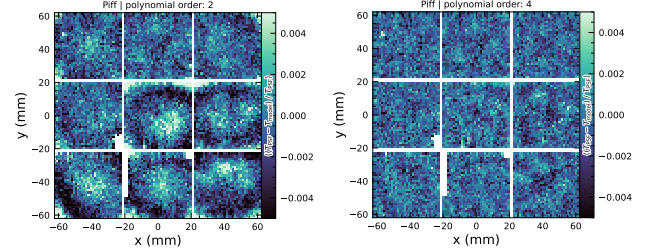


Figure 14. Average across all visits of $\delta T/T$ for different PSF modeling on LSSTComCam. Average is computed on a bin size of 120 pixels.

Another way to look at the PSF modeling quality is via whisker plots of the PSF second and fourth moments and their modeling residuals projected on a part of the sky. In addition to the second moment, the spin-2 fourth moments, $e^{(4)}$, is defined as:

$$\begin{aligned} e_1^{(4)} &= M_{40} - M_{04} \\ e_2^{(4)} &= 2(M_{31} - M_{13}), \end{aligned}$$

where M_{pq} are the standardized higher moments as defined in T. Zhang et al. (2023) measured on stars and PSF models. Figure 15 shows the whisker plots of e , $e^{(4)}$ (top rows), and δe , $\delta e^{(4)}$ in the ECDFS field. The direction of the whiskers represents the orientation of the shape, while the length, modulated by the red bar, represents the amplitude $|e|$ or $|e^{(4)}|$. We observe coherent patterns in both the PSF moments and the residuals, the latter of which warrants further investigation if it persists in future data releases.

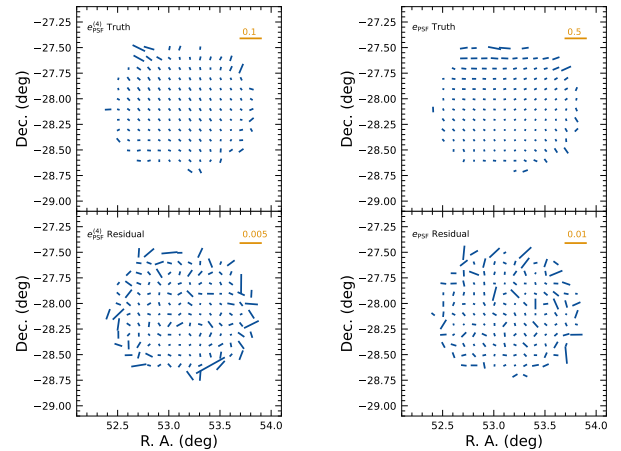
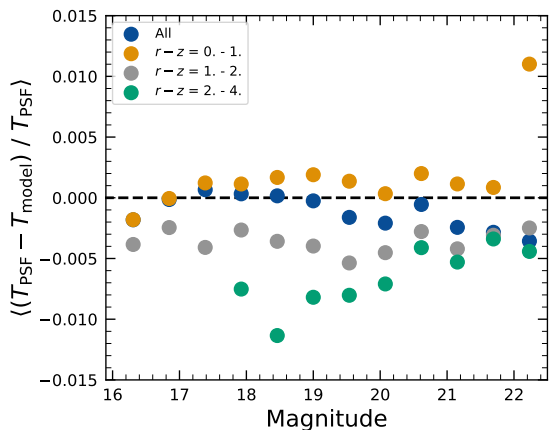


Figure 15. Whisker plot on ECDFS field for e , $e^{(4)}$ and δe , $\delta e^{(4)}$.

Table 4. Comparison of observed and model residuals, across all visits and filters.

Quantity	Observed	Piff O2	Piff O4
	$\times 10^{-3}$	$\times 10^{-4}$	$\times 10^{-4}$
$\langle T \rangle$ (pixel ²)	11.366 ± 0.003		
$\langle e^1 \rangle$	$(-6.07 \pm 0.05) \times 10^{-3}$		
$\langle e^2 \rangle$	$(-4.57 \pm 0.05) \times 10^{-3}$		
$\langle e \rangle$	$(8.794 \pm 0.004) \times 10^{-2}$		
$\langle \delta T/T \rangle$		-4.0 ± 0.2	-5.0 ± 0.2
$\langle \delta e^1 \rangle$		0.6 ± 0.1	0.5 ± 0.1
$\langle \delta e^2 \rangle$		0.0 ± 0.1	0.0 ± 0.1

Another characterization of PSF-modeling performance is to look at $\delta T/T$ versus stellar magnitude to reveal any PSF size-flux dependencies (Figure 16). We also repeat this analysis in color bins to probe chromatic effects. Fainter stars show a larger negative bias in PSF size compared to brighter ones. Binning by color uncovers a clear color dependence, as seen in DES (e.g., M. Jarvis et al. 2021). DP1 does not include the color correction implemented in T. Schutt et al. (2025). Post-DP1 tests added a color correction similar to T. Schutt et al. (2025): it reduced the color-dependent scatter in PSF size but did not eliminate the negative bias for faint sources. The cause of this residual remains unknown and is consistent with what is shown in Table 4.

**Figure 16.** Binned $\delta T/T$ as a function of magnitude across all visits and filters and binned in different colors.

As mentioned in Rubin Observatory Science Pipelines Developers (2025), there are two important Piff features that were not used during DP1. First, PSF color dependence was not yet implemented but will be added in the next release of the Rubin Science Pipelines. Second, although the current Rubin software allows Piff to operate in sky coordinates (including WCS transformations), it does not yet correct for sensor-induced astrometric distortions (e.g., tree

rings). That capability is also planned for future data releases.

5.3. Astrometry

To characterize astrometric performance, we evaluate both internal consistency and agreement with an external reference. A primary measure of internal consistency is the repeatability of position measurements for the same object. We associate isolated point sources across visits and compute the Root-Mean-Square (RMS) of their fitted positions. Figure 17 shows the median per-tract astrometric error for all isolated point sources, both after the initial calibration and after the final calibration, which includes proper motion corrections. The results indicate that the astrometric solution is already very good after the initial calibration. Global calibration yields only modest improvement, likely due to the short time span of DP1 and the minimal distortions in the LSSTComCam. In the main survey, the longer time baseline and greater distortions near the LSSTCam field edges will make global calibration more impactful.

An additional metric of internal consistency is the repeatability of separations between objects at a given distance. To calculate this, we find pairs of objects at a given distance from each other, then calculate their separation in each visit in which they appear. The scatter in these distances then gives us a measure of the internal consistency of the astrometric model. The median value for each tract for objects separated by approximately 5 arcmin after the final calibration, i.e., AM1 from Ž. Ivezić & The LSST Science Collaboration (2018), is given in Figure 17. These values are already approaching the design requirement of 10 mas.

Finally, we consider the median separation between sources not included in the astrometric fit and associated objects from a reference catalog. For this, we use the Gaia DR3 catalog, with the object positions shifted to the observation epoch using the Gaia motion parameters. Figure 18 shows the median separation for each visit in the r-band in tract 4849.

The calculated values are almost all within 5 mas, well below the design requirement of 50 mas for the main survey.

By looking at the astrometric residuals, we can assess whether there are distortions not accounted for by the astrometric model. In some cases, the residuals in a single

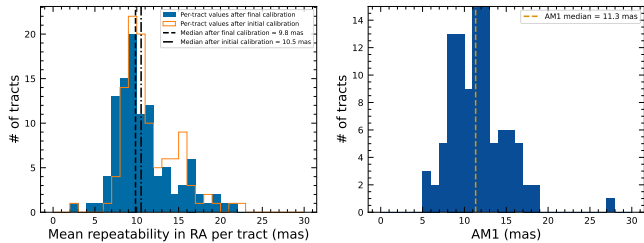


Figure 17. (a) Mean per-tract astrometric repeatability of measurements of isolated point sources in [Rapid Analysis \(RA\)](#) (b) Median per-tract repeatability in separations between isolated point sources 5 arcmin apart.

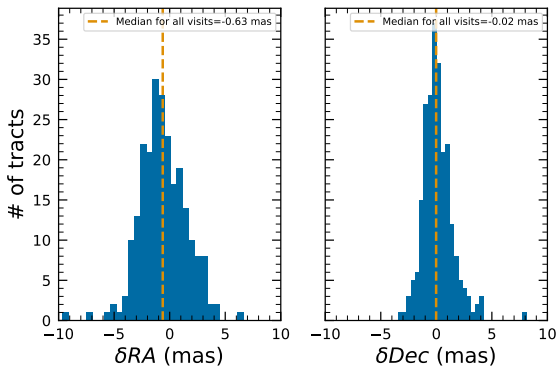


Figure 18. Median absolute offset for all visits in r-band in [tract 4849](#). The offset is the difference between the position of isolated point sources that were reserved from the astrometric fit and matched objects from the Gaia DR3 catalog.

visit show behavior consistent with atmospheric turbulence, as shown in [Figure 19](#). As in [P. F. Léget et al. \(2021\)](#) and [W. F. Fortino et al. \(2021\)](#), this is characterized by a curl-free gradient field in the two-point correlation function of the residuals (E-mode). However, as seen in [Figure 20](#), the residuals in many visits also have correlation functions with a non-negligible divergence free B-mode, indicating that some of the remaining residuals are due to unmodeled instrumental effects, such as rotations between visits.

We can see unmodeled camera distortions by stacking the residuals over many visits as a function of the focal plane position. [Figure 21](#) shows the median residuals in x and y directions for 1792 visits. Spatial structures are evident at the CCD level, along with the mid-line break in the y-direction residuals.

Further stacking all the detectors makes certain effects particularly clear. [Figure 22](#) shows distortions very similar to those measured for an LSSCam ITL sensor in a laboratory setting in [J. H. Esteves et al. \(2023\)](#).

5.4. Detection Completeness on Coadds

We characterize completeness by injecting synthetic sources into coadded images, and by comparing to external catalogs. In both cases, we use a greedy, probabilistic matching algorithm, whereby reference objects are matched

in order of descending brightness to the most likely target within a $0.5''$ radius.

We inject sources in 12 of the patches of the ECDFS region with the deepest coverage. The input catalog contains stars and galaxies from part of the [Data Challenge 2 \(Dark Energy Science Collaboration\)](#) ([LSST Dark Energy Science Collaboration \(LSST DESC\) et al. 2021](#)), where the galaxies consist of an exponential disk and de Vaucouleurs ([G. de Vaucouleurs 1948, 1953](#)) bulge. To avoid deblender failures from excessive increases in object density, stars whose total flux (i.e., summed across all six bands) is brighter than $17.5 \text{ mag}_{\text{AB}}$ are excluded, as are galaxies whose total flux is brighter than $15 \text{ mag}_{\text{AB}}$ or fainter than $26.5 \text{ mag}_{\text{AB}}$. Half of the remaining objects are selected for injection.

[Figure 23](#) shows completeness as a function of magnitude for these injected objects. The completeness estimates are comparable to results from matching external catalogs. The Hubble Legacy Field catalog ([K. E. Whitaker et al. 2019](#); [G. Illingworth et al. 2016](#)) reaches 50% completeness at $26.13 \text{ mag}_{\text{F775W}}$, approximately 0.4 magnitudes fainter; this is roughly equivalent to 25.83 mag_i from differences in matched object magnitudes. Similarly, completeness drops below 90% at $23.80 \text{ mag}_{\text{VIS}}$ matching to Euclid Q1 ([Euclid Collaboration et al. 2025](#)) objects, equivalent to about 23.5 mag_i . The Euclid imaging is of comparable (or shallower) depth, so magnitude limits at lower completeness percentages than 90% are unreliable, whereas the HST images cover too small (and irregular) of an area to accurately characterize 80-90% completeness limits.

At the 80% completeness limit, nearly 20% of objects, primarily injected galaxies, are incorrectly classified as stars based on the refExtendedness parameter, which indicates whether a source is more likely to be a point source or an extended source. Similarly, the fraction of correctly classified injected stars drops to about 50% at 23.8 mag_i (90% completeness).

There are several caveats for this analysis. The selection of objects for matching in any catalog is not trivial. Some fraction of the detections are either artifacts (particularly close to diffraction spikes around bright stars) or otherwise spurious. Additionally, some objects lie in masked regions of one survey but not another, which has not been accounted for. For injected source matching, the reference catalog does not include real on-sky objects. For this reason, we do not quote specific figures for purity; however, based on prior analyses of the DC2 simulations, purity is generally higher than completeness at any given magnitude.

5.5. Flux Measurement

[Figure 24](#) shows *i*-band magnitude residuals for CModel and Sersic measurements using the matched injected galaxies described in [5.4](#). Similar behavior is seen in other bands. Sersic fluxes show reduced scatter and are more accurate on average for galaxies brighter than 22.5 mag_i , though CModel's are less biased, median residuals are slightly closer to zero. For fainter objects, Sersic fluxes are more biased and less accurate. The magnitude of this bias is considerably larger than previously seen in simulated data and is being investi-

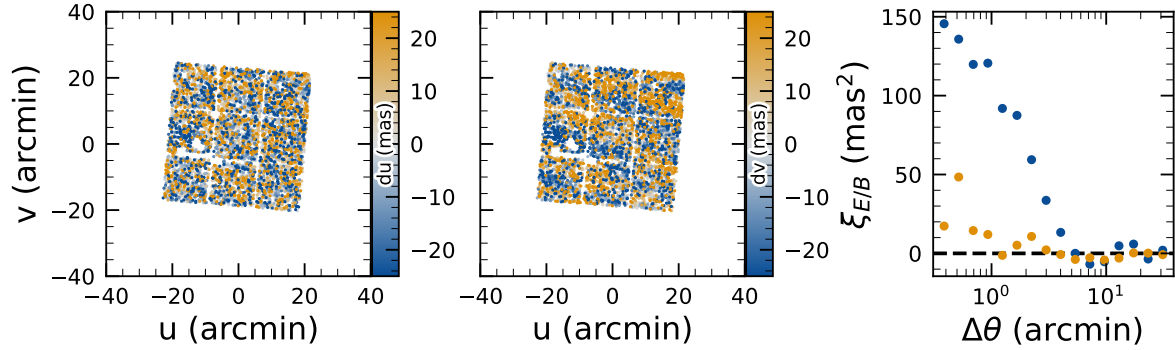


Figure 19. Residuals in du (left panel) and dv (center panel) directions, with the E and Byte (8 bit) (B)-modes of the two-point correlation function (right panel). The residuals show a wave-like pattern characteristic of atmospheric turbulence, and there is significant E-mode and negligible B-mode in the correlation function.

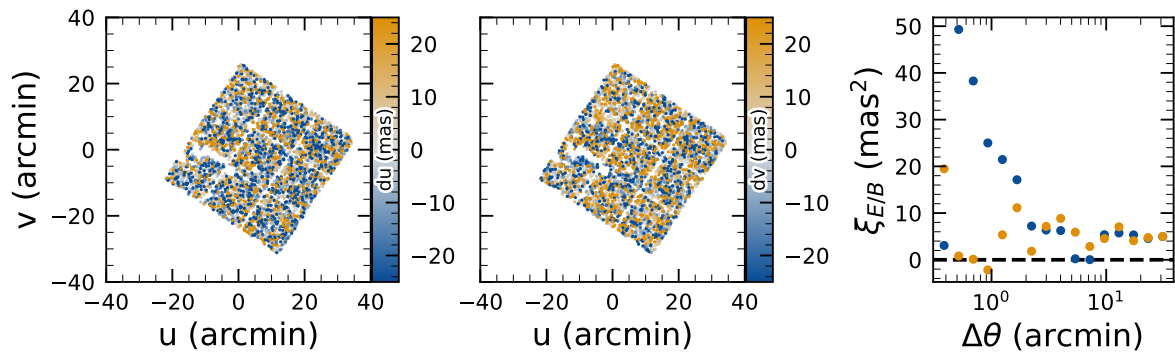


Figure 20. Residuals in du (left panel) and dv (center panel) directions, with the E and B-modes of the two-point correlation function (right panel). There are coherent residuals, but without the wave-like pattern seen in Figure 19, and the correlation function has significant values for both E and B-modes.

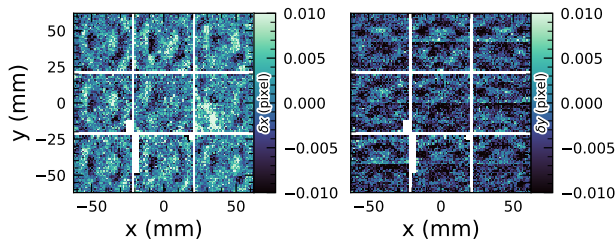


Figure 21. Median residuals as a function of focal plane position in dx (left panel) and dy (right panel) directions

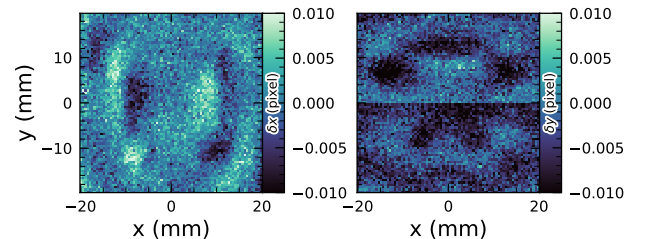


Figure 22. Median residuals as a function of pixel position in dx (left panel) and dy (right panel) directions

1714 gated. Aperture fluxes - including Kron and Gaussian Aperture and PSF - are not shown as they are not corrected to
 1715 yield total fluxes and thus are not recommended for use as
 1716 total galaxy magnitudes.

1717
 1718 Figure 24 shows $g - i$ color residuals versus r -band magnitude for the same sample of galaxies as Figure 24. For this
 1719 and most other colors, GAaP (with a $1''$ aperture) and Sersic colors both yield lower scatter; however, the CModel colors
 1720 have the smallest bias. Curiously, the GAaP bias appears
 1721
 1722

1723 to be magnitude-dependent, whereas the Sersic bias remains
 1724 stable from $19 < r < 26$. Any of these color measurements
 1725 are suitable for use for deriving quantities like photometric
 1726 redshifts, stellar masses, etc.

1727 In addition to photometry, some algorithms include mea-
 1728 surements of structural parameters like size, ellipticity, and
 1729 Sersic index. One particular known issue is that many (truly)
 1730 faint objects have significantly overestimated sizes and fluxes,
 1731 as was also seen in the Dark Energy Survey (K. Bechtol et al.

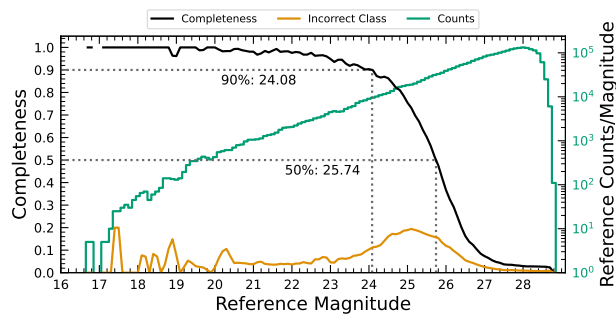


Figure 23. Completeness as a function of i -band CModel magnitude for DC2-based injections into a portion of the ECDFS field.

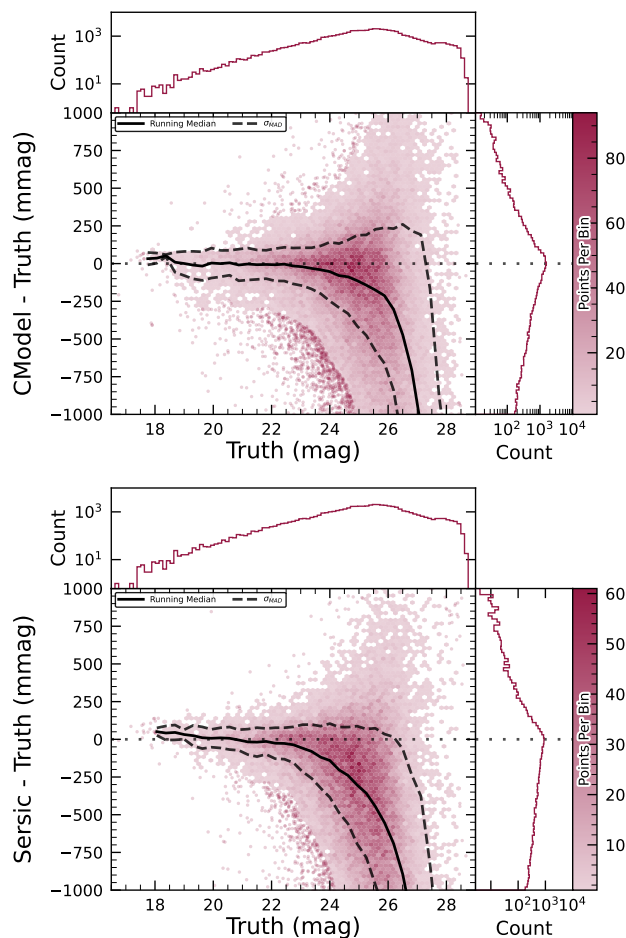


Figure 24. Magnitude residuals for matched injected galaxies with the CModel and Sersic algorithms.

1732 2025) and dubbed "super-spreaders". These super-spreaders
 1733 contribute significantly to overestimated fluxes at the faint end,
 1734 and are particularly problematic for the Kron algorithm
 1735 (R. G. Kron 1980), which is not recommended for general
 1736 use.

1737 As mentioned in §4.5, the Sersic fits include a free centroid,
 1738 which is initialized from the fiducial centroid of the

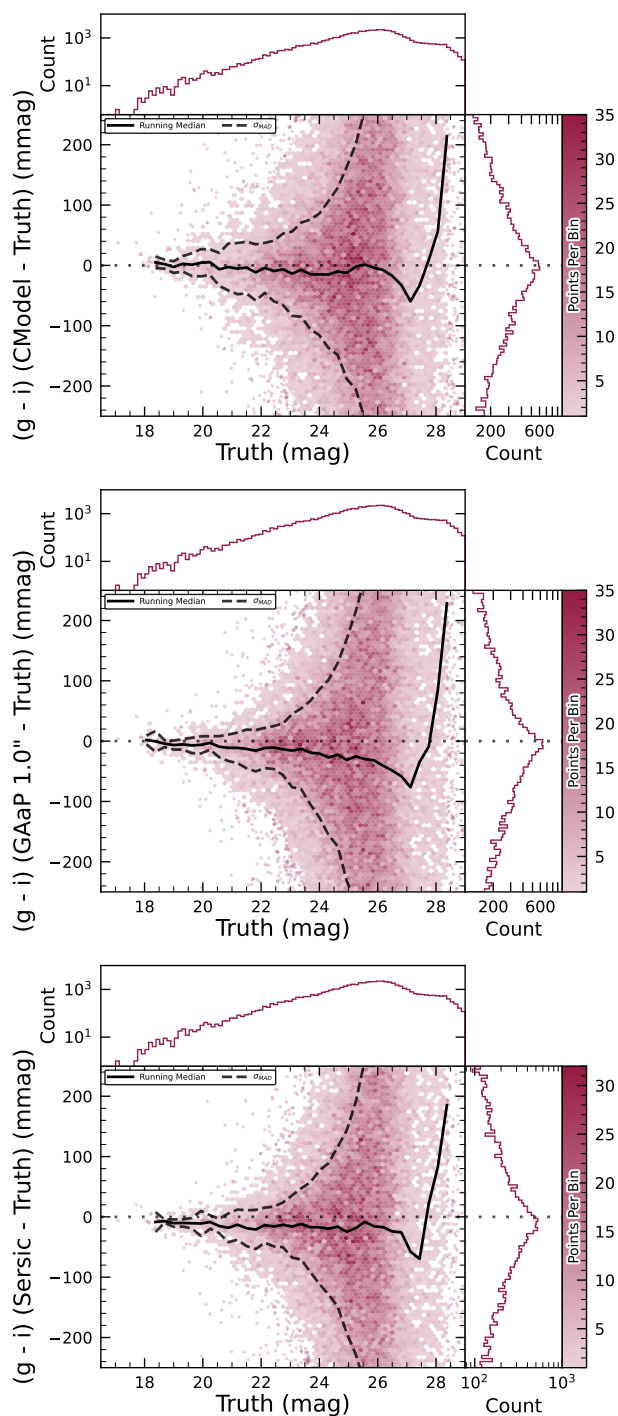


Figure 25. $g - i$ color residuals versus injected r -band magnitude for matched galaxies with the CModel, GAaP and Sersic algorithms.

1739 object. Preliminary analyses of matched injected objects
 1740 suggest that the galaxy astrometry residuals are somewhat
 1741 smaller, and so users of the Sersic photometry should also
 1742 use these centroid values (if needed). One caveat is that
 1743 for faint objects and/or in crowded regions with unreliable

1744 deblending, free centroids can drift significantly and potentially
 1745 towards other objects, so objects with large differences
 1746 between the fiducial and Sersic [astrometry](#) should be used
 1747 with caution.

1748 5.6. Differential Chromatic Refraction

1749 [Differential Chromatic Refraction](#) (DCR) occurs when
 1750 light passes through Earth’s atmosphere, refracting more
 1751 for shorter wavelengths, which causes blue light to appear
 1752 shifted closer to the zenith. This wavelength-dependent ef-
 1753 fect results in the smearing of point sources along the zenith
 1754 direction, specifically parallel to the parallactic angle. The
 1755 DCR effect is observable in LSSTComCam data, particularly in
 1756 the angular offset versus $g-i$ band magnitude difference
 1757 plots [Figure 26](#) which contains all direct sources with SNR
 1758 > 10 from 41 visits from November 26, 2024. When look-
 1759 ing at data perpendicular to the parallactic angle, sources
 1760 show no DCR effect (as expected), forming a clear vertical
 1761 distribution on the hexbin plots.

1762 In contrast, sources aligned with the parallactic angle ex-
 1763 hibit a tilted, linear distribution, clearly demonstrating the
 1764 relationship between angular offset and the $g-i$ band mag-
 1765 nitude difference, thereby providing a visual indication of the
 1766 [DCR](#) effect.

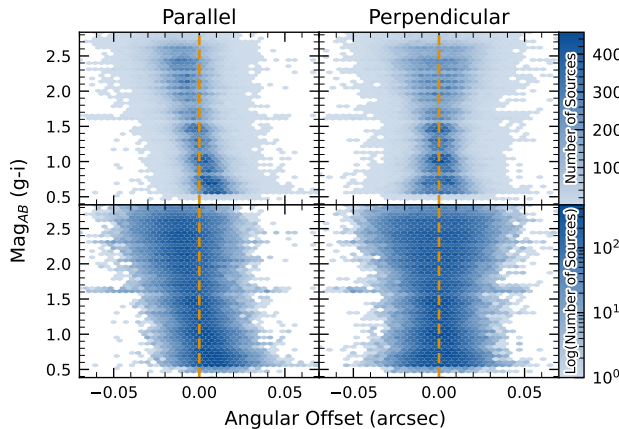


Figure 26. Visualization of [Differential Chromatic Refraction](#) (DCR) observed in the LSSTComCam commissioning campaign. The $g-i$ color is computed for every source in the reference catalog that is matched to a direct source in the science image, and the binned density for the full survey is plotted against the angular offset between the reference and detected positions. The angular offset is projected along coordinates parallel and perpendicular to the parallactic angle of the observation, and shows a characteristic correlation along the parallel axis with no correlation along the perpendicular axis. The orange vertical dashed line indicates the expected $g-i$ magnitude distribution at zero angular offset, while the green ‘x’ marks the average $g-i$ magnitude of the plotted sources.

1767 5.7. Difference Imaging Purity

1768 We assessed the performance of image differencing using
 1769 human vetting and source injection (§5.8.3). Members of the
 1770 DP1 team labeled more than 9500 DIASource image triplets
 1771 consisting of cutouts from the science, template, and differ-
 1772 ence images. We classified these into various real and artifact
 1773 categories. The raw real:bogus ratio was roughly 9:1. Bright
 1774 stars are the main source of artifacts. Correlated noise, pri-
 1775 marily in u and g bands, also leads to spurious detections
 1776 near the threshold. We expect to be able to mitigate these
 1777 effects for LSSTCam.

1778 Applying a reliability threshold improves the purity of
 1779 transients but not variable stars; technical limitations at the
 1780 time of model training prevented injection of variable stars
 1781 into the synthetic training set. Reliability models for LSST-
 1782 Cam data will be trained on a wider range of input data.

1783 5.8. Solar System

1784 5.8.1. Asteroid Linking Performance

1785 DP1 performance evaluation of asteroid linking focused on
 1786 demonstrating discovery capability. The solar system discov-
 1787 ery [pipeline](#) produced 269,581 tracklets, 5,691 linkages, and
 1788 281 post-processed candidates.

1789 We performed a conservative manual investigation of these
 1790 281 candidates, producing a curated list of 93 probable new
 1791 asteroid discoveries. As described in Section 4.6.3, post
 1792 processing of the [heliolinc](#) output with [link_purify](#) produced
 1793 a final set of 281 candidate linkages, ranked with the most
 1794 promising candidates first. Using [find_orb](#) (B. Gray 2025),
 1795 we derived orbit fits for each candidate, sorting the result-
 1796 ing list by χ^2_{dof} , the quality of the fit. Manual inspection of the
 1797 linkages indicated that those ranked 0–137 corresponded to
 1798 unique real asteroids; ranks 138–200 contained additional
 1799 real objects intermixed with some spurious linkages; and
 1800 ranks higher than 200 were essentially all spurious. This
 1801 analysis indicates that it will be possible to identify cuts
 1802 on quality metrics like χ^2 to derive discovery candidate sam-
 1803 ples with high purity; determining the exact quantitative cut
 1804 values require more data with LSSTCam. We next removed
 1805 all observations matched to known asteroids (using [Minor](#)
 1806 [Planet Center](#) ()’s MPChecker service), reducing the number
 1807 of candidates to 97. Of these, four had strong astrometric
 1808 and/or photometric outliers, likely due to self-subtraction
 1809 in difference images due to the unavoidable limitations of
 1810 template generation from the limited quantity of data avail-
 1811 able from LSSTComCam. We suspect these four linkages
 1812 do correspond to real objects, but have chosen to discard
 1813 them out of an abundance of caution. The remaining 93
 1814 were submitted to the Minor Planet Center and accepted as
 1815 new discoveries, demonstrating the LSST pipelines are able
 1816 to successfully discover new solar system objects.

1817 5.8.2. Asteroid Association Performance

1818 Solar system association associated 5988 DiaSources to 431
 1819 unique solar system objects. These include 3,934 DiaSources
 1820 to 338 already-known MPC objects and 2,054 DiaSources to
 1821 the 93 discoveries newly-discovered objects. Association also
 1822 picked up an additional 143 detections of newly discovered

1823 objects. These were not originally found by the discovery
 1824 pipelines as they didn't satisfy the number and/or maximum
 1825 time span requirements to form tracklets.

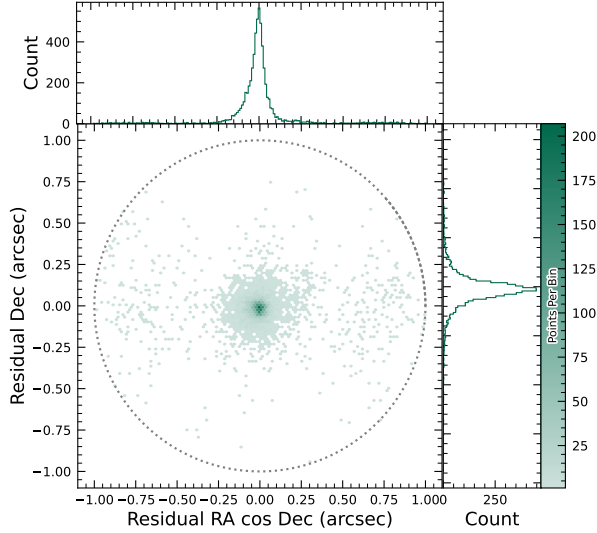


Figure 27. Astrometric residuals between expected and observed positions of SSOs in DP1. The median residuals are $0.''001$ and $-0.''016$ in R.A./Dec direction, with the standard deviations of $0.''19$ and $0.''10$, respectively. No detectable systematic offset from zero indicates there are no major errors in either timing or astrometry delivered by the Rubin system. The wider scatter in the RA-direction is due to objects whose measured orbital elements are less well constrained, translating to larger along-track positional errors in the predicted positions.

1826 The astrometric residuals of known asteroid association are
 1827 shown in Figure 27. Astrometric precision for solar system
 1828 sources is excellent, the majority of objects detected within
 1829 $0''.1$ of their expected positions. Taking the unsigned median
 1830 residuals to search for biases, we find that previously-known
 1831 objects have mean residuals of $0.''001$ and $-0.''016$ in the
 1832 RA and Dec directions respectively, while newly-discovered
 1833 objects have mean residuals of $-0.''035$ and $-0.''010$ in the
 1834 RA and Dec directions, respectively. These mean residuals
 1835 are small enough to eliminate the possibility of a timing off-
 1836 set greater than the second-scale shutter motion (which is
 1837 uncharacterized for LSSTComCam).

1838 5.8.3. Detection Completeness on Difference Images

1839 We assess the performance of our difference imaging
 1840 pipeline using synthetic source injection on the science images
 1841 prior to differencing. We construct a catalog of injected
 1842 sources by joining two different samples of point sources, a
 1843 set of hosted sources to emulate transients in galaxies and
 1844 second set of hostless.

1845 The hosts are selected from the pipeline source catalog that
 1846 is produced upstream by imposing a cut in their extended-

1847 ness measurement, and selecting $N_{\text{src}} = \min(100, N \times 0.05)$
 1848 of the available sources per detector. For each host we pick
 1849 a random position angle and radius using its light profile
 1850 shape, and also a random value of brightness for the injected
 1851 source, with magnitudes higher than the host source. The
 1852 hostless sources instead have random positions in the CCD
 1853 focal plane, and with magnitudes chosen from a random uni-
 1854 form distribution with $20 \geq m \geq m_{\text{lim}} + 1$ with m_{lim} the
 1855 limiting magnitude of the image.

1856 We used the LSST package `source_injection` to include
 1857 these sources into our test images, we performed a coordinate
 1858 cross-match task, with a threshold of $0.''5$ to find which of
 1859 these sources were detected and which were lost, enabling
 1860 the calculation of a set of performance metrics.

1861 In Figure 28 we show the detection completeness as function
 1862 of the SNR, for sources in the ECDFS field, for filters
 1863 *griz*. We observe a completeness $> 95\%$ for sources with
 1864 $\text{SNR} > 6$, with mean completeness $\simeq 99\%$ and standard
 1865 deviation of $\simeq 0.7\%$. In Figure 29 we show the distribution of

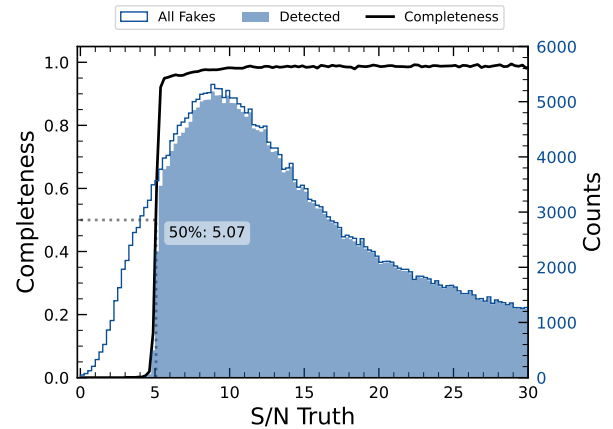


Figure 28. The difference image detection completeness for injected sources in the ECDFS field, for filters *griz*, as function of the estimated signal to noise ratio S/N. This completeness is the ratio between the found fake sources (shaded histogram) and all the sources (solid line). The horizontal dashed line represents where the 50% completeness level is reached, at approximately $S/N \simeq 5.07$.

1866 the residuals of the recovered sky coordinates for the detected
 1867 synthetic sources. The marginal distributions are both centered
 1868 at zero, and they are compatible with normal distributions
 1869 $\mathcal{N}(0, 0.''04)$. In Figure 30 we show the recovered
 1870 magnitudes for our detected synthetic sources in the *i* filter,
 1871 using PSF photometry on the difference images, and also
 1872 show marginal distributions of the true magnitudes for fake
 1873 sources, and the residuals on the left, split into hosted and
 1874 hostless. Our flux measurements are accurate within a wide
 1875 range of magnitudes, for both hosted and hostless synthetic
 1876 sources. We obtain that for true $m_i < 22.2$, the median PSF
 1877 magnitudes residuals are < 0.1 . When considering the flux
 1878 pulls $\delta = (f - f_{\text{True}})/\sigma_f$ for PSF flux f and error σ_f , we find
 1879 that $|\langle \delta \rangle| < 0.1$, and $\sigma_\delta < 1.1$ for $m_i < 21.6$.
 1880
 1881
 1882

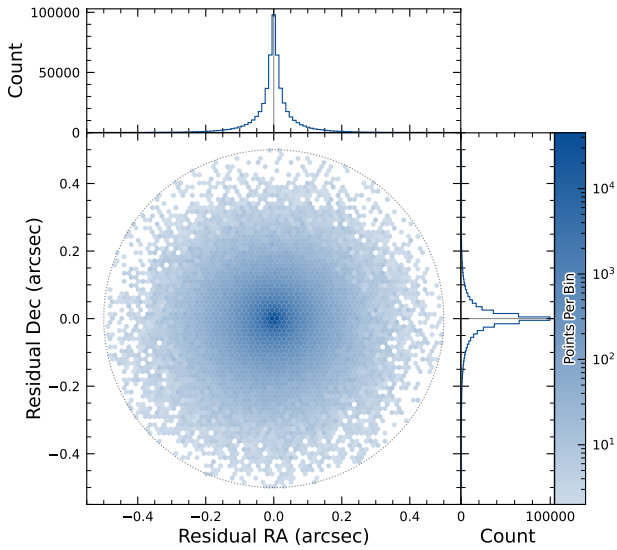


Figure 29. Coordinate residuals for detected synthetic sources in difference images, between recovered and true position of the sources in the ECDFS field. In the top and right panels we include the histogram of these offsets. The circle reflects the matching radius of $0''.5$.

5.9. Crowded Fields

Two of the seven DP1 target fields exhibit high stellar density, 47 Tucanae and the Fornax dwarf galaxy. 47 Tucanae was chosen as an initial stress test for the science pipelines processing. The Fornax dwarf galaxy also exhibits high stellar density, particularly in its central regions.

6. RUBIN SCIENCE PLATFORM

The RSP (M. Jurić et al. 2019; F. Economou 2023) is a powerful, cloud-based environment for scientific research and analysis of petascale-scale astronomical survey data. It serves as the primary interface for scientists to access, visualize, and conduct next-to-the-data analysis of Rubin and LSST data. The RSP is designed around a “bring the compute to the data” principle, eliminating the need for users to download massive datasets. Although DP1 is comparable in size (3.5 TB) to existing survey datasets, future LSST datasets will be larger and more complex, making it crucial to co-locate data and analysis for effective scientific discovery.

The RSP provides users with access to data and services through three distinct user-facing Aspects: a Portal, which facilitates interactive exploration of the data; a JupyterLab-based Notebook environment for data analysis using Python; and an extensive set of Application Programming Interfaces (APIs) that enable programmatic access to both data and services. The three Aspects are designed to be fully integrated, enabling seamless workflows across the RSP. The data products described in §3 are accessible via all three Aspects, and the system facilitates operations such as starting

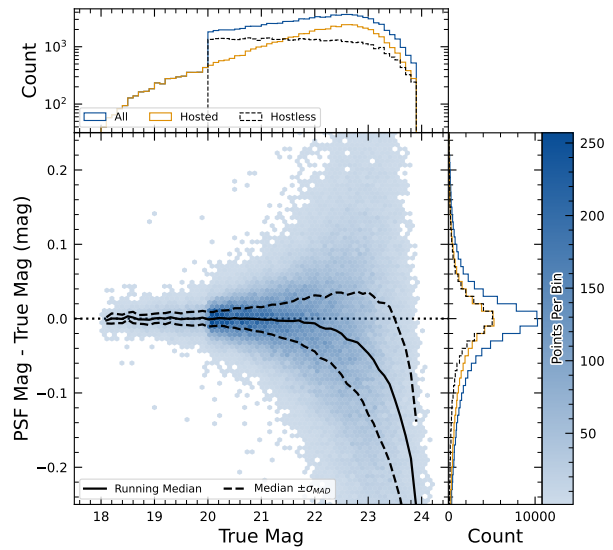


Figure 30. Magnitude residuals for PSF photometry on difference images for ECDFS field in i for detected fake sources. In black solid and dashed lines: the running median, and the mean absolute deviation. Top panel: the distribution of true magnitudes for hostless and hosted fakes sources. Right panel: the distribution of magnitude residuals for hostless and hosted sources.

a query in one Aspect and retrieving its results in another. Figure 31 shows the Rubin Science Platform landing page in the Google cloud.

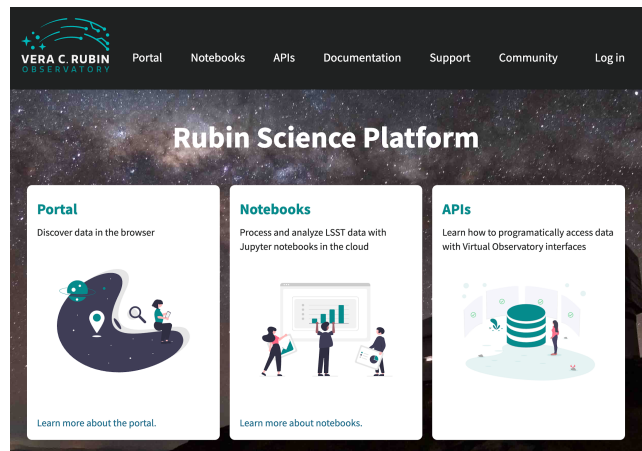


Figure 31. The Rubin Science Platform landing page showing the three Aspects as well as links to documentation and support information.

The RSP is supported by a number of back-end services, including databases, files, and batch computing. Support for collaborative work through shared workspaces is also included in the RSP.

A preview of the *RSP* was launched on Google Cloud in 2022, operating under a shared-risk model to support *Data Preview 0* (W. O’Mullane et al. 2024a). This allowed the community to test the platform, begin preparations for science, and provide valuable feedback to inform ongoing development. It was the first time an astronomical research environment was hosted in a *cloud* environment. The DP1 release brings major updates to *RSP* services, enhancing scientific analysis capabilities. The *RSP* remains under active development, with incremental improvements being rolled out as they mature. During the Rubin Early Science Phase, the *RSP* will continue to operate under a shared-risk model. This section outlines the *RSP* functionality available at the time of the DP1 release and provides an overview of planned future capabilities.

6.1. Rubin Data Access Center

The Rubin USDAC utilizes a novel hybrid on-premises-*cloud* architecture, which combines on-premises infrastructure at the USDF at SLAC with flexible and scalable resources in the Google *cloud*. This architecture has been deployed and tested using the larger simulated data set of DP0.2 (W. O’Mullane et al. 2024b).

In this hybrid model, user-facing services are deployed in the *cloud* to support dynamic scaling in response to user demand and to simplify the provisioning and management of large numbers of science user accounts. The majority of the static data products described in §3 are stored on-premises at the USDF to benefit from cost-effective mass storage and close integration with Rubin data processing infrastructure, also located at the USDF. For imaging data, the Data Butler (§6.2.2) provides the interface between the *cloud*-based users and data services, and the on-premises data. For catalog data, a *cloud*-based TAP client (§6.2.1) submits queries to the on-premises Qserv database cluster (§6.5) and retrieves the results. In the initial DP1 deployment, catalog data is hosted at the USDF while image data is stored in the *cloud*. The full hybrid model will be rolled out and further tested following the release of DP1.

The *RSP* features a single-sign-on authentication and authorization system to provide secure access for Rubin data rights holders (R. Blum & the Rubin Operations Team 2020)

6.2. API Aspect

The *API* Aspect provides a comprehensive set of user-facing interfaces for programmatic access to the DP1 data products, through both IVOA-compliant services and the Rubin Data Butler. IVOA services enable standard queries and integration with existing tools, while the Butler facilitates advanced data processing within the LSST Science Pipelines.

At the time of the DP1 release, some IVOA services are unavailable, and certain data products are only accessible via the Butler. This section provides an overview of the available IVOA services and Butler access.

6.2.1. IVOA Services

Rubin has adopted a Virtual Observatory (VO)-first design philosophy, prioritizing compliance with IVOA standard

interfaces to foster interoperability, standardization, and collaboration. In cases where standardized protocols have yet to be established, additional services have been introduced to complement these efforts. This approach ensures that the *RSP* can be seamlessly integrated with community-standard tools such as TOPCAT (M. Taylor 2011) and Aladin (F. Bonnarel et al. 2000; T. Boch & P. Fernique 2014; M. Baumann et al. 2022), as well as libraries such as PyVO (M. Graham et al. 2014).

The user-facing APIs are also used internally within the *RSP*, creating a unified design that ensures consistent and reproducible workflows across all three Aspects. This reduces code duplication, simplifies maintenance, and ensures all users, both internal and external, access data in the same way. For example, an Astronomical Data Query Language (IVOA standard) (IVOA) query on the Object catalog via TAP yields identical results whether run from the Portal, Notebook, or an external client.

The following IVOA services are available at the time of the DP1 release:

- **Table Access Protocol (TAP) Service:** A TAP service (P. Dowler et al. 2019) enables queries of catalog data via the IVOA-standard ADQL, a dialect of SQL92 with spherical geometry extensions. The main TAP service for DP1 runs on the Rubin-developed Qserv database (§ 6.5), which hosts the core science tables described in §3.2, as well as the Visit database. It also provides image metadata in the IVOA ObsCore format via the standard `ivoa.ObsCore` table, making it an “ObsTAP” service (ObsTAP; M. Louys et al. 2017). The TAP service is based on the Canadian Astronomy Data Centre (CADC)’s open-source Java TAP implementation¹⁹, modified for the exact query language accepted by Qserv. It currently supports a large subset of ADQL, with limitations documented in the data release materials (see §7.1) and exposed via the TAP **capabilities** endpoint where possible.

The TAP service provides metadata annotations consistent with the standard, including table and column descriptions, indications of foreign-key relationships between tables, and column metadata such as units and IVOA Unified Content Descriptors (UCDs).

- **Image Access Services:** Rubin image access services are compliant with IVOA SIAv2 (Simple Image Access Protocol, version 2; T. Jenness et al. 2024; P. Dowler et al. 2015) for discovering and accessing astronomical images based on *metadata*. For example, querying for all images in a given band over a particular sky region observed during a given period. SIAv2 is a REpresentational State Transfer (REST)-based protocol that supports the discovery and retrieval of image data. Users identify an image or observation of interest and query the service. The result set includes *metadata* about the image, such as the sky position, time, or band, and a data access URL, which includes

¹⁹ <https://github.com/opencadc/tap>

an IVOA Identifier uniquely identifying the dataset (T. Jenness & G. P. Dubois-Felsmann 2025), allowing the dataset to be retrieved or a cutout requested via [Server-side Operations for Data Access \(IVOA standard\)](#) ().

- **Image Cutout Service:** The Rubin Cutout Service (R. Allbery 2023, 2024) is based on the IVOA SODA (Server-side Operations for Data Access; F. Bonnarel et al. 2017). Users submit requests specifying sky coordinates and the cutout size as the radius from the coordinates, and the service performs the operation on the full image and returns a result set. For DP1, The cutout service is a single cutout service only where N cutout requests will require N independent synchronous calls. We expect some form of bulk cutout service by mid 2026, approximately contemporaneously with DP2
- **HiPS Data Service:** An authenticated HiPS (P. Fernique et al. 2017) data service for seamless pan-and-zoom access to large-scale co-adds. It supports fast interactive progressive image exploration at a range of resolutions.
- **WebDAV:** A [Web Distributed Authoring and Versioning \(WebDav\)](#) service is provided to enable users to remotely manage, edit, and organize files and directories on the RSP as if they were local files on their own computer. This is especially useful for local development.

6.2.2. Data Butler

The Rubin Data Butler (T. Jenness et al. 2022; N. B. Lust et al. 2023), is a high-level interface designed to facilitate seamless access to data for both users and software systems. This includes managing storage formats, physical locations, data staging, and database mappings. A Butler repository contains two components:

- the *Data Store*: A physical storage system for datasets, e.g., a [Portable Operating System Interface \(POSIX\)](#) file system or S3 object store; and
- the *Registry*: An [Structured Query Language \(SQL\)](#)-compatible database that stores metadata about the datasets in the data store, see §??.

For DP1, the Butler repository is hosted in the Google Cloud, using an [\(Amazon\) Simple Storage Service \(S3\)](#)-compatible store for datasets and AlloyDB, a PostgreSQL-compatible database, for the registry.

In the context of the Butler, a *dataset* refers to a unique data product, such as an image, catalog or map, generated by the observatory or processing pipelines. Datasets belong to one of the various types of data products, described in §3. The Butler ensures that each dataset is uniquely identifiable by a combination of three pieces of information: a data coordinate, a dataset type, and a run collection. For example, a dataset that represents a single raw image with detector 8 during the on-sky campaign on the night starting 2024-11-11 in the *i* band

with exposure ID 2024111100074 would be represented as `dataId='exposure':2024111100074, 'band':'i', 'instrument':'LSSTComCam'` and is associated with the `raw` DatasetType. For a deep coadd on a patch of sky in the Seagull field, there would be no exposure dimensions and would instead the tract, patch and band would be specified as `dataId='tract':7850, 'patch': 6, 'band':'g', 'instrument':'LSSTComCam', skymap='lsst_cells_v1'` and is associated with the `deep_coadd` DatasetType.

The data coordinate is used to locate a dataset in multi-dimensional space, where dimensions are defined in terms of scientifically meaningful concepts, such as instrument, visit, detector or band. For example, a calibrated single-visit image (§3.1) has dimensions including band, instrument, and detector. In contrast, the visit table (§3.2), a catalog of all calibrated single-epoch visits in DP1, has only the instrument dimension. The main dimensions used in DP1 are listed, together with a brief description, in Table 5. To determine which dimensions are relevant for a specific dataset, the Butler defines dataset types, which associate each dataset with its specific set of relevant dimensions, as well as the associated Python type representing the dataset. The dataset type defines the kind of data a dataset represents. For example, a raw image (`raw`), a processed catalog (`object_forced_source`), or a `sky map` (`skyMap`).

Table 6 lists all the dataset types available via the Butler in DP1, together with the dimensions needed to uniquely identify a specific dataset and the number of unique datasets of each type. It is important to highlight a key difference between accessing catalog data via the TAP service versus the Butler. While the TAP service contains entire catalogs, many of the same catalogs in the Butler are split into multiple separate catalogs. This is partly due to how these catalogs are generated, but also because of the way data is stored within and retrieved from the Butler repository – it is inefficient to retrieve the entire `Source` catalog, for example, from the file system. Instead, because the `Source` catalog contains data for sources detected in the `visit_images`, there is one `Source` catalog in the Butler for each `visit_image`. Similarly, there is one `Object` catalog for each `deep_coadd`. All the catalogs described in §3.2, aside from the `CcdVisit`, `SSObject`, `SSSource`, and `Calibration` catalogs, are split within the Butler.

A dataset is associated with one or more *Run Collections*; logical groupings of datasets within the Butler system that were created or processed together by the same batch operation. Collections allow multiple datasets with the same data coordinate to coexist without conflict. Run Collections support flexible, parallel processing by enabling repeated analyses of the same input data using different configurations.

For DP1, a subset of the consolidated database contents (§6.5.2) is accessible through the Data Butler. However, not all metadata from the `Visit` table (§3.4) is available. The DP1 Butler is read-only; a writeable Butler is expected by mid-2026, around the time of DP2.

6.2.3. Remote Programmatic Access

The Rubin RSP API can be accessed from a local system by data rights holders outside of the RSP, by creating a user

Table 5. Descriptions of and valid values for the key data dimensions in DP1. YYYYMMDD signifies date and # signifies a single 0-9 digit.

Dimension	Format/Valid values	Description
day_obs	YYYYMMDD	A day and night of observations that rolls over during daylight hours.
visit	YYYYMMDD#####	A sequence of observations processed together; synonymous with “exposure” in DP1.
exposure	YYYYMMDD#####	A single exposure of all nine ComCam detectors.
instrument	LSSTComCam	The instrument name.
detector	0 - 8	A ComCam detector.
skymap	lsst_cells_v1	A set of tracts and patches that subdivide the sky into rectangular regions with simple projections and intentional overlaps.
tract	See Table 2	A large rectangular region of the sky.
patch	0 - 99	A rectangular region within a tract.
physical_filter	u_02, g_01, i_06, r_03, z_03, y_04	An astronomical filter.
band	u, g, r, i, z, y	An astronomical wave band.

Table 6. The name and number of each type of data product in the Butler and the dimensions required to identify a specific dataset.

Data Product	Name in Butler	Required Dimensions	Number in DP1
raw	raw	instrument, detector, exposure	16125
visit_image	visit_image	instrument, detector, visit	15972
deep_coadd	deep_coadd	band, skymap, tract, patch	2644
template_coadd	template_coadd	band, skymap, tract, patch	2730
difference_image	difference_image	instrument, detector, visit	15972
Source	source	instrument, visit	1786
Object	object	skymap, tract	29
ForcedSource	object_forced_source	skymap, tract, patch	636
DiaSource	dia_source	skymap, tract	25
DiaObject	dia_object	skymap, tract	25
ForcedSourceOnDiaObject	dia_object_forced_source	skymap, tract, patch	597
CCDVisit	visit_detector_table	instrument	1
SSObject	ss_object	–	1
SSSource	ss_source	–	1
Visit	visit_table	instrument	1
x			

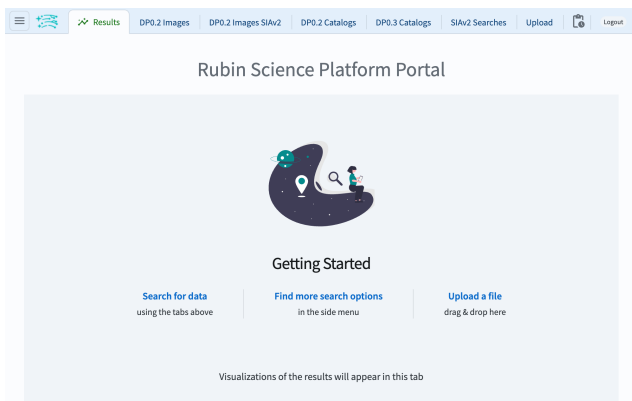
2146 security token. This token can then be used as a bearer token for API calls to the RSP TAP service. This capability is especially useful for remote data analysis using tools such as Tool for OPERations on Catalogues And Tables (TOPCAT), as well as enabling third-party systems (e.g., Community Alert Brokers) to access Rubin data. Additionally, it supports remote development with local IDEs, allowing for more flexible workflows and integration with external systems.

2154 6.3. Portal Aspect

2155 The Portal Aspect provides an interactive environment for exploratory data discovery, query, filtering, and visualization of both image and catalog data, without requiring programming experience.

2159 It enables users to search, visualize, and interact with large datasets through tools for catalog queries, image browsing, time series inspection, and cross-matching. The Portal is designed to support both exploratory data access and detailed scientific investigation.

2164 The Portal is built on Firefly (X. Wu et al. 2019), a powerful web application framework developed by IPAC (Infrared Processing and Analysis Center). Firefly provides interactive capabilities such as customizable table views, image overlays, multi-panel visualizations, and linked displays between catalogs and images. Through Firefly, the Portal delivers a responsive and intuitive user experience, allowing users to analyze data visually while maintaining access to underlying metadata and query controls.



2173 **Figure 32.** The Rubin Science Platform Portal Aspect

2174 6.4. Notebook Aspect

2176 The Notebook Aspect provides an interactive, web-based environment built on Jupyter Notebooks, enabling users to write and execute Python code directly on Rubin and LSST data without downloading it locally. It offers programmatic access to Rubin and LSST data products, allowing users to query and retrieve datasets, manipulate and display images, compute derived properties, plot results, and reprocess data using the LSST Science Pipelines (§4.1). The environment comes pre-installed with the pipelines and a broad set of widely used astronomical software tools, supporting immediate and flexible data analysis.

2187 6.5. Databases

2188 The user-facing Aspects of the RSP are supported by several backend databases that store catalog data products, image metadata, and other derived datasets. The schema for DP1 and other Rubin databases is available online at <https://sdm-schemas.lsst.io>.

2193 6.5.1. Qserv

2194 The final 10-year LSST catalog is expected to reach 15 PB and contain measurements for billions of stars and galaxies across trillions of detections. To support efficient storage, querying, and analysis of this dataset, Rubin Observatory developed Qserv (D. L. Wang et al. 2011; F. Mueller et al. 2023) – a scalable, parallel, distributed SQL database system. Qserv partitions data over approximately equal-area regions of the celestial sphere, replicates data to ensure resilience and high availability, and uses shared scanning to reduce overall I/O load. It also supports a package of scientific user-defined functions (SciSQL: <https://smonkewitz.github.io/scisql/>) simplifying complex queries involving spherical geometry, statistics, and photometry. Qserv is built on robust production-quality components, including MariaDB (<https://www.mariadb.org/>) and XRootD (<https://xrootd.org/>). Qserv runs at the USDF and user access to catalog data is via the TAP service (§6.2.1). This enables catalog-based analysis through both the RSP Portal and Notebook Aspects.

2213 Although the small DP1 dataset does not require Qserv’s full capabilities, we nevertheless chose to use it for DP1 to accurately reflect the future data access environment and to gain experience with scientifically-motivated queries ahead of full-scale deployment. Qserv is open-source and available on GitHub: <https://github.com/lsst/qserv>.

2219 6.5.2. Consolidated Database

2220 The Consolidated Database (ConsDB) (K.-T. Lim 2025) is an SQL-compatible database designed to store and manage metadata for Rubin Observatory science and calibration images. Metadata is recorded on a per-exposure basis and includes information such as the target name, pointing coordinates, observation time, physical filter and band, exposure duration, and environmental conditions (e.g., temperature, humidity, and wind speed). This key image metadata is also stored in the Butler Registry (§6.2.2), however the ConsDB stores additional information including derived metrics from image processing and information from the Engineering and Facility Database (EFD) transformed from the time dimension to the exposure dimension.

2233 The ConsDB schema is organized into instrument-specific tables, e.g., LSSTComCam and LSSTCam, facilitating instrument-specific queries. Within the LSSTComCam schema, data is further structured into tables for individual exposures and detectors. An example query on the DP1 dataset might retrieve all visits within a specified time range in the r-band for a given DP1 target.

2241 The ConsDB is hosted at the USDF. Following the initial release of DP1, a release of the DP1 exposure-specific ConsDB data will be made available through the RSP, and accessible externally via TAP. The detailed LSSTComCam

2244 schema can be found at: https://sdm-schemas.lsst.io/cdb_
 2245 [lsstcomcam.html](https://sdm-schemas.lsst.io/cdb_)

2246 7. SUPPORT FOR COMMUNITY SCIENCE

2247 The Rubin Observatory has a science community that en-
 2248 compasses thousands of individuals worldwide, with a broad
 2249 range of experience and expertise in astronomy in general,
 2250 and in the analysis of optical imaging data specifically.

2251 Rubin’s model to support this diverse community to ac-
 2252 cess and analyze DP1 emphasizes self-help via documenta-
 2253 tion and tutorials, and employs an open platform for asyn-
 2254 chronous issue reporting that enables crowd-sourced solu-
 2255 tions. These two aspects of community support are aug-
 2256 mented by virtual engagement activities. In addition, Rubin
 2257 supports its Users Committee to advocate on behalf of the
 2258 science community, and supports the eight LSST Science
 2259 Collaborations.

2260 All of the resources for scientists that are discussed in this
 2261 section are discoverable by browsing the For Scientists pages
 2262 of the Rubin Observatory website²⁰.

2263 7.1. Documentation

2264 The data release documentation for DP1 can be found
 2265 at dp1.lsst.io. The contents include an overview of the
 2266 LSSTComCam observations, descriptions of the data prod-
 2267 ucts (images and catalogs), and a high-level summary of the
 2268 processing pipelines. Similar to the contents of this paper,
 2269 but presented in a browsable, searchable webpage built with
 2270 Sphinx²¹, and written with a focus on applications of the
 2271 data products to scientific analysis.

2272 7.2. Tutorials

2273 A suite of tutorials that demonstrate how to access and
 2274 analyze DP1 using the RSP accompany the data release.
 2275 Jupyter Notebook tutorials are available via the “Tutorials”
 2276 drop-down menu within the Notebook aspect of the RSP.
 2277 Tutorials for the Portal and API aspects of the RSP can be
 2278 found in the data release documentation.

2279 These tutorials are designed to be inclusive, accessible,
 2280 clear, focused, and consistent. Their format and contents
 2281 follow a set of guidelines (M. L. Graham et al. 2025) that
 2282 are informed by industry standards in technical writing.

2283 7.3. Community Forum

2284 The venue for all user support is the Rubin Community
 2285 Forum²².

2286 Questions about any and all aspects of the Rubin data
 2287 products, pipelines, and services should be posted as new
 2288 topics in the Support category. This includes beginner-level
 2289 and “naive” questions, advanced scientific analysis questions,
 2290 technical bug reports, account and data access issues, and
 2291 everything in between. The Support category of the Forum
 2292 is monitored by Rubin staff, who aim to respond to all new
 2293 unsolved topics within 24 hours.

20 <https://rubinobservatory.org/>

21 <https://www.sphinx-doc.org/>

22 <https://community.lsst.org/>

2294 The Rubin Community Forum is built on the open-source
 2295 Discourse platform. It was chosen because, for a worldwide
 2296 community of ten thousand Rubin users, a traditional (i.e.,
 2297 closed) help desk represents a risk to Rubin science (e.g.,
 2298 many users with the same question having to wait for re-
 2299 sponses). The open nature of the Forum enables self-help
 2300 by letting users search for similar issues, and enables crowd-
 2301 sourced problem solving (and avoids knowledge bottlenecks)
 2302 by letting users help users.

2303 7.4. Engagement Activities

2304 A variety of live virtual and in-person workshops and sem-
 2305 inars offer learning opportunities to scientists and students
 2306 working with DP1.

- 2307 • Rubin Science Assemblies (weekly, virtual, 1 hour): al-
 2308 ternates between hands-on tutorials based on the most
 2309 recent data release and open drop-in “office hours”
 2310 with Rubin staff.
- 2311 • Rubin Data Academy (annual, virtual, 3-4 days): an
 2312 intense set of hands-on tutorials based on the most
 2313 recent data release, along with co-working and net-
 2314 working sessions.
- 2315 • Rubin Community Workshop (annual, virtual, 5 days),
 2316 a science-focused conference of contributed posters,
 2317 talks, and sessions led by members of the Rubin sci-
 2318 ence community and Rubin staff

2319 For schedules and connection information, visit the For
 2320 Scientists pages of the Rubin Observatory website. Requests
 2321 for custom tutorials and presentations for research groups
 2322 are also accommodated.

2323 7.5. Users Committee

2324 This committee is charged with soliciting feedback from
 2325 the science community, advocating on their behalf, and re-
 2326 commending science-driven improvements to the LSST data
 2327 products and the Rubin Science Platform tools and services.
 2328 Community members are encouraged to attend their virtual
 2329 meetings and raise issues to their attention, so they can be
 2330 included in the committee’s twice-yearly reports to the Ru-
 2331 bin Observatory Director.

2332 The community’s response to DP1 will be especially valu-
 2333 able input to DP2 and Data Release 1 (), and the Users
 2334 Committee encourages all users to interact with them. For
 2335 a list of members and contact information, visit the For Sci-
 2336 entists pages of the Rubin Observatory website.

2337 7.6. Science Collaborations

2338 The eight LSST Science Collaborations are independent,
 2339 worldwide communities of scientists, self-organized into col-
 2340 laborations based on their research interests and expertise.
 2341 Members work together to apply for funding, build software
 2342 infrastructure and analysis algorithms, and incorporate ex-
 2343 ternal data sets into their LSST-based research.

2344 The Science Collaborations also provide valuable advice
 2345 to Rubin Observatory on the operational strategies and data
 2346 products to accomplish specific science goals, and Rubin Ob-
 2347 servatory supports the collaborations via staff liaisons and
 2348 regular virtual meetings with Rubin operations leadership.

8. SUMMARY AND FUTURE RELEASES

Rubin Data Preview 1 (DP1) offers an initial look at the first on-sky data products and access services from the Vera C. Rubin Observatory. DP1 forms part of Rubin’s Early Science Program, and provides the scientific community with an early opportunity to familiarize themselves with the data formats and access infrastructure for the forthcoming Legacy Survey of Space and Time (LSST). This early release has a proprietary period of two years, during which time it is available to Rubin data rights holders only via the cloud-based Rubin Science Platform (RSP).

In this paper we have described the completion status of the observatory at the time of data acquisition, the commissioning campaign that forms the basis of DP1, and the processing pipelines used to produce early versions of data products. We provide details on the data products, their characteristics and known issues, and describe the RSP.

The data products described in this paper derive from observations obtained by LSSTComCam. LSSTComCam contains only around 5% the number of CCDs as the full LSST Science Camera (LSSTCam), yet the DP1 dataset that it has produced will already enable a very broad range of science. At 3.5 TB in size, DP1 covers a total area of ~ 15 sq. deg. and contains 1792 single-epoch images, 2644 deep coadded images, 2.3 million distinct astrophysical objects, including 93 new asteroid discoveries.

While some data products expected from the LSST are not yet available, e.g. cell-based coadds, several others have been provided in DP1 that will not be available in future releases. Difference images are included in DP1, but in future releases, these will be generated on-demand via services, rather than being provided as pre-produced products. The inclusion of these images in DP1 is possible due to the small dataset size, which makes it feasible to include them at this stage. As future releases will involve much larger datasets, this approach will no longer be possible.

The RSP is continually under development, and new functionality will continue to be deployed incrementally as it becomes available, and independent of future data releases. For

example, user query history capabilities, context-aware documentation and a bulk cutout services are just a few of the services currently under development.

Coincident with the release of DP1, Rubin Observatory begins its Science Validation Surveys with the LSST Science Camera. This final commissioning phase will produce a dataset that will form the foundation for the second Rubin Data Preview, DP2, expected around mid to late 2026. Full operations – marking the start of the LSST – is expected to commence by the end of 2025.

ACKNOWLEDGMENTS

This material is based upon work supported in part by the National Science Foundation through Cooperative Agreement AST-1258333 and Cooperative Support Agreement AST-1202910 managed by the Association of Universities for Research in Astronomy (AURA), and the Department of Energy under Contract No. DE-AC02-76SF00515 with the SLAC National Accelerator Laboratory managed by Stanford University. Additional Rubin Observatory funding comes from private donations, grants to universities, and in-kind support from LSSTC Institutional Members. This research has made use of NASA’s Astrophysics Data System Bibliographic Services.

Facilities: Rubin:Simonyi (LSSTComCam), USDAC, USDF

Software: Rubin Data Butler (T. Jenness et al. 2022), LSST Science Pipelines (Rubin Observatory Science Pipelines Developers 2025), LSST Feature Based Scheduler v3.0 (P. Yoachim et al. 2024; E. Naghib et al. 2019) Astropy (Astropy Collaboration et al. 2013, 2018, 2022) PIFF (M. Jarvis et al. 2021), GBDES (G. M. Bernstein 2022), Qserv (D. L. Wang et al. 2011; F. Mueller et al. 2023)

APPENDIX

Glossary

Adam: Adaptive Moment Estimation. 21

ADQL: Astronomical Data Query Language (IVOA standard). 41

ADU: Analogue-to-Digital Unit. 17

airmass: The pathlength of light from an astrophysical source through the Earth’s atmosphere. It is given approximately by $\sec z$, where z is the angular distance from the zenith (the point directly overhead, where airmass = 1.0) to the source. 16

Alert: A packet of information for each source detected with signal-to-noise ratio > 5 in a difference image by Alert Production, containing measurement and characterization parameters based on the past 12 months of

LSST observations plus small cutouts of the single-visit, template, and difference images, distributed via the internet. 15

Alert Production: Executing on the Prompt Processing system, the Alert Production payload processes and calibrates incoming images, performs Difference Image Analysis to identify DIASources and DIAObjects, and then packages the resulting alerts for distribution.. 21

algorithm: A computational implementation of a calculation or some method of processing. 3, 17, 20, 28

AOS: Active Optics System. 3

API: Application Programming Interface. 37, 40–42

arcmin: arcminute minute of arc (unit of angle). 28

ASPIC: Analog Signal Processing Integrated Circuit. 17

- astrometry:** In astronomy, the sub-discipline of astrometry concerns precision measurement of positions (at a reference epoch), and real and apparent motions of astrophysical objects. Real motion means 3-D motions of the object with respect to an inertial reference frame; apparent motions are an artifact of the motion of the Earth. Astrometry per se is sometimes confused with the act of determining a World Coordinate System (WCS), which is a functional characterization of the mapping from pixels in an image or spectrum to world coordinate such as (RA, Dec) or wavelength. [15](#), [31](#), [34](#)
- ATLAS:** Asteroid Terrestrial-impact Last Alert System. [15](#)
- AU:** deprecated acronym for astronomical unit; use **au** instead. [22](#)
- au:** astronomical unit. [22](#)
- B:** Byte (8 bit). [29](#), [30](#)
- background:** In an image, the background consists of contributions from the sky (e.g., clouds or scattered moonlight), and from the telescope and camera optics, which must be distinguished from the astrophysical background. The sky and instrumental backgrounds are characterized and removed by the LSST processing software using a low-order spatial function whose coefficients are recorded in the image metadata. [12](#), [13](#), [15](#), [18–20](#)
- Butler:** A middleware component for persisting and retrieving image datasets (raw or processed), calibration reference data, and catalogs. [11](#), [13](#), [16](#), [41](#), [42](#)
- CADC:** Canadian Astronomy Data Centre. [41](#)
- cadence:** The sequence of pointings, visit exposures, and exposure durations performed over the course of a survey. [1](#)
- calibration:** The process of translating signals produced by a measuring instrument such as a telescope and camera into physical units such as flux, which are used for scientific analysis. Calibration removes most of the contributions to the signal from environmental and instrumental factors, such that only the astronomical component remains. [4](#), [11](#), [12](#), [15](#), [17–19](#), [28](#)
- Camera:** The LSST subsystem responsible for the 3.2-gigapixel LSST camera, which will take more than 800 panoramic images of the sky every night. SLAC leads a consortium of Department of Energy laboratories to design and build the camera sensors, optics, electronics, cryostat, filters and filter exchange mechanism, and camera control system. [1](#), [2](#)
- camera:** An imaging device mounted at a telescope focal plane, composed of optics, a shutter, a set of filters, and one or more sensors arranged in a focal plane array. [9–11](#), [16](#), [17](#), [19](#), [28](#)
- CBP:** Collimated Beam Projector. [4](#)
- CCD:** Charge-Coupled Device. [4](#), [10–12](#), [19](#), [28](#), [35](#)
- Center:** An entity managed by AURA that is responsible for execution of a federally funded project. [15](#), [21](#), [35](#)
- Charge-Coupled Device:** a particular kind of solid-state sensor for detecting optical-band photons. It is composed of a 2-D array of pixels, and one or more read-out amplifiers. [4](#)
- cloud:** A visible mass of condensed water vapor floating in the atmosphere, typically high above the ground or in interstellar space acting as the birthplace for stars. Also a way of computing (on other peoples computers leveraging their services and availability).. [1](#), [2](#), [38–40](#)
- Collimated Beam Projector:** The hardware to project a field of sources onto discrete sections of the telescope optics in order to characterize spatial variations in the telescope and instrument transmission function, and to monitor filter throughput evolution during the survey. Images obtained using the CBP will be used in calibration. [4](#)
- Commissioning:** A two-year phase at the end of the Construction project during which a technical team a) integrates the various technical components of the three subsystems; b) shows their compliance with ICDs and system-level requirements as detailed in the LSST Observatory System Specifications document (OSS, LSE-30); and c) performs science verification to show compliance with the survey performance specifications as detailed in the LSST Science Requirements Document (SRD, LPM-17). [1](#), [2](#)
- configuration:** A task-specific set of configuration parameters, also called a 'config'. The config is read-only; once a task is constructed, the same configuration will be used to process all data. This makes the data processing more predictable: it does not depend on the order in which items of data are processed. This is distinct from arguments or options, which are allowed to vary from one task invocation to the next. [3](#), [4](#), [16](#)
- CPU:** Central Processing Unit. [21](#)
- CTI:** Charge Transfer Inefficiency. [4](#), [11](#), [17](#)
- Data Management System:** The computing infrastructure, middleware, and applications that process, store, and enable information extraction from the LSST dataset; the DMS will process peta-scale data volume, convert raw images into a faithful representation of the universe, and archive the results in a useful form. The infrastructure layer consists of the computing, storage, networking hardware, and system software. The middleware layer handles distributed processing, data access, user interface, and system operations services. The applications layer includes the data pipelines and the science data archives' products and services. [1](#)
- Data Release:** The approximately annual reprocessing of all LSST data, and the installation of the resulting data products in the LSST Data Access Centers, which marks the start of the two-year proprietary period. [13](#), [15](#)

- 2557 **Data Release Processing:** Deprecated term; see Data
2558 Release Production. 17
- 2559 **DC2:** Data Challenge 2 (DESC). 28, 30, 31
- 2560 **DCR:** Differential Chromatic Refraction. 15, 19, 34
- 2561 **deblend:** Deblending is the act of inferring the intensity
2562 profiles of two or more overlapping sources from a
2563 single footprint within an image. Source footprints
2564 may overlap in crowded fields, or where the astrophysical
2565 phenomena intrinsically overlap (e.g., a supernova
2566 embedded in an external galaxy), or by spatial coincidence
2567 (e.g., an asteroid passing in front of a star). Deblending
2568 may make use of a priori information from images (e.g.,
2569 deep CoAdds or visit images obtained in good seeing),
2570 from catalogs, or from models. A 'deblend' is commonly
2571 referred to in terms of 'parent' (total) and 'child'
2572 (component) objects. 20
- 2573 **deg:** degree; unit of angle. 22
- 2574 **Department of Energy:** cabinet department of the
2575 United States federal government; the DOE has assumed
2576 technical and financial responsibility for providing the
2577 LSST camera. The DOE's responsibilities are executed by
2578 a collaboration led by SLAC National Accelerator
2579 Laboratory. 1
- 2580 **DES:** Dark Energy Survey. 15, 25
- 2581 **DESC:** Dark Energy Science Collaboration. 28
- 2582 **DIA:** Difference Image Analysis. 17
- 2583 **Difference Image Analysis:** The detection and
2584 characterization of sources in the Difference Image that
2585 are above a configurable threshold, done as part of Alert
2586 Generation Pipeline. 17
- 2587 **Differential Chromatic Refraction:** The refraction of
2588 incident light by Earth's atmosphere causes the apparent
2589 position of objects to be shifted, and the size of this
2590 shift depends on both the wavelength of the source and
2591 its airmass at the time of observation. DCR corrections
2592 are done as a part of DIA. 15, 34
- 2593 **DIMM:** Differential Image Motion Monitor. 9
- 2594 **Director:** The person responsible for the overall
2595 conduct of the project; the LSST director is charged with
2596 ensuring that both the scientific goals and management
2597 constraints on the project are met. S/he is the principal
2598 public spokesperson for the project in all matters and
2599 represents the project to the scientific community, AURA,
2600 the member institutions of LSSTC, and the funding
2601 agencies. 45
- 2602 **Document:** Any object (in any application supported
2603 by DocuShare or design archives such as PDMWorks or
2604 GIT) that supports project management or records
2605 milestones and deliverables of the LSST Project. 10
- 2606 **DOE:** Department of Energy. 1
- 2607 **DP0:** Data Preview 0. 2
- 2608 **DP1:** Data Preview 1. 1–6, 8–19, 21–23, 26, 28, 35–37,
2609 42, 44–46
- 2610 **DP2:** Data Preview 2. 2, 41, 42, 45, 46
- 2611 **DPDD:** Data Product Definition Document. 10
- 2612 **DR1:** Data Release 1. 45
- 2613 **DR3:** Data Release 3. 15, 19, 28
- 2614 **DRP:** Data Release Processing. 17
- 2615 **E2V:** Teledyne. 4
- 2616 **ECDFS:** Extended Chandra Deep Field-South Survey. 6,
2617 25, 27, 28, 31, 35, 37, 38
- 2618 **Education and Public Outreach:** The LSST subsystem
2619 responsible for the cyberinfrastructure, user interfaces,
2620 and outreach programs necessary to connect educators,
2621 planetaria, citizen scientists, amateur astronomers,
2622 and the general public to the transformative LSST
2623 dataset. 1
- 2624 **efd:** Engineering and Facility Database. 44
- 2625 **EPO:** Education and Public Outreach. 1
- 2626 **epoch:** Sky coordinate reference frame, e.g., J2000.
2627 Alternatively refers to a single observation (usually
2628 photometric, can be multi-band) of a variable source. 2,
2629 5, 8, 10, 13, 14, 19, 20, 46
- 2630 **ESO:** European Southern Observatory. 15
- 2631 **FBS:** Feature-Based Scheduler. 5
- 2632 **FGCM:** Forward Global Calibration Model. 19
- 2633 **Firefly:** A framework of software components written
2634 by IPAC for building web-based user interfaces to
2635 astronomical archives, through which data may be
2636 searched and retrieved, and viewed as FITS images,
2637 catalogs, and/or plots. Firefly tools will be
2638 integrated into the Science Platform. 43
- 2639 **FITS:** Flexible Image Transport System. 16
- 2640 **Flexible Image Transport System:** an international
2641 standard in astronomy for storing images, tables,
2642 and metadata in disk files. See the IAU FITS
2643 Standard for details. 16
- 2644 **flux:** Shorthand for radiative flux, it is a
2645 measure of the transport of radiant energy per unit
2646 area per unit time. In astronomy this is usually
2647 expressed in cgs units: erg/cm²/s. 12–15, 18,
2648 20, 28, 36
- 2649 **forced photometry:** A measurement of the
2650 photometric properties of a source, or expected
2651 source, with one or more parameters held fixed.
2652 Most often this means fixing the location of the
2653 center of the brightness profile (which may be
2654 known or predicted in advance), and measuring
2655 other properties such as total brightness, shape,
2656 and orientation. Forced photometry will be done
2657 for all Objects in the Data Release Production.
2658 14, 20, 21
- 2659 **FOV:** field of view. 8
- 2660 **FrDF:** French Data Facility. 17
- 2661 **FWHM:** Full Width at Half-Maximum. 1, 3, 10,
2662 12, 13
- 2663 **GAaP:** Gaussian Aperture and PSF. 30, 33

- Gaia:** a space observatory of the European Space Agency, launched in 2013 and expected to operate until 2025. The spacecraft is designed for astrometry: measuring the positions, distances and motions of stars with unprecedented precision. 15
- Gaussian Aperture and PSF:** involves Gaussianizing the PSFs and then using a Gaussian aperture (instead of top-hat) for measuring photometry. The aperture+PSF is designed to be the same across all bands, so that you measure consistent colors.. 30
- HEALPix:** Hierarchical Equal-Area iso-Latitude Pixelisation. 15, 16
- HiPS:** Hierarchical Progressive Survey (IVOA standard). 15, 16, 41
- HSM:** Half-Second Moment. 23
- IAU:** International Astronomical Union. 15
- ISR:** Instrument Signal Removal. 17, 18
- ITL:** Imaging Technology Laboratory (UA). 4, 7, 19, 24, 25, 28
- IVOA:** International Virtual-Observatory Alliance. 11, 13, 15, 40, 41
- LSST:** Legacy Survey of Space and Time (formerly Large Synoptic Survey Telescope). 1–4, 6, 8, 10, 13, 15, 35, 37, 43, 45, 46
- LSST Science Pipelines:** software used to perform the LSST data reduction pipelines.lsst.io. 4, 17, 18, 40, 43
- LSSTCam:** LSST Science Camera. 2–4, 8, 28, 35
- LSSTComCam:** Rubin Commissioning Camera. 2–6, 8, 10–12, 17, 19, 21–23, 26, 35, 44–46
- M1M3:** Primary Mirror Tertiary Mirror. 3
- M2:** Secondary Mirror. 3
- metadata:** General term for data about data, e.g., attributes of astronomical objects (e.g. images, sources, astroObjects, etc.) that are characteristics of the objects themselves, and facilitate the organization, preservation, and query of data sets. (E.g., a FITS header contains metadata). 12, 13, 16, 41
- metric:** A measurable quantity which may be tracked. A metric has a name, description, unit, references, and tags (which are used for grouping). A metric is a scalar by definition. See also: aggregate metric, model metric, point metric. 28
- middleware:** Software that acts as a bridge between other systems or software usually a database or network. Specifically in the Data Management System this refers to Butler for data access and Workflow management for distributed processing.. 17
- MPC:** Minor Planet Center. 35
- MPCORB:** Minor Planet Center Orbit database. 15
- National Science Foundation:** primary federal agency supporting research in all fields of fundamental science and engineering; NSF selects and funds projects through competitive, merit-based review. 1
- NEO:** Near-Earth Object. 22
- NSF:** National Science Foundation. 1
- Object:** In LSST nomenclature this refers to an astronomical object, such as a star, galaxy, or other physical entity. E.g., comets, asteroids are also Objects but typically called a Moving Object or a Solar System Object (SSObject). One of the DRP data products is a table of Objects detected by LSST which can be static, or change brightness or position with time. 8, 22, 41
- Operations:** The 10-year period following construction and commissioning during which the LSST Observatory conducts its survey. 41
- Pan-STARRS:** Panoramic Survey Telescope and Rapid Response System. 15
- patch:** An quadrilateral sub-region of a sky tract, with a size in pixels chosen to fit easily into memory on desktop computers. 11–13, 15, 42
- pipeline:** A configured sequence of software tasks (Stages) to process data and generate data products. Example: Association Pipeline. 11, 17, 22, 35
- PNG:** Portable Network Graphics. 16
- POSIX:** Portable Operating System Interface. 41
- provenance:** Information about how LSST images, Sources, and Objects were created (e.g., versions of pipelines, algorithmic components, or templates) and how to recreate them. 16
- PSF:** Point Spread Function. 3, 10, 12–16, 19–21, 23, 25, 35, 39
- PTC:** Photon Transfer Curve. 17
- Qserv:** LSST’s distributed parallel database. This database system is used for collecting, storing, and serving LSST Data Release Catalogs and Project metadata, and is part of the Software Stack. 13, 40, 41, 43, 44
- RA:** Rapid Analysis. 28, 35
- REB:** Readout Electronics Board. 17, 18
- Release:** Publication of a new version of a document, software, or data product. Depending on context, releases may require approval from Project- or DM-level change control boards, and then form part of the formal project baseline. 15, 45
- REST:** REpresentational State Transfer. 41
- RINGSS:** Ring-Image Next Generation Scintillation Sensor. 9
- RMS:** Root-Mean-Square. 28
- RSP:** Rubin Science Platform. 16, 37–39, 41–46

- 2761 **Rubin Operations:** operations phase of Vera C. Rubin Ob-
2762 servatory. 19
- 2763 **S3:** (Amazon) Simple Storage Service. 41
- 2764 **S3DF:** SLAC Shared Scientific Data Facility. 21
- 2765 **schema:** The definition of the metadata and linkages be-
2766 tween datasets and metadata entities in a collection of
2767 data or archive.. 13, 43
- 2768 **Science Collaboration:** An autonomous body of scientists
2769 interested in a particular area of science enabled by the
2770 LSST dataset, which through precursor studies, sim-
2771 ulations, and algorithm development lays the ground-
2772 work for the large-scale science projects the LSST will
2773 enable. In addition to preparing their members to take
2774 full advantage of LSST early in its operations phase,
2775 the science collaborations have helped to define the
2776 system’s science requirements, refine and promote the
2777 science case, and quality check design and development
2778 work. 28
- 2779 **Science Pipelines:** The library of software components
2780 and the algorithms and processing pipelines assembled
2781 from them that are being developed by DM to generate
2782 science-ready data products from LSST images. The
2783 Pipelines may be executed at scale as part of LSST
2784 Prompt or Data Release processing, or pieces of them
2785 may be used in a standalone mode or executed through
2786 the Rubin Science Platform. The Science Pipelines are
2787 one component of the LSST Software Stack. 3, 26
- 2788 **Science Platform:** A set of integrated web applications
2789 and services deployed at the LSST Data Access Cen-
2790 ters (DACs) through which the scientific community
2791 will access, visualize, and perform next-to-the-data
2792 analysis of the LSST data products. 1, 2, 16, 37, 40,
2793 44
- 2794 **SDSS:** Sloan Digital Sky Survey. 15
- 2795 **seeing:** An astronomical term for characterizing the stabil-
2796 ity of the atmosphere, as measured by the width of
2797 the point-spread function on images. The PSF width
2798 is also affected by a number of other factors, including
2799 the airmass, passband, and the telescope and camera
2800 optics. 1, 3, 10, 13, 20
- 2801 **Sensor:** A sensor is a generic term for a light-sensitive detec-
2802 tor, such as a CCD. For LSST, sensors consist of a 2-D
2803 array of roughly 4K x 4K pixels, which are mounted
2804 on a raft in a 3x3 mosaic. Each sensor is divided into
2805 16 channels or amplifiers. The 9 sensors that make up
2806 a raft are numbered from "0,0" through "2,2". 9
- 2807 **shape:** In reference to a Source or Object, the shape is a
2808 functional characterization of its spatial intensity dis-
2809 tribution, and the integral of the shape is the flux.
2810 Shape characterizations are a data product in the DI-
2811 ASource, DIAObject, Source, and Object catalogs. 14,
2812 15, 21, 25, 35
- 2813 **Simonyi Survey Telescope:** The telescope at the Rubin
2814 Observatory that will perform the LSST (this refers
2815 to all physical components: the mirror, the mount as-
2816 sembly, etc.).. 1
- 2817 **sky map:** A sky tessellation for LSST. The Stack includes
2818 software to define a geometric mapping from the repre-
2819 sentation of World Coordinates in input images to the
2820 LSST sky map. This tessellation is comprised of indi-
2821 vidual tracts which are, in turn, comprised of patches.
2822 42
- 2823 **SLAC:** SLAC National Accelerator Laboratory. 21, 24
- 2824 **SLAC National Accelerator Laboratory:** A national
2825 laboratory funded by the US Department of Energy
2826 (DOE); SLAC leads a consortium of DOE laboratories
2827 that has assumed responsibility for providing the
2828 LSST camera. Although the Camera project manages
2829 its own schedule and budget, including contingency,
2830 the Camera team’s schedule and requirements are
2831 integrated with the larger Project. The camera effort
2832 is accountable to the LSSTPO.. 21
- 2833 **Sloan Digital Sky Survey:** is a digital survey of roughly
2834 10,000 square degrees of sky around the north Galactic
2835 pole, plus a 300 square degree stripe along the celestial
2836 equator. 15
- 2837 **SLR:** Stellar Locus Regression. 15
- 2838 **SNR:** Signal to Noise Ratio. 19, 34, 35
- 2839 **SOAR:** Southern Astrophysical Research Telescope. 9
- 2840 **SODA:** Server-side Operations for Data Access (IVOA stan-
2841 dard). 41
- 2842 **software:** The programs and other operating information
2843 used by a computer.. 26, 43
- 2844 **Source:** A single detection of an astrophysical object in an
2845 image, the characteristics for which are stored in the
2846 Source Catalog of the DRP database. The association
2847 of Sources that are non-moving lead to Objects; the
2848 association of moving Sources leads to Solar System
2849 Objects. (Note that in non-LSST usage "source" is
2850 often used for what LSST calls an Object.). 20
- 2851 **SQL:** Structured Query Language. 41
- 2852 **TAP:** Table Access Protocol (IVOA standard). 13, 40–42
- 2853 **TOPCAT:** Tool for OPERations on Catalogues And Tables.
2854 42
- 2855 **tracklet:** Links between unassociated DIASources within
2856 one night to identify moving objects. 21, 22
- 2857 **tract:** A portion of sky, a spherical convex polygon, within
2858 the LSST all-sky tessellation (sky map). Each tract is
2859 subdivided into sky patches. 11, 15, 16, 19, 28, 29
- 2860 **transient:** A transient source is one that has been detected
2861 on a difference image, but has not been associated with
2862 either an astronomical object or a solar system body.
2863 2, 12, 14, 20
- 2864 **UA:** University of Arizona. 4
- 2865 **UKDF:** United Kingdom Data Facility. 17
- 2866 **USDF:** United States Data Facility. 17, 39, 40, 44
- 2867 **VLT:** Very Large Telescope (ESO). 15

- 2868 **VO:** Virtual Observatory. 40
- 2869 **VST:** VLT Survey Telescope. 15
- 2870 **WCS:** World Coordinate System. 12, 13, 20, 26
- 2871 **WebDav:** Web Distributed Authoring and Versioning. 41
- 2872 **WFD:** Wide Fast Deep. 4
- 2873 **World Coordinate System:** a mapping from image pixel
2874 coordinates to physical coordinates; in the case of im-
- 2875 ages the mapping is to sky coordinates, generally in an
2876 equatorial (RA, Dec) system. The WCS is expressed
2877 in FITS file extensions as a collection of header key-
2878 word=value pairs (basically, the values of parameters
2879 for a selected functional representation of the map-
2880 ping) that are specified in the FITS Standard. 12
- 2881 **XP:** B or R Photometry (Gaia). 15

REFERENCES

- 2882 Ahumada, R., Allende Prieto, C., Almeida, A., et al. 2020,
2883 ApJS, 249, 3, doi: [10.3847/1538-4365/ab929e](https://doi.org/10.3847/1538-4365/ab929e)
- 2884 Aihara, H., AIsayyad, Y., Ando, M., et al. 2022, PASJ, 74,
2885 247, doi: [10.1093/pasj/psab122](https://doi.org/10.1093/pasj/psab122)
- 2886 Allbery, R. 2023, IVOA SODA implementation experience,
2887 SQuaRE Technical Note SQR-063, Vera C. Rubin
2888 Observatory. <https://sqr-063.lsst.io/>
- 2889 Allbery, R. 2024, Draft IVOA SODA web service
2890 specification, SQuaRE Technical Note SQR-093, Vera C.
2891 Rubin Observatory. <https://sqr-093.lsst.io/>
- 2892 AIsayyad, Y. 2019, Coaddition Artifact Rejection and
2893 CompareWarp, Data Management Technical Note
2894 DMTN-080, Vera C. Rubin Observatory.
2895 <https://dmtn-080.lsst.io/>
- 2896 Ansel, J., Yang, E., He, H., et al. 2024, in 29th ACM
2897 International Conference on Architectural Support for
2898 Programming Languages and Operating Systems, Volume
2899 2 (ASPLOS '24) (ACM), doi: [10.1145/3620665.3640366](https://doi.org/10.1145/3620665.3640366)
- 2900 Astropy Collaboration, Robitaille, T. P., Tollerud, E. J.,
2901 et al. 2013, A&A, 558, A33,
2902 doi: [10.1051/0004-6361/201322068](https://doi.org/10.1051/0004-6361/201322068)
- 2903 Astropy Collaboration, Price-Whelan, A. M., Sipőcz, B. M.,
2904 et al. 2018, AJ, 156, 123, doi: [10.3847/1538-3881/aabc4f](https://doi.org/10.3847/1538-3881/aabc4f)
- 2905 Astropy Collaboration, Price-Whelan, A. M., Lim, P. L.,
2906 et al. 2022, ApJ, 935, 167, doi: [10.3847/1538-4357/ac7c74](https://doi.org/10.3847/1538-4357/ac7c74)
- 2907 Baumann, M., Boch, T., Pineau, F.-X., et al. 2022, in
2908 Astronomical Society of the Pacific Conference Series,
2909 Vol. 532, Astronomical Data Analysis Software and
2910 Systems XXX, ed. J. E. Ruiz, F. Pierfederici, &
2911 P. Teuben, 7
- 2912 Bechtol, K., Sevilla-Noarbe, I., Drlica-Wagner, A., et al.
2913 2025, arXiv e-prints, arXiv:2501.05739,
2914 doi: [10.48550/arXiv.2501.05739](https://doi.org/10.48550/arXiv.2501.05739)
- 2915 Berk, A., Anderson, G. P., Bernstein, L. S., et al. 1999, in
2916 Society of Photo-Optical Instrumentation Engineers
2917 (SPIE) Conference Series, Vol. 3756, Optical
2918 Spectroscopic Techniques and Instrumentation for
2919 Atmospheric and Space Research III, ed. A. M. Larar,
2920 348–353, doi: [10.1117/12.366388](https://doi.org/10.1117/12.366388)
- 2921 Bernstein, G. M. 2022, gbdes: DECam instrumental
2922 signature fitting and processing programs,, Astrophysics
2923 Source Code Library, record ascl:2210.011
- 2924 Bernstein, G. M., Armstrong, R., Plazas, A. A., et al. 2017,
2925 PASP, 129, 074503, doi: [10.1088/1538-3873/aa6c55](https://doi.org/10.1088/1538-3873/aa6c55)
- 2926 Bertin, E. 2011, in Astronomical Society of the Pacific
2927 Conference Series, Vol. 442, Astronomical Data Analysis
2928 Software and Systems XX, ed. I. N. Evans,
2929 A. Accomazzi, D. J. Mink, & A. H. Rots, 435
- 2930 Blum, R., & the Rubin Operations Team. 2020, Vera C.
2931 Rubin Observatory Data Policy, Data Management
2932 Operations Controlled Document RDO-013, Vera C.
2933 Rubin Observatory. <https://ls.st/RDO-013>
- 2934 Boch, T., & Fernique, P. 2014, in Astronomical Society of
2935 the Pacific Conference Series, Vol. 485, Astronomical
2936 Data Analysis Software and Systems XXIII, ed.
2937 N. Manset & P. Forshay, 277
- 2938 Bonnarel, F., Dowler, P., Demleitner, M., Tody, D., &
2939 Dempsey, J. 2017, IVOA Server-side Operations for Data
2940 Access Version 1.0,, IVOA Recommendation 17 May 2017
2941 doi: [10.5479/ADS/bib/2017ivoa.spec.0517B](https://doi.org/10.5479/ADS/bib/2017ivoa.spec.0517B)
- 2942 Bonnarel, F., Fernique, P., Bienaymé, O., et al. 2000,
2943 A&AS, 143, 33, doi: [10.1051/aas:2000331](https://doi.org/10.1051/aas:2000331)
- 2944 Bosch, J., Armstrong, R., Bickerton, S., et al. 2018, PASJ,
2945 70, S5, doi: [10.1093/pasj/psx080](https://doi.org/10.1093/pasj/psx080)
- 2946 Broughton, A., Utsumi, Y., Plazas Malagón, A. A., et al.
2947 2024, PASP, 136, 045003, doi: [10.1088/1538-3873/ad3aa2](https://doi.org/10.1088/1538-3873/ad3aa2)
- 2948 Burke, D. L., Rykoff, E. S., Allam, S., et al. 2018, AJ, 155,
2949 41, doi: [10.3847/1538-3881/aa9f22](https://doi.org/10.3847/1538-3881/aa9f22)
- 2950 Chambers, K. C., Magnier, E. A., Metcalfe, N., et al. 2016,
2951 arXiv e-prints, arXiv:1612.05560,
2952 doi: [10.48550/arXiv.1612.05560](https://doi.org/10.48550/arXiv.1612.05560)
- 2953 de Vaucouleurs, G. 1948, Annales d'Astrophysique, 11, 247
- 2954 de Vaucouleurs, G. 1953, MNRAS, 113, 134,
2955 doi: [10.1093/mnras/113.2.134](https://doi.org/10.1093/mnras/113.2.134)
- 2956 Dowler, P., Bonnarel, F., & Tody, D. 2015, IVOA Simple
2957 Image Access Version 2.0,, IVOA Recommendation 23
2958 December 2015
2959 doi: [10.5479/ADS/bib/2015ivoa.spec.1223D](https://doi.org/10.5479/ADS/bib/2015ivoa.spec.1223D)

- 2960 Dowler, P., Rixon, G., Tody, D., & Demleitner, M. 2019,
2961 Table Access Protocol Version 1.1., IVOA
2962 Recommendation 27 September 2019
- 2963 Economou, F. 2023, The Rubin Science Platform, Data
2964 Management Technical Note DMTN-212, Vera C. Rubin
2965 Observatory. <https://dmtn-212.lsst.io/>
- 2966 Eggl, S., Juric, M., Moeyens, J., & Jones, L. 2020, in
2967 AAS/Division for Planetary Sciences Meeting Abstracts,
2968 Vol. 52, AAS/Division for Planetary Sciences Meeting
2969 Abstracts, 211.01
- 2970 Esteves, J. H., Utsumi, Y., Snyder, A., et al. 2023, PASP,
2971 135, 115003, doi: [10.1088/1538-3873/ad0a73](https://doi.org/10.1088/1538-3873/ad0a73)
- 2972 Euclid Collaboration, Romelli, E., Kümmel, M., et al. 2025,
2973 arXiv e-prints, arXiv:2503.15305,
2974 doi: [10.48550/arXiv.2503.15305](https://doi.org/10.48550/arXiv.2503.15305)
- 2975 Fagrelus, P., & Rykoff, E. 2025, Rubin Baseline Calibration
2976 Plan, Commissioning Technical Note SITCOMTN-086,
2977 Vera C. Rubin Observatory. <https://sitcomtn-086.lsst.io/>
- 2978 Ferguson, P., Rykoff, E., Carlin, J., Saunders, C., &
2979 Parejko, J. 2025, The Monster: A reference catalog with
2980 synthetic ugrizy-band fluxes for the Vera C. Rubin
2981 observatory, Data Management Technical Note
2982 DMTN-277, Vera C. Rubin Observatory.
2983 <https://dmtn-277.lsst.io/>
- 2984 Fernique, P., Allen, M. G., Boch, T., et al. 2015, A&A, 578,
2985 A114, doi: [10.1051/0004-6361/201526075](https://doi.org/10.1051/0004-6361/201526075)
- 2986 Fernique, P., Allen, M., Boch, T., et al. 2017, HiPS -
2987 Hierarchical Progressive Survey Version 1.0., IVOA
2988 Recommendation 19 May 2017
2989 doi: [10.5479/ADS/bib/2017ivoa.spec.0519F](https://doi.org/10.5479/ADS/bib/2017ivoa.spec.0519F)
- 2990 Fortino, W. F., Bernstein, G. M., Bernardinelli, P. H., et al.
2991 2021, AJ, 162, 106, doi: [10.3847/1538-3881/ac0722](https://doi.org/10.3847/1538-3881/ac0722)
- 2992 Gaia Collaboration, Montegriffo, P., Bellazzini, M., et al.
2993 2023, A&A, 674, A33, doi: [10.1051/0004-6361/202243709](https://doi.org/10.1051/0004-6361/202243709)
- 2994 Górski, K. M., Hivon, E., Banday, A. J., et al. 2005, ApJ,
2995 622, 759, doi: [10.1086/427976](https://doi.org/10.1086/427976)
- 2996 Graham, M., Plante, R., Tody, D., & Fitzpatrick, M. 2014,
2997 PyVO: Python access to the Virtual Observatory,,
2998 Astrophysics Source Code Library, record ascl:1402.004
- 2999 Graham, M. L., Carlin, J. L., Adair, C. L., et al. 2025,
3000 Guidelines for User Tutorials, Technical Note RTN-045,
3001 Vera C. Rubin Observatory. <https://rtn-045.lsst.io/>
- 3002 Gray, B. 2025, find_orb: Orbit determination from
3003 observations,
- 3004 Guy, L. P., Bechtol, K., Bellm, E., et al. 2025, Rubin
3005 Observatory Plans for an Early Science Program,
3006 Technical Note RTN-011, Vera C. Rubin Observatory,
3007 doi: [10.5281/zenodo.5683848](https://doi.org/10.5281/zenodo.5683848)
- 3008 Heinze, A., Eggl, S., Juric, M., et al. 2022, in AAS/Division
3009 for Planetary Sciences Meeting Abstracts, Vol. 54,
3010 AAS/Division for Planetary Sciences Meeting Abstracts,
3011 504.04
- 3012 Heinze, A., Juric, M., & Kurlander, J. 2023, helioline: Open
3013 Source Solar System Discovery Software,
- 3014 Hirata, C., & Seljak, U. 2003, MNRAS, 343, 459,
3015 doi: [10.1046/j.1365-8711.2003.06683.x](https://doi.org/10.1046/j.1365-8711.2003.06683.x)
- 3016 Holman, M. J., Payne, M. J., Blankley, P., Janssen, R., &
3017 Kuindersma, S. 2018, AJ, 156, 135,
3018 doi: [10.3847/1538-3881/aad69a](https://doi.org/10.3847/1538-3881/aad69a)
- 3019 Homar, G. M., Tighe, R., Thomas, S., et al. 2024, in
3020 Ground-based and Airborne Telescopes X, ed. H. K.
3021 Marshall, J. Spyromilio, & T. Usuda, Vol. 13094,
3022 International Society for Optics and Photonics (SPIE),
3023 130943C, doi: [10.1117/12.3019031](https://doi.org/10.1117/12.3019031)
- 3024 Howard, J., Reil, K., Claver, C., et al. 2018, in Society of
3025 Photo-Optical Instrumentation Engineers (SPIE)
3026 Conference Series, Vol. 10700, Ground-based and
3027 Airborne Telescopes VII, ed. H. K. Marshall &
3028 J. Spyromilio, 107003D, doi: [10.1117/12.2312684](https://doi.org/10.1117/12.2312684)
- 3029 Illingworth, G., Magee, D., Bouwens, R., et al. 2016, arXiv
3030 e-prints, arXiv:1606.00841,
3031 doi: [10.48550/arXiv.1606.00841](https://doi.org/10.48550/arXiv.1606.00841)
- 3032 Ingraham, P., Fagrelus, P., Stubbs, C. W., et al. 2022, in
3033 Society of Photo-Optical Instrumentation Engineers
3034 (SPIE) Conference Series, Vol. 12182, Ground-based and
3035 Airborne Telescopes IX, ed. H. K. Marshall,
3036 J. Spyromilio, & T. Usuda, 121820R,
3037 doi: [10.1117/12.2630185](https://doi.org/10.1117/12.2630185)
- 3038 Ivezić, Z. 2022, Survey Cadence Optimization Committee's
3039 Phase 1 Recommendation, Project Science Technical
3040 Note PSTN-053, Vera C. Rubin Observatory.
3041 <https://pstn-053.lsst.io/>
- 3042 Ivezić, Ž., & The LSST Science Collaboration. 2018, LSST
3043 Science Requirements Document, Project Controlled
3044 Document LPM-17, Vera C. Rubin Observatory.
3045 <https://ls.st/LPM-17>
- 3046 Ivezić, Ž., Kahn, S. M., Tyson, J. A., et al. 2019a, ApJ,
3047 873, 111, doi: [10.3847/1538-4357/ab042c](https://doi.org/10.3847/1538-4357/ab042c)
- 3048 Ivezić, Ž., Kahn, S. M., Tyson, J. A., et al. 2019b, ApJ,
3049 873, 111, doi: [10.3847/1538-4357/ab042c](https://doi.org/10.3847/1538-4357/ab042c)
- 3050 Jarvis, M., et al. 2021, Mon. Not. Roy. Astron. Soc., 501,
3051 1282, doi: [10.1093/mnras/staa3679](https://doi.org/10.1093/mnras/staa3679)
- 3052 Jenness, T., & Dubois-Felsmann, G. P. 2025, IVOA
3053 Identifier Usage at the Rubin Observatory, Data
3054 Management Technical Note DMTN-302, Vera C. Rubin
3055 Observatory. <https://dmtn-302.lsst.io/>

- 3056 Jenness, T., Voutsinas, S., Dubois-Felsmann, G. P., &
3057 Salnikov, A. 2024, arXiv e-prints, arXiv:2501.00544,
3058 doi: [10.48550/arXiv.2501.00544](https://doi.org/10.48550/arXiv.2501.00544)
- 3059 Jenness, T., Bosch, J. F., Salnikov, A., et al. 2022, in
3060 Society of Photo-Optical Instrumentation Engineers
3061 (SPIE) Conference Series, Vol. 12189, Software and
3062 Cyberinfrastructure for Astronomy VII, 1218911,
3063 doi: [10.1117/12.2629569](https://doi.org/10.1117/12.2629569)
- 3064 Jones, R. L. 2021, Survey Strategy and Cadence Choices
3065 for the Vera C. Rubin Observatory Legacy Survey of
3066 Space and Time (LSST), Project Science Technical Note
3067 PSTN-051, Vera C. Rubin Observatory.
3068 <https://pstn-051.lsst.io/>
- 3069 Juric, M. 2025, mpsky: Multi-purpose sky catalog
3070 cross-matching,
- 3071 Jurić, M., Ciardi, D., Dubois-Felsmann, G., & Guy, L.
3072 2019, LSST Science Platform Vision Document, Systems
3073 Engineering Controlled Document LSE-319, Vera C.
3074 Rubin Observatory. <https://lse-319.lsst.io/>
- 3075 Jurić, M., Axelrod, T., Becker, A., et al. 2023, Data
3076 Products Definition Document, Systems Engineering
3077 Controlled Document LSE-163, Vera C. Rubin
3078 Observatory. <https://lse-163.lsst.io/>
- 3079 Kannawadi, A. 2022, Consistent galaxy colors with
3080 Gaussian-Aperture and PSF photometry, Data
3081 Management Technical Note DMTN-190, Vera C. Rubin
3082 Observatory. <https://dmtn-190.lsst.io/>
- 3083 Kron, R. G. 1980, ApJS, 43, 305, doi: [10.1086/190669](https://doi.org/10.1086/190669)
- 3084 Kuijken, K. 2008, A&A, 482, 1053,
3085 doi: [10.1051/0004-6361/20066601](https://doi.org/10.1051/0004-6361/20066601)
- 3086 Lange, T., Nordby, M., Pollek, H., et al. 2024, in Society of
3087 Photo-Optical Instrumentation Engineers (SPIE)
3088 Conference Series, Vol. 13096, Ground-based and
3089 Airborne Instrumentation for Astronomy X, ed. J. J.
3090 Bryant, K. Motohara, & J. R. D. Vernet, 130961O,
3091 doi: [10.1117/12.3019302](https://doi.org/10.1117/12.3019302)
- 3092 Léget, P. F., Astier, P., Regnault, N., et al. 2021, A&A,
3093 650, A81, doi: [10.1051/0004-6361/202140463](https://doi.org/10.1051/0004-6361/202140463)
- 3094 Lim, K.-T. 2022, Proposal and Prototype for Prompt
3095 Processing, Data Management Technical Note
3096 DMTN-219, Vera C. Rubin Observatory.
3097 <https://dmtn-219.lsst.io/>
- 3098 Lim, K.-T. 2025, The Consolidated Database of Image
3099 Metadata, Data Management Technical Note DMTN-227,
3100 Vera C. Rubin Observatory. <https://dmtn-227.lsst.io/>
- 3101 Louys, M., Tody, D., Dowler, P., et al. 2017, Observation
3102 Data Model Core Components, its Implementation in the
3103 Table Access Protocol Version 1.1., IVOA
3104 Recommendation 09 May 2017
3105 doi: [10.5479/ADS/bib/2017ivoa.spec.0509L](https://doi.org/10.5479/ADS/bib/2017ivoa.spec.0509L)
- 3106 LSST Dark Energy Science Collaboration (LSST DESC),
3107 Abolfathi, B., Alonso, D., et al. 2021, ApJS, 253, 31,
3108 doi: [10.3847/1538-4365/abd62c](https://doi.org/10.3847/1538-4365/abd62c)
- 3109 Lust, N. B., Jenness, T., Bosch, J. F., et al. 2023, arXiv
3110 e-prints, arXiv:2303.03313,
3111 doi: [10.48550/arXiv.2303.03313](https://doi.org/10.48550/arXiv.2303.03313)
- 3112 Mandelbaum, R., Hirata, C. M., Seljak, U., et al. 2005,
3113 MNRAS, 361, 1287,
3114 doi: [10.1111/j.1365-2966.2005.09282.x](https://doi.org/10.1111/j.1365-2966.2005.09282.x)
- 3115 Megias Homar, G., Meyers, J. M., Thomas, S. J., et al.
3116 2024, in Society of Photo-Optical Instrumentation
3117 Engineers (SPIE) Conference Series, Vol. 13094,
3118 Ground-based and Airborne Telescopes X, ed. H. K.
3119 Marshall, J. Spyromilio, & T. Usuda, 130943N,
3120 doi: [10.1117/12.3019361](https://doi.org/10.1117/12.3019361)
- 3121 Melchior, P., Moolekamp, F., Jerdee, M., et al. 2018,
3122 Astronomy and Computing, 24, 129,
3123 doi: [10.1016/j.ascom.2018.07.001](https://doi.org/10.1016/j.ascom.2018.07.001)
- 3124 Mueller, F., et al. 2023, in ASP Conf. Ser., Vol. TBD,
3125 ADASS XXXII, ed. S. Gaudet, S. Gwyn, P. Dowler,
3126 D. Bohlender, & A. Hincks (San Francisco: ASP), in
3127 press. <https://dmtn-243.lsst.io>
- 3128 Naghib, E., Yoachim, P., Vanderbei, R. J., Connolly, A. J.,
3129 & Jones, R. L. 2019, The Astronomical Journal, 157, 151,
3130 doi: [10.3847/1538-3881/aafece](https://doi.org/10.3847/1538-3881/aafece)
- 3131 NSF-DOE Vera C. Rubin Observatory. 2025, Legacy Survey
3132 of Space and Time Data Preview 1, NSF-DOE Vera C.
3133 Rubin Observatory, doi: [10.71929/RUBIN/2570308](https://doi.org/10.71929/RUBIN/2570308)
- 3134 NSF-DOE Vera C. Rubin Observatory. 2025a, Legacy
3135 Survey of Space and Time Data Preview 1: raw dataset
3136 type, NSF-DOE Vera C. Rubin Observatory,
3137 doi: [10.71929/RUBIN/2570310](https://doi.org/10.71929/RUBIN/2570310)
- 3138 NSF-DOE Vera C. Rubin Observatory. 2025b, Legacy
3139 Survey of Space and Time Data Preview 1: visit_image
3140 dataset type, NSF-DOE Vera C. Rubin Observatory,
3141 doi: [10.71929/RUBIN/2570311](https://doi.org/10.71929/RUBIN/2570311)
- 3142 NSF-DOE Vera C. Rubin Observatory. 2025c, Legacy
3143 Survey of Space and Time Data Preview 1: deep_coadd
3144 dataset type, NSF-DOE Vera C. Rubin Observatory,
3145 doi: [10.71929/RUBIN/2570313](https://doi.org/10.71929/RUBIN/2570313)
- 3146 NSF-DOE Vera C. Rubin Observatory. 2025d, Legacy
3147 Survey of Space and Time Data Preview 1:
3148 template_coadd dataset type, NSF-DOE Vera C. Rubin
3149 Observatory, doi: [10.71929/RUBIN/2570314](https://doi.org/10.71929/RUBIN/2570314)
- 3150 NSF-DOE Vera C. Rubin Observatory. 2025e, Legacy
3151 Survey of Space and Time Data Preview 1:
3152 difference_image dataset type, NSF-DOE Vera C. Rubin
3153 Observatory, doi: [10.71929/RUBIN/2570312](https://doi.org/10.71929/RUBIN/2570312)

- 3154 NSF-DOE Vera C. Rubin Observatory. 2025f, Legacy
3155 Survey of Space and Time Data Preview 1: Source
3156 searchable catalog, NSF-DOE Vera C. Rubin
3157 Observatory, doi: [10.71929/RUBIN/2570323](https://doi.org/10.71929/RUBIN/2570323)
- 3158 NSF-DOE Vera C. Rubin Observatory. 2025g, Legacy
3159 Survey of Space and Time Data Preview 1: Object
3160 searchable catalog, NSF-DOE Vera C. Rubin
3161 Observatory, doi: [10.71929/RUBIN/2570325](https://doi.org/10.71929/RUBIN/2570325)
- 3162 NSF-DOE Vera C. Rubin Observatory. 2025h, Legacy
3163 Survey of Space and Time Data Preview 1: ForcedSource
3164 searchable catalog, NSF-DOE Vera C. Rubin
3165 Observatory, doi: [10.71929/RUBIN/2570327](https://doi.org/10.71929/RUBIN/2570327)
- 3166 NSF-DOE Vera C. Rubin Observatory. 2025i, Legacy
3167 Survey of Space and Time Data Preview 1: DiaSource
3168 searchable catalog, NSF-DOE Vera C. Rubin
3169 Observatory, doi: [10.71929/RUBIN/2570317](https://doi.org/10.71929/RUBIN/2570317)
- 3170 NSF-DOE Vera C. Rubin Observatory. 2025j, Legacy
3171 Survey of Space and Time Data Preview 1: DiaObject
3172 searchable catalog, NSF-DOE Vera C. Rubin
3173 Observatory, doi: [10.71929/RUBIN/2570319](https://doi.org/10.71929/RUBIN/2570319)
- 3174 NSF-DOE Vera C. Rubin Observatory. 2025k, Legacy
3175 Survey of Space and Time Data Preview 1:
3176 ForcedSourceOnDiaObject searchable catalog, NSF-DOE
3177 Vera C. Rubin Observatory,
3178 doi: [10.71929/RUBIN/2570321](https://doi.org/10.71929/RUBIN/2570321)
- 3179 NSF-DOE Vera C. Rubin Observatory. 2025l, Legacy
3180 Survey of Space and Time Data Preview 1: CcdVisit
3181 searchable catalog, NSF-DOE Vera C. Rubin
3182 Observatory, doi: [10.71929/RUBIN/2570331](https://doi.org/10.71929/RUBIN/2570331)
- 3183 NSF-DOE Vera C. Rubin Observatory. 2025a, Legacy
3184 Survey of Space and Time Data Preview 1: SSOBJECT
3185 searchable catalog, NSF-DOE Vera C. Rubin
3186 Observatory, doi: [10.71929/RUBIN/2570335](https://doi.org/10.71929/RUBIN/2570335)
- 3187 NSF-DOE Vera C. Rubin Observatory. 2025b, Legacy
3188 Survey of Space and Time Data Preview 1: SSSource
3189 searchable catalog, NSF-DOE Vera C. Rubin
3190 Observatory, doi: [10.71929/RUBIN/2570333](https://doi.org/10.71929/RUBIN/2570333)
- 3191 NSF-DOE Vera C. Rubin Observatory. 2025, Legacy
3192 Survey of Space and Time Data Preview 1: survey
3193 property dataset type, NSF-DOE Vera C. Rubin
3194 Observatory, doi: [10.71929/RUBIN/2570315](https://doi.org/10.71929/RUBIN/2570315)
- 3195 Oke, J. B., & Gunn, J. E. 1983, ApJ, 266, 713,
3196 doi: [10.1086/160817](https://doi.org/10.1086/160817)
- 3197 O'Mullane, W., Economou, F., Huang, F., et al. 2024a, in
3198 Astronomical Society of the Pacific Conference Series,
3199 Vol. 535, Astronomical Data Analysis Software and Systems
3200 XXXI, ed. B. V. Hugo, R. Van Rooyen, & O. M.
3201 Smirnov, 227, doi: [10.48550/arXiv.2111.15030](https://doi.org/10.48550/arXiv.2111.15030)
- 3202 O'Mullane, W., AlSayyad, Y., Chiang, J., et al. 2024b, in
3203 Society of Photo-Optical Instrumentation Engineers
3204 (SPIE) Conference Series, Vol. 13101, Software and
3205 Cyberinfrastructure for Astronomy VIII, ed. J. Ibsen &
3206 G. Chiozzi, 131012B, doi: [10.1117/12.3018005](https://doi.org/10.1117/12.3018005)
- 3207 Onken, C. A., Wolf, C., Bessell, M. S., et al. 2019, PASA,
3208 36, e033, doi: [10.1017/pasa.2019.27](https://doi.org/10.1017/pasa.2019.27)
- 3209 Petrosian, V. 1976, ApJL, 210, L53,
3210 doi: [10.1086/18230110.1086/182253](https://doi.org/10.1086/18230110.1086/182253)
- 3211 Plazas, A. A., Shapiro, C., Smith, R., Huff, E., & Rhodes,
3212 J. 2018, Publications of the Astronomical Society of the
3213 Pacific, 130, 065004, doi: [10.1088/1538-3873/aab820](https://doi.org/10.1088/1538-3873/aab820)
- 3214 Plazas Malagón, A. A., Waters, C., Broughton, A., et al.
3215 2025, Journal of Astronomical Telescopes, Instruments,
3216 and Systems, 11, 011209,
3217 doi: [10.1117/1.JATIS.11.1.011209](https://doi.org/10.1117/1.JATIS.11.1.011209)
- 3218 Plazas Malagón, A., Digel, S., Roodman, A., Broughton,
3219 A., & LSST Camera Team. 2025, LSSTCam and
3220 ComCam Focal Plane Layouts, Vera C. Rubin
3221 Observatory. <https://ctn-001.lsst.io/>
- 3222 Refregier, A. 2003, ARA&A, 41, 645,
3223 doi: [10.1146/annurev.astro.41.111302.102207](https://doi.org/10.1146/annurev.astro.41.111302.102207)
- 3224 Reiss, D. J., & Lupton, R. H. 2016, Implementation of
3225 Image Difference Decorrelation, Data Management
3226 Technical Note DMTN-021, Vera C. Rubin Observatory.
3227 <https://dmtn-021.lsst.io/>
- 3228 Roodman, A., Rasmussen, A., Bradshaw, A., et al. 2024, in
3229 Society of Photo-Optical Instrumentation Engineers
3230 (SPIE) Conference Series, Vol. 13096, Ground-based and
3231 Airborne Instrumentation for Astronomy X, ed. J. J.
3232 Bryant, K. Motohara, & J. R. D. Vernet, 130961S,
3233 doi: [10.1117/12.3019698](https://doi.org/10.1117/12.3019698)
- 3234 Rubin, V. C., & Ford, Jr., W. K. 1970, ApJ, 159, 379,
3235 doi: [10.1086/150317](https://doi.org/10.1086/150317)
- 3236 Rubin, V. C., Ford, Jr., W. K., & Thonnard, N. 1980, ApJ,
3237 238, 471, doi: [10.1086/158003](https://doi.org/10.1086/158003)
- 3238 Rubin Observatory Science Pipelines Developers. 2025, The
3239 LSST Science Pipelines Software: Optical Survey
3240 Pipeline Reduction and Analysis Environment, Project
3241 Science Technical Note PSTN-019, Vera C. Rubin
3242 Observatory, doi: [10.71929/rubin/2570545](https://doi.org/10.71929/rubin/2570545)
- 3243 Rykoff, E. S., Tucker, D. L., Burke, D. L., et al. 2023, arXiv
3244 e-prints, arXiv:2305.01695,
3245 doi: [10.48550/arXiv.2305.01695](https://doi.org/10.48550/arXiv.2305.01695)
- 3246 Saunders, C. 2024, Astrometric Calibration in the LSST
3247 Pipeline, Data Management Technical Note DMTN-266,
3248 Vera C. Rubin Observatory. <https://dmtn-266.lsst.io/>
- 3249 Schutt, T., Jarvis, M., Roodman, A., et al. 2025, The Open
3250 Journal of Astrophysics, 8, 26, doi: [10.33232/001c.132299](https://doi.org/10.33232/001c.132299)

- 3251 Sérsic, J. L. 1963, Boletín de la Asociación Argentina de
3252 Astronomía La Plata Argentina, 6, 41
- 3253 Sérsic, J. L. 1968, Atlas de Galaxias Australes (Córdoba,
3254 Argentina: Observatorio Astronómico)
- 3255 Shanks, T., Metcalfe, N., Chehade, B., et al. 2015,
3256 MNRAS, 451, 4238, doi: [10.1093/mnras/stv1130](https://doi.org/10.1093/mnras/stv1130)
- 3257 SLAC National Accelerator Laboratory, & NSF-DOE Vera
3258 C. Rubin Observatory. 2024, LSST Commissioning
3259 Camera, SLAC National Accelerator Laboratory (SLAC),
3260 Menlo Park, CA (United States),
3261 doi: [10.71929/RUBIN/2561361](https://doi.org/10.71929/RUBIN/2561361)
- 3262 Stalder, B., Reil, K., Claver, C., et al. 2020, in Society of
3263 Photo-Optical Instrumentation Engineers (SPIE)
3264 Conference Series, Vol. 11447, Ground-based and
3265 Airborne Instrumentation for Astronomy VIII, ed. C. J.
3266 Evans, J. J. Bryant, & K. Motohara, 114470L,
3267 doi: [10.1117/12.2561132](https://doi.org/10.1117/12.2561132)
- 3268 Stalder, B., Reil, K., Aguilar, C., et al. 2022, in Society of
3269 Photo-Optical Instrumentation Engineers (SPIE)
3270 Conference Series, Vol. 12184, Ground-based and
3271 Airborne Instrumentation for Astronomy IX, ed. C. J.
3272 Evans, J. J. Bryant, & K. Motohara, 121840J,
3273 doi: [10.1117/12.2630184](https://doi.org/10.1117/12.2630184)
- 3274 Stalder, B., Muñoz, F., Aguilar, C., et al. 2024, in Society
3275 of Photo-Optical Instrumentation Engineers (SPIE)
3276 Conference Series, Vol. 13094, Ground-based and
3277 Airborne Telescopes X, ed. H. K. Marshall, J. Spyromilio,
3278 & T. Usuda, 1309409, doi: [10.1117/12.3019266](https://doi.org/10.1117/12.3019266)
- 3279 Swinbank, J., Axelrod, T., Becker, A., et al. 2020, Data
3280 Management Science Pipelines Design, Data
3281 Management Controlled Document LDM-151, Vera C.
3282 Rubin Observatory. <https://ldm-151.lsst.io/>
- 3283 Taranu, D. S. 2025, The MultiProFit astronomical source
3284 modelling code, Data Management Technical Note
3285 DMTN-312, Vera C. Rubin Observatory.
3286 <https://dmtn-312.lsst.io/>
- 3287 Taylor, M. 2011, TOPCAT: Tool for Operations on
3288 Catalogues And Tables,, Astrophysics Source Code
3289 Library, record ascl:1101.010
- 3290 The Rubin Observatory Survey Cadence Optimization
3291 Committee. 2023, Survey Cadence Optimization
3292 Committee’s Phase 2 Recommendations, Project Science
3293 Technical Note PSTN-055, Vera C. Rubin Observatory.
3294 <https://pstn-055.lsst.io/>
- 3295 The Rubin Observatory Survey Cadence Optimization
3296 Committee. 2025, Survey Cadence Optimization
3297 Committee’s Phase 3 Recommendations, Project Science
3298 Technical Note PSTN-056, Vera C. Rubin Observatory.
3299 <https://pstn-056.lsst.io/>
- 3300 Thomas, S., Connolly, A., Crenshaw, J. F., et al. 2023, in
3301 Adaptive Optics for Extremely Large Telescopes
3302 (AO4ELT7), 67, doi: [10.13009/AO4ELT7-2023-069](https://doi.org/10.13009/AO4ELT7-2023-069)
- 3303 Wang, D. L., Monkewitz, S. M., Lim, K.-T., & Becla, J.
3304 2011, in State of the Practice Reports, SC ’11 (New
3305 York, NY, USA: ACM), 12:1–12:11,
3306 doi: [10.1145/2063348.2063364](https://doi.org/10.1145/2063348.2063364)
- 3307 Waters, C. Z., Magnier, E. A., Price, P. A., et al. 2020,
3308 ApJS, 251, 4, doi: [10.3847/1538-4365/abb82b](https://doi.org/10.3847/1538-4365/abb82b)
- 3309 Whitaker, K. E., Ashas, M., Illingworth, G., et al. 2019,
3310 ApJS, 244, 16, doi: [10.3847/1538-4365/ab3853](https://doi.org/10.3847/1538-4365/ab3853)
- 3311 Wu, X., Roby, W., Goldian, T., et al. 2019, in Astronomical
3312 Society of the Pacific Conference Series, Vol. 521,
3313 Astronomical Data Analysis Software and Systems
3314 XXVI, ed. M. Molinaro, K. Shortridge, & F. Pasian, 32
3315 Xin, B., Claver, C., Liang, M., et al. 2015, ApOpt, 54,
3316 9045, doi: [10.1364/AO.54.009045](https://doi.org/10.1364/AO.54.009045)
- 3317 Yoachim, P. 2022, Survey Strategy: Rolling Cadence,
3318 Project Science Technical Note PSTN-052, Vera C.
3319 Rubin Observatory. <https://pstn-052.lsst.io/>
- 3320 Yoachim, P., Jones, L., Eric H. Neilsen, J., & Becker, M. R.
3321 2024, lsst/rubin_scheduler: v3.0.0, v3.0.0 Zenodo,
3322 doi: [10.5281/zenodo.13985198](https://doi.org/10.5281/zenodo.13985198)
- 3323 Zhang, T., Almoubayyed, H., Mandelbaum, R., et al. 2023,
3324 MNRAS, 520, 2328, doi: [10.1093/mnras/stac3350](https://doi.org/10.1093/mnras/stac3350)